Spectral rehomogenization of cross sections for pin-by-pin nodal diffusion calculations

G.I.A. Lippens

24 April 2017

The work presented in this thesis has been conducted within the context of the Master Thesis project for the Applied Physics M.Sc. program of Delft University of Technology.

This thesis is to be defended on 01-05-2017 at 15:00.

Student ID:	4031644	
Thesis committee:	Dr. ir. D. Lathouwers	TU Delft (TNW, supervisor)
	Prof. dr. ir. J.L. Kloosterman	TU Delft (TNW)
	Dr. ir. M.B. van Gijzen	TU Delft (EWI)

Abstract

Equivalent cross sections used in few-group nodal diffusion calculations are obtained through homogenization of fissile unit cells under infinite medium conditions. Reference reaction rates can be accurately reproduced in nodal calculations provided that these unit cells are surrounded by cells of the same type. Large heterogeneities, however, invalidate this approach and lead to cross section errors up to 15 %. The spectral rehomogenization method, developed at AREVA NP, has provided adequate error reductions in calculations employing assembly-level homogenization by imposing cross section corrections based on spectrum variation reconstruction using nodal calculation output. In the present thesis the spectral rehomogenization method is validated and its feasibility assessed in two-group pin-by-pin nodal diffusion calculations. It is found that significant cross section error reductions can be achieved, as well as reductions in errors related to the pin power distribution. However, improvements to the method are necessary in highly heterogeneous media to ensure adequate error reductions in group cross sections associated with fast and epithermal neutrons. Additionally, large errors may be introduced as a consequence of inconsistencies in the present implementation.

Keywords: homogenization, spectral rehomogenization, cross sections, nodal diffusion, pin-by-pin

Acknowledgements

Several calculations in this thesis were performed using the TU Delft in-house code BRISINGR, written by Matteo Gamarino.
In the completion of this thesis the efforts of several key people should not slide by unnoticed.
I wish to express my gratitude firstly and foremostly to Matteo Gamarino for being available at all times to provide the necessary advice, for our near-daily discussions and for his assistance in taking my first steps into the field of neutronics. I wish you the best of luck in the completion of your PhD project.
I want to thank Danny Lathouwers for maintaining overview of the project and for sharing his indispensible knowledge of computational reactor physics.
Moreover I wish to thank Danny Lathouwers, Jan-Leen Kloosterman and Martin van Gijzen for taking place in the assessment committee reviewing this thesis.
Also thanks to:

- Frank Wols and August Winkelman for providing support in the use of the HPC system and SCALE.
- the people at NERA for making my stay in the group enjoyable,
- my friends and family for always being supportive throughout the duration of my studies,
- Yosta, for everything you are and everything you do.

Finally I want to thank the Ministry of Education, Culture and Science of the Netherlands, for pursuing access to a high standard of education for all of their citizens.

Nomenclature

Roman characters

a_f	Fission emission spectrum coefficient
$c_{j,g}$	Leakage weighting coefficient
D	Diffusion coefficient
E	Energy
f	Discontinuity factor
g	Energy group
h	Homogenization coefficient
H	Heaviside function
$\vec{j}$	Angular neutron current density
$\vec{J}$	Neutron current density
k	Node index
k_{eff}	Multiplication factor
L	Leakage rate
n	Neutron density
N	Nuclide density
Q	Rehomogenization basis function
$\vec{r}$	Spatial coordinate
r_g	Logarithmic energy group width
t	Time
T	Chebyshev polynomial
u	Pseudo-lethargy
v	Velocity
ΔV	Control volume
W	Weighting function

Greek characters

α	Nodal expansion coefficient
β	Rehomogenization expansion coefficient
μ	Scattering angle cosine
ν	Number of neutrons produced per fission
ρ	Nodal expansion leakage coefficient
σ	Microscopic cross section
Σ	Macroscopic cross section
$\tilde{\varphi}$	Angular neutron flux density
φ	Neutron flux density (unit normalization)
ϕ	Neutron flux density
$\hat{\phi}$	Neutron flux density (homogeneous)
$\bar{\phi}$	Neutron flux density (node-averaged)
χ	Fission neutron emission spectrum
ψ	Nodal expansion basis function
$\hat{\Omega}$	Solid angle

Table of Contents

Chapter 1

Introduction

Reactor core simulations play a vital role in the analysis of nuclear reactor behaviour. Such analysis includes the investigation and design of new reactor types and fuel loading patterns, safety assessments for performing experiments in research reactors and operation of power reactors, and routine analysis and optimization studies in existing reactors. Recent decades saw a rapid increase in computational capabilities at ever reducing cost. As a consequence, also the detailed computational study of nuclear reactor behaviour has become increasingly feasible.

Core simulations can be stochastic or deterministic, and both categories have their merits and drawbacks. Stochastic simulations, or Monte Carlo simulations, perform a pre-defined number of single particle simulations with randomized input variables. Monte Carlo simulations provide the possibility to solve complex problems without physical approximations or geometrical simplifications, but getting results with good precision requires a large number of samples [1]. Deterministic simulations are capable of producing approximate results, already at low cost, but the errors resulting from the approximations, on which the simulation relies, cannot be corrected simply through increasing the computational burden by spatial, angular or spectral refinement.

In deterministic methods reaction rate distributions are determined by finding the neutron flux density distribution in space, angle and energy. The category can be subdivided in transport and diffusion methods. Like their names suggest, methods in the former group find the neutron flux by solving the neutron transport balance equation, whereas diffusion methods solve an approximation to the transport equation called the neutron diffusion equation. The neutron transport and diffusion equations relate the rate of change of the neutron flux density in a control volume to the net neutron leakage rate and nuclear reaction rates in that volume.

Nuclear reaction rates scale with the neutron flux via *macroscopic cross sections*, specific to each reaction type and dependent on incident neutron energy, isotopic composition and density of the medium under consideration.

The macroscopic cross section is closely related to the *microscopic cross section*, which can be seen from a classical physics viewpoint as a target area for a particle to collide with in order to undergo a specific nuclear reaction. While in reality the probabilistic behaviour of neutron-nuclear interactions is more complicated, this operational definition is statistically adequate when a large number of neutrons and nuclei is considered [2].

Cross sections are elaborately dependent on the energy of the incident neutron, being subject to various energy dependence regimes in different regions, including resolved and unresolved resonant behaviour. A computational approach that attempts to capture all details of the energy dependence of cross sections for all materials present in the core requires a very fine energy meshing, employing several hundreds of energy meshes.

In addition, a nuclear reactor core is typically composed of several hundreds of fuel assemblies, each consisting again of several hundreds of fuel pins, absorber rods, detector arrays and water channels. Consequently the spatial cross section distribution, following the material distribution, is highly heterogeneous.

The detailed simulation of systems subject to these heterogeneities quickly becomes highly expensive, thus the development of computational schemes capable of accurately reproducing reaction rates at reduced computational costs is an active area of research.

Common reactor physics methods employ the spatial homogenization of cross sections to assembly-

or pin-level nodes and the collapsing to a few energy group structure (2 to 4 groups for water-moderated reactors [3]) via flux weighting to maintain reaction rates. The weighting fluxes used for these procedures commonly come from detailed transport calculations on a single pin cell or assembly at infinite medium conditions. This approach becomes invalidated when dealing with large spatial and spectral heterogeneity between cells, for example in the case of UO_2 fuel pins neighbouring MOX fuel pins or absorber rods. Homogenization methods to overcome this issue have long been the subject of extensive study.

Recent efforts by AREVA NP have attempted to reproduce these environmental effects by imposing spatial and spectral corrections to few-group cross sections that are obtained via flux-variation reconstruction using nodal data ([4], [5]). These *rehomogenization* methods have been demonstrated to be promising in the reduction of cross section and power errors in nodal diffusion calculations with assembly-sized meshes [6].

In these assembly-level calculations, mesh sizes are generally several times larger than the neutron mean free path, with environmental effects manifesting themselves mainly through variations on the spatial flux distribution and to a lesser extent on the neutron flux spectrum [3]. At the pin-by-pin level spectral effects are expected to dominate as the thermal neutron mean free path and the mesh size are of comparable length. The aforementioned rehomogenization methods should be studied at the pin-by-pin level separately, in order to account for the differences in behaviour of neutron diffusion processes between these length scales.

The objective of the present thesis is to validate and investigate the feasibility the spectral rehomogenization method in the framework of nodal diffusion calculations with pin-size meshes. The structure of the thesis is as follows: The framework of homogenization theory in neutron diffusion calculations is discussed in Chapter 2. Chapter 3 covers nodal methods, the rehomogenization method and the computational schemes applied in this research. In Chapter 4 the results of rehomogenization and reference calculations applied to pin checkerboard and assembly colorset configurations are discussed, of which the most important findings are summarized in Chapter 5.

Chapter 2

Neutron diffusion and homogenization theory

2.1 Neutron transport and cross sections

In deterministic methods reaction rates and reactor behaviour over time are calculated by finding the *neutron flux density*, a (scalar) quantity defined as:

$$\tilde{\varphi}(\vec{r}, E, \hat{\Omega}, t) = v(E)n(\vec{r}, E, \hat{\Omega}, t), \tag{2.1}$$

where n is the density of neutrons at location $\vec{r}$, flowing in the direction $\hat{\Omega}$ with a kinetic energy E, at time t, and v is the speed of the neutrons [2]. A quantity closely related to the neutron flux density is the *neutron current density* vector, which is defined as:

$$\vec{j}(\vec{r}, E, \hat{\Omega}, t) = \tilde{\varphi}(\vec{r}, E, \hat{\Omega}, t)\hat{\Omega} \tag{2.2}$$

The behaviour of the flux in an arbitrary volume ΔV is governed by the Boltzmann neutron transport equation.In this equation the rate of change for the neutron flux density is determined by the balance between the following losses:

- the net rate at which neutrons leak away from the volume ΔV through its outer surface ∂V;
- the total reaction rate engaged in by neutrons with an energy E and with direction $\hat{\Omega}$;

and the following gains:

- the rate at which neutrons scatter to $E, \hat{\Omega}$ from the whole energy spectrum ($0 < E < \infty$) and from all angles ($\hat{\Omega} \in 4\pi$);
- the rate at which neutrons are released from nuclear fissions at an energy E and with direction $\hat{\Omega}$, and
- an external source term s.

These terms are mathematically formulated in equation (2.3), which is the volume-integrated neutron transport equation [2].

$$\begin{aligned}
\int_{\Delta V} \frac{1}{v(E)} \frac{\partial}{\partial t} \tilde{\varphi}(\vec{r}, E, \hat{\Omega}, t) \mathrm{d}^3\vec{r} + \oint_{\partial V} \vec{j}(\vec{r}, E, \hat{\Omega}, t) \cdot \mathrm{d}^2\vec{S} \\
+ \int_{\Delta V} \Sigma_t(\vec{r}, E, \hat{\Omega}, t) \tilde{\varphi}(\vec{r}, E, \hat{\Omega}, t) \mathrm{d}^3\vec{r} \\
= \int_{\Delta V} \int_{[0,\infty],4\pi} \Sigma_s(\vec{r}, E' \to E, \hat{\Omega}' \to \hat{\Omega}, t) \tilde{\varphi}(\vec{r}, E', \hat{\Omega}', t) \mathrm{d}E' \mathrm{d}\hat{\Omega}' \mathrm{d}^3\vec{r} \\
+ \int_{\Delta V} \chi(\vec{r}, E, \hat{\Omega}, t) \int_{[0,\infty],4\pi} \nu\Sigma_f(\vec{r}, E', \hat{\Omega}', t) \tilde{\varphi}(\vec{r}, E', \hat{\Omega}', t) \mathrm{d}E' \mathrm{d}\hat{\Omega}' \mathrm{d}^3\vec{r} \\
+ \int_{\Delta V} s(\vec{r}, E, \hat{\Omega}, t) \mathrm{d}^3\vec{r}
\end{aligned} \tag{2.3}$$

The symbol Σ_q reprents the macroscopic cross section for a reaction type q, a material parameter characterizing the probability that the neutron-nuclear interaction q occurs, with units (cm^{-1}). It depends on the isotopic composition of the medium and the microscopic cross sections of the constituent nuclides in the following way:

$$\Sigma_q = \sum_i N_i \sigma_{q,i}, \tag{2.4}$$

where $\sigma_{q,i}$ is the microscopic cross section, with units of *barn* ($1\,\mathrm{b} = 10^{-24}\,\mathrm{cm}^2$), for the reaction type q of nuclide i, of which N_i is the nuclide density with units (cm^{-3}) or $((\mathrm{bcm})^{-1})$.

An example of the elaborate energy dependence of nuclear cross sections is illustrated in Figure 2.1.

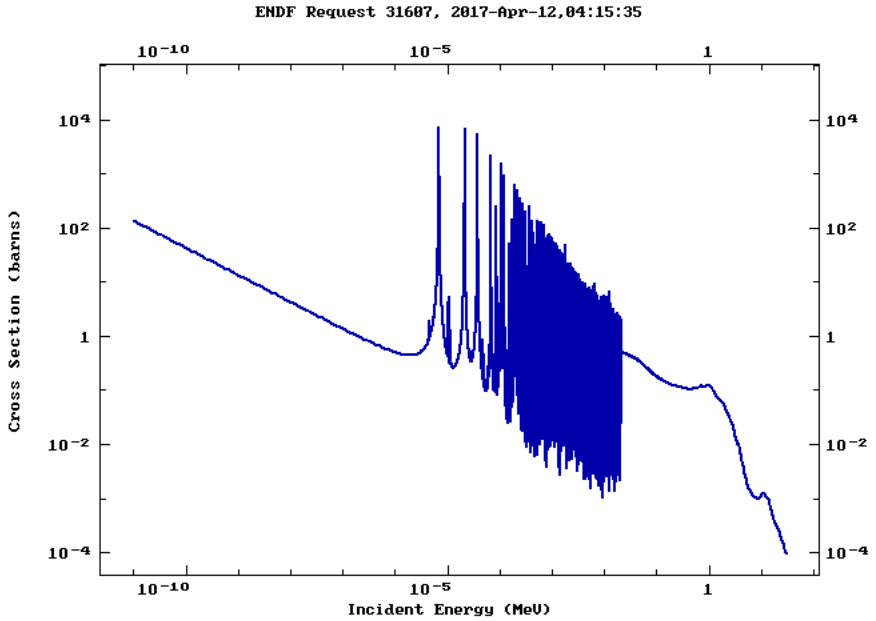

Figure 2.1: Cross section energy dependence for gamma-emissive neutron capture in ^{238}U [7].

For the purpose of this thesis we limit ourselves to the time-independent criticality formulation of the Boltzmann equation. The criticality formulation describes the self-multiplicative behaviour of a nuclear reactor system in which the neutron population sustains itself, without external sources. This formulation reads:

$$\begin{aligned} \oint_{\partial V} \vec{j}(\vec{r}, E, \hat{\Omega}) \cdot \mathrm{d}^2\vec{S} + \int_{\Delta V} \Sigma_t(\vec{r}, E, \hat{\Omega}) \tilde{\varphi}(\vec{r}, E, \hat{\Omega}) \mathrm{d}^3\vec{r} \\ = \int_{\Delta V} \int_{[0,\infty],4\pi} \Sigma_s(\vec{r}, E' \to E, \hat{\Omega}' \to \hat{\Omega}) \tilde{\varphi}(\vec{r}, E', \hat{\Omega}') \mathrm{d}E' \mathrm{d}\hat{\Omega}' \mathrm{d}^3\vec{r} \\ + \frac{1}{k_{\mathrm{eff}}} \int_{\Delta V} \chi(\vec{r}, E, \hat{\Omega}) \int_{[0,\infty],4\pi} \nu\Sigma_f(\vec{r}, E', \hat{\Omega}') \tilde{\varphi}(\vec{r}, E', \hat{\Omega}') \mathrm{d}E' \mathrm{d}\hat{\Omega}' \mathrm{d}^3\vec{r} \end{aligned} \tag{2.5}$$

The solution to the criticality problem determines the flux $\tilde{\varphi}$, with arbitrary normalization that yields an additional degree of freedom, and the eigenvalue k_{eff}. Taking into account that scattering is not an actual source of neutrons, but rather draws neutrons from other energies, and thus gives a zero net contribution to the overall neutron population, it can be seen from equation (2.5) that:

$$k_{\mathrm{eff}} = \frac{\text{production rate}}{\text{loss rate}} \tag{2.6}$$

This implies that k_{eff} determines the time-dependent behaviour of a reactor in one of the following ways:

$k_{\text{eff}} > 1$	super-critical reactor	$\tilde{\varphi}$ increases
$k_{\text{eff}} = 1$	critical reactor	$\tilde{\varphi}$ is sustained
$k_{\text{eff}} < 1$	sub-critical reactor	$\tilde{\varphi}$ decreases

The first term in equation (2.5), the leakage term, can be rewritten to a volume integral using the divergence theorem:

$$\oint_{\partial V} \vec{j}(\vec{r}, E, \hat{\Omega}) \cdot \mathrm{d}^2\vec{S} = \int_{\Delta V} \nabla \cdot \vec{j}(\vec{r}, E, \hat{\Omega}) \mathrm{d}^3\vec{r} \tag{2.7}$$

With every term now being an integral over the arbitrary volume ΔV, the equation can be simplified by removing the integral.

$$\begin{aligned} \nabla \cdot \vec{j}(\vec{r}, E, \hat{\Omega}) &+ \Sigma_t(\vec{r}, E, \hat{\Omega})\tilde{\varphi}(\vec{r}, E, \hat{\Omega}) \\ &= \int_{[0,\infty],4\pi} \Sigma_s(\vec{r}, E' \to E, \hat{\Omega}' \to \hat{\Omega})\tilde{\varphi}(\vec{r}, E', \hat{\Omega}')\mathrm{d}E'\mathrm{d}\hat{\Omega}' \\ &+ \frac{1}{k_{\text{eff}}}\chi(\vec{r}, E, \hat{\Omega}) \int_{[0,\infty],4\pi} \nu\Sigma_f(\vec{r}, E', \hat{\Omega}')\tilde{\varphi}(\vec{r}, E', \hat{\Omega}'\mathrm{d}E'\mathrm{d}\hat{\Omega}') \end{aligned} \tag{2.8}$$

Taking into account the identity

$$\nabla \cdot (c\vec{x}) = c\nabla \cdot \vec{x} + \vec{x} \cdot \nabla c,$$

and noting that the solid angle $\hat{\Omega}$ does not depend on $\vec{r}$, substituting the definition of the current, equation (2.2), into equation (2.8) yields:

$$\begin{aligned} \hat{\Omega} \cdot \nabla\tilde{\varphi}(\vec{r}, E, \hat{\Omega}) &+ \Sigma_t(\vec{r}, E, \hat{\Omega})\tilde{\varphi}(\vec{r}, E, \hat{\Omega}) \\ &= \int_{[0,\infty],4\pi} \Sigma_s(\vec{r}, E' \to E, \hat{\Omega}' \to \hat{\Omega})\tilde{\varphi}(\vec{r}, E', \hat{\Omega}')\mathrm{d}E'\mathrm{d}\hat{\Omega}' \\ &+ \frac{1}{k_{\text{eff}}}\chi(\vec{r}, E, \hat{\Omega}) \int_{[0,\infty],4\pi} \nu\Sigma_f(\vec{r}, E', \hat{\Omega}')\tilde{\varphi}(\vec{r}, E', \hat{\Omega}')\mathrm{d}E'\mathrm{d}\hat{\Omega}' \end{aligned} \tag{2.9}$$

It is clearly visible that the neutron transport equation is a first order differential equation. There are six degrees of freedom: three in space, one in energy and two in solid angle. Formulating an analytical solution to neutron transport problems is next to impossible, with possible exception of heavily simplified systems. Several deterministic strategies exist to solve the neutron transport equation numerically, such as the method of discrete ordinates and the collision probability method [3]. Such strategies, however, are usually computationally intensive.

2.2 Neutron diffusion theory

Often in reactor physics a detailed treatment of the angular dependence of the neutron flux is not necessary [2], and eliminating the angular dependence substantially reduces the computational burden. This can be done by employing the *neutron continuity equation*, which is the angle-independent form of the neutron transport equation. The neutron continuity equation requires an additional relation between the neutron flux and the neutron current, which is provided by the *diffusion approximation*. The neutron continuity equation and neutron diffusion theory are discussed in the present section.

The neutron continuity equation is derived by introducing the angle-integrated scalar flux ϕ:

$$\phi(\vec{r}, E) = \int_{4\pi} \tilde{\varphi}(\vec{r}, E, \hat{\Omega})\mathrm{d}\hat{\Omega}, \tag{2.10}$$

as well as the angle-integrated neutron current $\vec{J}$:

$$\vec{J}(\vec{r}, E) = \int_{4\pi} \vec{j}(\vec{r}, E, \hat{\Omega})\mathrm{d}\hat{\Omega}, \tag{2.11}$$

and asserting that the cross sections Σ_t and Σ_f are angle-independent and that the angular dependence of the scattering cross section Σ_s is only influenced by the cosine of the scattering angle $\mu_0 = \hat{\Omega}' \cdot \hat{\Omega}$. The latter of these assertions implies that [2]:

$$\int_{4\pi} \Sigma_s(E' \to E, \hat{\Omega}' \to \hat{\Omega}) \mathrm{d}\hat{\Omega} = 2\pi \int_{-1}^{+1} \Sigma_s(E' \to E, \mu_0) \mathrm{d}\mu_0 = \Sigma_s(E' \to E) \tag{2.12}$$

Incorporating above assertions into equation (2.8) yields the neutron continuity equation [1]:

$$\begin{aligned} &\nabla \cdot \vec{J}(\vec{r}, E) + \Sigma_t(\vec{r}, E)\phi(\vec{r}, E) \\ &\quad = \int_0^\infty \Sigma_s(\vec{r}, E' \to E)\phi(\vec{r}, E)\mathrm{d}E' + \frac{1}{k_{\text{eff}}}\chi(\vec{r}, E) \int_0^\infty \nu\Sigma_f(\vec{r}, E')\phi(\vec{r}, E')\mathrm{d}E' \end{aligned} \tag{2.13}$$

Characteristic to diffusion theory is the diffuson approximation, which asserts that the neutron current J is proportional to the gradient of the flux ϕ by the following relation:

$$\vec{J}(\vec{r}, E) = -\frac{1}{3(\Sigma_t(\vec{r}, E) - \bar{\mu}(\vec{r}, E)\Sigma_s(\vec{r}, E))} \nabla\phi(\vec{r}, E), \tag{2.14}$$

where the parameter $\bar{\mu}$ is the cosine of the average scattering angle [1].
The expression $\Sigma_t(\vec{r}, E) - \bar{\mu}(\vec{r}, E)\Sigma_s(\vec{r}, E)$ in the denominator is usually abbreviated to Σ_{tr} and is called the *transport cross section*. The proportionality constant between the neutron current density and the neutron flux density, $(3\Sigma_{tr})^{-1}$, is again abbreviated to D, which is called the *diffusion coefficient*. The proportionality relation in abbreviated form reads:

$$\vec{J}(\vec{r}, E) = -D(\vec{r}, E)\nabla\phi(\vec{r}, E) \tag{2.15}$$

Equation (2.15) is commonly referred to as *Fick's Law*. Substituting Fick's Law into the leakage term in equation (2.13) yields:

$$\begin{aligned} &-\nabla \cdot D(\vec{r}, E)\nabla\phi(\vec{r}, E) + \Sigma_t(\vec{r}, E)\phi(\vec{r}, E) \\ &\quad = \int_0^\infty \Sigma_s(\vec{r}, E' \to E)\phi(\vec{r}, E)\mathrm{d}E' + \frac{1}{k_{\text{eff}}}\chi(\vec{r}, E) \int_0^\infty \nu\Sigma_f(\vec{r}, E')\phi(\vec{r}, E')\mathrm{d}E', \end{aligned} \tag{2.16}$$

which is the continuous energy neutron diffusion equation. Since the diffusion equation is of second order in space, the set of possible solutions is more limited than that of the first order neutron transport equation.

Diffusion theory relies on the following approximations

- The angular neutron flux is only weakly dependent on angular variables, such that a linearization in angular variables is justified;
- The fission source term is isotropic in the LAB inertial frame;
- The anisotropic contribution to energy transfer through scattering is negligible, and
- The inverse neutron speed multiplied by the neutron current rate of change is small compared to the neutron flux gradient.

With coarse energy discretization, diffusion theory produces accurate results for near-homogeneous regions that are large compared to the neutron mean free path, with small flux gradients. Strongly absorbing or anisotropic scattering media will cause problems, as well as material interfaces with large density differences, such as vacuum boundaries [1].

2.3 Spatial and spectral discretization

The present study investigates cross section rehomogenization in the framework of multi-group nodal diffusion calculations. Multi-group methods rely on condensing continuous-energy neutron fluxes, currents and material and geometrical parameters to a small number of energy groups. As a convention, the energy group indices run from maximum to minimum energy, so that E_0 corresponds to the

maximum energy and E_G to the minimum energy, where G is the number of groups. This reflects the life cycle of the neutrons, that is, the fact that fission neutrons originate in the high-energy region and through several scattering events lose their kinetic energy until they are eventually absorbed in a resonance or in the low (thermal) energy region where they may cause a new fission event [2]. An energy group structure is illustrated in Figure 2.2. The group g comprises all energies between E_g and E_{g-1}.

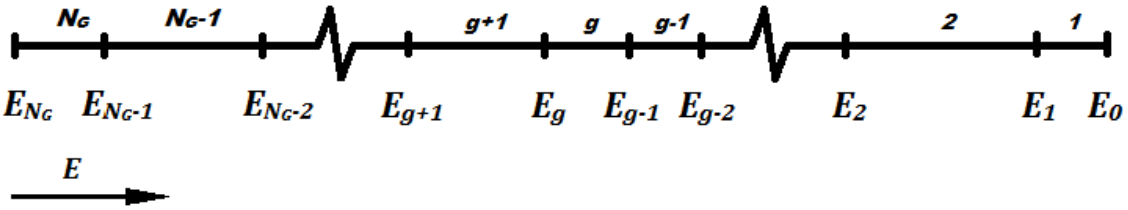

Figure 2.2: An arbitrary energy group structure, where the lowest indices correspond to the highest energies.

Spatial discretization in nodal methods may be performed to hexagonal or Cartesian geometry [8]. In the present thesis the geometry is discretized to Cartesian coordinates, as specifically pin-by-pin configurations reminiscent of pressurized water reactor core layouts are studied. The Cartesian spatial discretization is illustrated in two dimensions in Figure 2.3. Node k is the region defined by

$$x_k - \frac{\Delta x_k}{2} \leq x \leq x_k + \frac{\Delta x_k}{2}, \qquad y_k - \frac{\Delta y_k}{2} \leq y \leq y_k + \frac{\Delta y_k}{2}, \qquad z_k - \frac{\Delta z_k}{2} \leq z \leq z_k + \frac{\Delta z_k}{2},$$

and will be assumed to have spatially homogeneous cross sections and a uniform diffusion coefficient, as is convention in nodal methods.

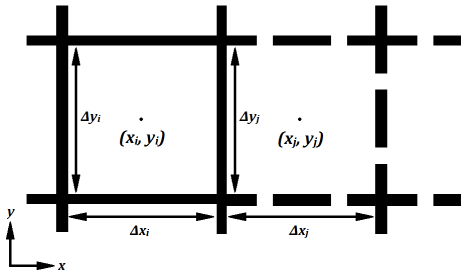

Figure 2.3: A 2D representation of the spatial discretization in Cartesian coordinates.

2.4 Cross section homogenization

2.4.1 General Equivalence Homogenization

In order to further develop an approximate solution to the diffusion problem, it is necessary that an equivalent problem be formulated based on the discretizations described in the previous section. This is done by writing an equation analogous to the diffusion equation, for energy group g:

$$\nabla \cdot \hat{\vec{J}}_g(\vec{r}) + \hat{\Sigma}_{t,g}(\vec{r})\hat{\phi}_g(\vec{r}) = \sum_{g'=1}^{G} \hat{\Sigma}_{s,g'\to g}(\vec{r})\hat{\phi}_{g'}(\vec{r}) + \frac{1}{k_{\text{eff}}} \sum_{g'=1}^{G} \chi_g \nu \hat{\Sigma}_{f,g'}(\vec{r})\hat{\phi}_{g'}(\vec{r}) \tag{2.17}$$

Where the group flux $\hat{\phi}_g$ for the homogeneous problem is defined as:

$$\hat{\phi}_g(\vec{r}) = \int_{E_g}^{E_{g-1}} \hat{\phi}(\vec{r}, E)\mathrm{d}E \tag{2.18}$$

and the current satisfies Fick's law:

$$\hat{\vec{J}}_g(\vec{r}) = -\hat{D}_g(\vec{r})\nabla\hat{\phi}_g(\vec{r}) \tag{2.19}$$

The hats above the quantities denote that the quantities relate to the homogeneous (equivalent) problem.
Equivalence between the homogeneous and the heterogeneous solutions is achieved if reaction rates and surface currents are accurately preserved. For the total reaction rate in group g in the homogeneous node k this translates to:

$$\hat{\Sigma}^k_{t,g}\int_{\Delta V_k}\hat{\phi}_g(\vec{r})\mathrm{d}^3\vec{r} = \int_{\Delta V_k}\int_{E_g}^{E_{g-1}}\Sigma_t(\vec{r},E)\phi(\vec{r},E)\mathrm{d}E\mathrm{d}^3\vec{r} \tag{2.20}$$

For the scattering and fission reaction rates, the procedure is analogous:

$$\hat{\Sigma}^k_{s,g'\to g}\int_{\Delta V_k}\hat{\phi}_{g'}(\vec{r})\mathrm{d}^3\vec{r} = \int_{\Delta V_k}\int_{E'_g}^{E_{g'-1}}\int_{E_g}^{E_{g-1}}\Sigma_s(\vec{r},E'\to E)\phi(\vec{r},E')\mathrm{d}E\mathrm{d}E'\mathrm{d}^3\vec{r} \tag{2.21}$$

$$\chi_g\nu\hat{\Sigma}^k_{f,g'}\int_{\Delta V_k}\hat{\phi}_{g'}(\vec{r})\mathrm{d}^3\vec{r} = \int_{\Delta V_k}\int_{E'_g}^{E_{g'-1}}\int_{E_g}^{E_{g-1}}\chi(r,E)\nu\Sigma_f(\vec{r},E')\phi(\vec{r},E')\mathrm{d}E\mathrm{d}E'\mathrm{d}^3\vec{r} \tag{2.22}$$

Using equations (2.20), (2.21) and (2.22), one can in principle determine the total, scattering and fission cross sections that preserve reaction rates, provided that the heterogeneous and homogeneous solutions are known. Preservation of the surface currents requires that, for every surface l of node k:

$$\hat{D}^k_g\int_{S^l_k}\nabla\hat{\phi}_g(\vec{r})\cdot\mathrm{d}^2\vec{S} = -\int_{E_g}^{E_{g-1}}\int_{S^l_k}\vec{J}(\vec{r},E)\cdot\mathrm{d}^2\vec{S}\mathrm{d}E \tag{2.23}$$

In addition to the heterogeneous and homogeneous fluxes not being known beforehand, another complication is that the above condition must be satisfied for all surfaces l of node k simultaneously. Imposing continuity of the neutron fluxes and currents along node interfaces, there is an insufficient number of degrees of freedom remaining to permit this.

The surface current paradox was first resolved in 1978 by Koebke's Equivalence Theory [9], which formed the basis for Smith's 1980 *General Equivalence Theory* (GET) ([10], [11]).
The common approach for homogenizing cross sections relies on the assertion that the neutron flux distributions (both homogeneous and heterogeneous) in the unit cell under infinite medium conditions - that is, in an infinite lattice of identical unit cells - only weakly deviate from their respective distributions in the cell under actual environmental conditions.

$$\phi(\vec{r},E) \approx \phi^\infty(\vec{r},E) \tag{2.24a}$$

$$\hat{\phi}(\vec{r},E) \approx \hat{\phi}^\infty(\vec{r},E) \tag{2.24b}$$

The fluxes ϕ^∞ and $\hat{\phi}^\infty$ can be found by solving the neutron transport equation for the unit cell, for example a fuel pin or a quarter assembly, with reflective boundary conditions on all sides to simulate the infinite medium environment. By using infinite medium flux-weighting, often good approximations can be made for the nuclear reaction rates.

In addition to the infinite medium approximation, the node-average flux distribution is asserted to be preserved between the heterogeneous and homogeneous problems, so that the flux integral on the LHS of equations (2.20),(2.21) and (2.22) is approximated by:

$$\int_{\Delta V_k}\hat{\phi}_g(\vec{r})\mathrm{d}^3\vec{r} \approx \int_{\Delta V_k}\phi_g(\vec{r})\mathrm{d}^3\vec{r} \approx \int_{\Delta V_k}\int_{E_g}^{E_{g-1}}\phi^\infty(\vec{r},E)\mathrm{d}E\mathrm{d}^3\vec{r} \tag{2.25}$$

This leads to the general approximation of the cross sections as:

$$\Sigma^k_{q,k} \approx \frac{\int_{\Delta V_k}\int_{E_g}^{E_{g-1}}\Sigma_q(\vec{r},E)\phi^\infty(\vec{r},E)\mathrm{d}E\mathrm{d}^3\vec{r}}{\int_{\Delta V_k}\int_{E_g}^{E_{g-1}}\phi^\infty(\vec{r},E)\mathrm{d}E\mathrm{d}^3\vec{r}} \tag{2.26}$$

The preservation of the surface currents is achieved by introducing new degrees of freedom, using which the flux continuity condition at the interface $k, x+$ is replaced by the condition:

$$f^k_{g,x+}\hat{\phi}^k_{g,x+} = f^{k+1}_{g,x-}\hat{\phi}^{k+1}_{g,x-} \tag{2.27}$$

where the *discontinuity factor* $f^k_{g,x\pm}$ is defined as the surface-averaged heterogeneous flux divided by the homogeneous flux:

$$f^k_{g,x\pm} = \frac{\phi^k_{g,x\pm}}{\hat{\phi}^k_{g,x\pm}} \tag{2.28}$$

The subscripts $x\pm$ denote surface averaging at the interfaces delimiting the node in the x dimension, that is:

$$\hat{\phi}^k_{g,x\pm} = \frac{1}{\Delta y_k \Delta z_k}\int_{z_k-\Delta z_k/2}^{z_k+\Delta z_k/2}\int_{y_k-\Delta y_k/2}^{y_k+\Delta y_k/2}\hat{\phi}_g(x_k \pm \frac{\Delta x_k}{2}, y, z)\mathrm{d}y\mathrm{d}z \tag{2.29a}$$

$$\phi^k_{g,x\pm} = \frac{1}{\Delta y_k \Delta z_k}\int_{z_k-\Delta z_k/2}^{z_k+\Delta z_k/2}\int_{y_k-\Delta y_k/2}^{y_k+\Delta y_k/2}\phi_g(x_k \pm \frac{\Delta x_k}{2}, y, z)\mathrm{d}y\mathrm{d}z \tag{2.29b}$$

These discontinuity factors, like the nuclear cross sections, can be approximated using the result of the infinite medium calculation. A clear illustration of the flux discontinuity condition in one dimension is provided in Smith's 1986 paper [11], and is here displayed in Figure 2.4.

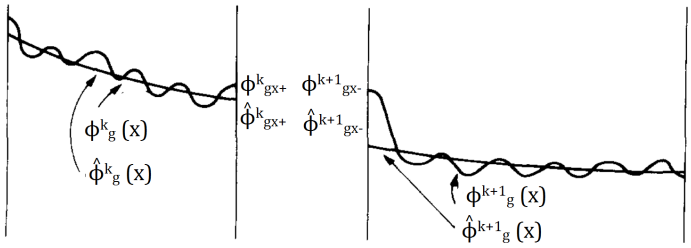

Figure 2.4: A one dimensional representation of the flux continuity condition. Φ and $\hat{\Phi}$ denote the heterogeneous and homogeneous medium fluxes respectively [11].

Several weighting strategies exist for determining the homogenized diffusion coefficient [3]. In the present thesis it is derived from the flux-volume weighted transport cross section Σ_{tr} that is obtained via the outscatter approximation [12], following the procedure of equation (2.26).

Other homogenization strategies have been developed for pin-by-pin geometries, such as the SPH method ([13], [14]) and more recently the ISH method [15]. The present thesis focuses on GET homogenization, as discussed above.

Cross section homogenization is commonly performed in extensive branch calculations that simulate cells under various combinations of state parameters [16]. Input parameters for core calculations may be interpolated on the cross section libraries resulting from these branch calculations [5]. This forms the first (off-line) step of the common two-step approach in nodal core calculations.

2.4.2 Pin-by-pin and assembly homogenization

Historically the focus of homogenization methods has been in the framework of assembly-size meshing. It has been only in recent decades, when computational capabilities have increased, that calculations based on pin-by-pin meshing have become feasible. Since in pin-by-pin meshing the mesh size is smaller than the typical thermal neutron mean free path $(\Sigma_{t,th})^{-1}$, the streaming term becomes more dominant. Inter-nodal leakages are typically stronger than in assembly level meshing-based calculations.

The pin-by-pin meshing limits the validity of the diffusion approximation, due to the reliance of the latter on large near-homogeneous regions. To this end, researchers have expressed interest in low-order transport approximations, such as SP_3, in which some angular dependence is preserved ([17], [18]).

Pin-by-pin meshing allows for reactor core calculations to high spatial detail without additional pin-power reconstruction schemes, as used in calculations with assembly-level meshing [11]. Additionally, the application of a nodal expansion method to pin-by-pin calculations is optional but not necessary. A nodal expansion method for SP_3 transport calculations with pin-level meshing has been applied succesfully in [17].

On the other hand pin-by-pin calculations are computationally more demanding than assembly level calculations, as a vastly larger number of nodes is required to model identical systems. Furthermore, pin-by-pin calculations deal with larger heterogeneity between nodes, leading to stronger spectral effects from the environment, than in the case of assembly-sized nodes. Such spectral effects are typically smoothed out over several mean free path-lengths in calculations with assembly-level meshing.

It is shown in [19] that homogenization effects in neutron transport calculations are small in cores fueled heterogeneously with UO_2 and MOX assemblies, but larger power variations occur in and near Gd-loaded rods. In [13] it is demonstrated that GET outperforms the SPH homogenization approach in terms of power error reduction, albeit at a higher computational cost.

A fuel assembly homogenized to 2×2 nodes per pin is shown in Figure 2.5.

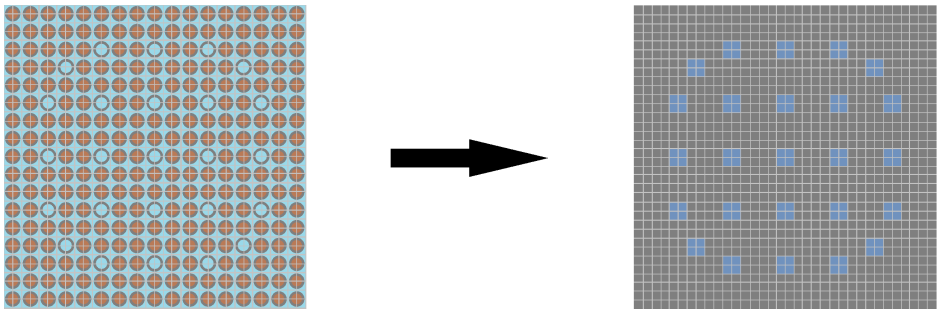

Figure 2.5: Spatial discretization to a pin-by-pin level mesh of a UO_2 fuel assembly in two dimensions, with 2×2 nodes per pin

2.5 Rehomogenization

In the homogenization process, the flux approximation by the infinite medium flux is acceptable, provided that the unit cell exists in an environment of largely similar cells, but loses its validity when the unit cell is in a heterogeneous environment, when the zero net current boundary conditions are invalidated by strong flux gradients. Examples of such heterogeneities are UO_2 fuel rods next to a guide tube, a burnable absorber rod, or near an interface with an assembly containing MOX fuel. It should be noted that these heterogeneities in the environment affect the local flux distribution both spatially and spectrally. For instance, a fuel rod neighbouring a strong thermal neutron absorber, such as a gadolinium rod, will experience a hardened neutron spectrum and a lowered thermal group flux near the heterogeneous interface, with respect to the infinite medium case.

Methods have been developed earlier to adress the limited validity of infinite-medium homogenization in a heterogeneous environment [20]. In any such method it is necessary to incorporate environmental data into the definition of the homogenized cross sections.

The present thesis focuses on the spectral rehomogenization method developed at AREVA NP, in which spectral corrections are applied on-line to the homogenized material properties, based on nodal calculation output and homogenization parameters prepared off-line.

The method was first presented in a paper by Dall'Osso, Tomatis and Du in 2010 [5], based on the Migration Mode Method (MMM), which posed an alternative to the multi-group approach [21]. A spatial rehomogenization method had been presented earlier [4]. The spectral and spatial rehomogenization methods were formalized into a consistent theoretical framework, along with a burnup-dependent correction, by Gamarino et al. in 2016 [6].

2.5.1 Homogenization defect

The homogenization defect modelled in [6] discerns between the infinite medium and environmental cross sections as shown in equations (2.30) and (2.31). As PWR core calculations generally adopt only one depletion history, aside from considering flux differences, it is also necessary to discern between the continuous cross section distributions Σ_q^{∞} and Σ_q^{env}.

$$\hat{\Sigma}_{q,g}^{k,\infty} = \frac{\int_{\Delta V_k}\int_{E_g}^{E_{g-1}} \Sigma_q^{\infty}(\vec{r},E)\phi^{\infty}(\vec{r},E)\mathrm{d}E\mathrm{d}\vec{r}}{\int_{\Delta V_k}\int_{E_g}^{E_{g-1}} \phi^{\infty}(\vec{r},E)\mathrm{d}E\mathrm{d}\vec{r}} \tag{2.30}$$

$$\hat{\Sigma}_{q,g}^{k,env} = \frac{\int_{\Delta V_k}\int_{E_g}^{E_{g-1}} \Sigma_q^{env}(\vec{r},E)\phi^{env}(\vec{r},E)\mathrm{d}E\mathrm{d}\vec{r}}{\int_{\Delta V_k}\int_{E_g}^{E_{g-1}} \phi^{env}(\vec{r},E)\mathrm{d}E\mathrm{d}\vec{r}} \tag{2.31}$$

The average flux values in the numerators and denominators cancel out in equations (2.30) and (2.31). Cross sections collapsed using differently normalized weighting fluxes are therefore equivalent to the cross sections in these equations. We define the node-average flux $\bar{\phi}_g^k$ for group g in node k as follows:

$$\Delta V_k \bar{\phi}_g^k \equiv \int_{\Delta V_k}\int_{E_g}^{E_{g-1}} \phi^{env}(\vec{r},E)\mathrm{d}E\mathrm{d}\vec{r} \tag{2.32}$$

Furthermore we introduce the flux variation as the difference between the environmental flux spatial and energy distribution and the infinite-medium distribution, whilst maintaining the node-average flux, as follows:

$$\delta\phi(\vec{r},E) = \bar{\phi}_g^k \delta\varphi(\vec{r},E) = \bar{\phi}_g^k(\varphi^{env}(\vec{r},E) - \varphi^{\infty}(\vec{r},E)) \tag{2.33}$$

Where φ are the environmental and infinite-medium flux distributions normalized such that $\int_{\Delta V_k}\int_{E_g}^{E_{g-1}} \varphi\mathrm{d}\vec{r}\mathrm{d}E = 1$. We further define the cross section variation $\delta\Sigma_q$ as follows:

$$\delta\Sigma_q(\vec{r},E) = \Sigma_q^{env}(\vec{r},E) - \Sigma_q^{\infty}(\vec{r},E) \tag{2.34}$$

The following expression can then be achieved for the environmental homogeneous cross section:

$$\begin{aligned}\hat{\Sigma}_{q,g}^{k,env} = \frac{1}{\Delta V_k \bar{\phi}_g^k}\int_{\Delta V_k}\int_{E_g}^{E_{g-1}} &[\Sigma_q^{\infty}(\vec{r},E)\bar{\phi}_g^k\varphi^{\infty}(\vec{r},E) \\ &+ \Sigma_q^{\infty}(\vec{r},E)\delta\phi(\vec{r},E) + \delta\Sigma_q(\vec{r},E)\phi^{env}(\vec{r},E)]\mathrm{d}E\mathrm{d}^3\vec{r}\end{aligned} \tag{2.35}$$

which can be condensed to:

$$\hat{\Sigma}_{q,g}^{k,env} = \hat{\Sigma}_{q,g}^{k,\infty} + \delta\hat{\Sigma}_{q,g}^{k,(r)} + \delta\hat{\Sigma}_{q,g}^{k,(xs)} \tag{2.36}$$

The terms in equation (2.36) correspond to the flux-volume-averaged, group-integrated terms of the integrand in equation (2.35). They represent, in order of appearance:

- The cross section homogenized in infinite-medium conditions,
- The homogenization defect corresponding to the spatial and spectral flux variations between the environmental and infinite-medium conditions, and
- The homogenization defect corresponding to the cross section variation as a result of intra-nodal burnup differences.

The present thesis considers zero burnup configurations only. Consequently the burnup-related homogenization defect is disregarded.

In [6] it is demonstrated that the flux variation homogenization defect:

$$\delta\hat{\Sigma}_{q,g}^{k,(r)} = \frac{1}{\Delta V_k \bar{\phi}_g^k}\int_{\Delta V_k}\int_{E_g}^{E_{g-1}} \Sigma_q^{\infty}(\vec{r},E)\delta\phi(\vec{r},E)\mathrm{d}E\mathrm{d}^3\vec{r}, \tag{2.37}$$

can be approximated by the sum of a spatial, a spectral and a cross term:

$$\delta\hat{\Sigma}_{q,g}^{k,(r)} \approx \delta\hat{\Sigma}_{q,g}^{k,spat} + \delta\hat{\Sigma}_{q,g}^{k,spec} + \delta\hat{\Sigma}_{q,g}^{k,cross}, \tag{2.38}$$

where the spatial and spectral cross section corrections correspond to those defined in [4] and [5] respectively. For the spectral correction, that is:

$$\delta\hat{\Sigma}_{q,g}^{k,spec} = \frac{1}{\bar{\phi}_g^k}\int_{E_g}^{E_{g-1}} \Sigma_q^{k,\infty}(E)\delta\phi^k(E)\mathrm{d}E \tag{2.39}$$

Where $\Sigma_q^{k,\infty}(E)$ is the spatially homogenized infinite medium cross section and $\delta\phi^k(E)$ is the *spectrum variation*. The spectral rehomogenization method consists of the reconstruction of this spectrum variation using only information from the nodal calculation and from cross section libraries that have been prepared prior to the nodal calculation.

To this end a lethargy-like variable u is introduced, defined as:

$$u = \frac{\log\frac{E}{E_{m,G}}}{\log\frac{E_{p,G}}{E_{m,G}}}, \tag{2.40}$$

where G refers to the group index for the macro-group structure applied in this thesis. $E_{p,G}$ and $E_{m,G}$ refer to the maximum and minimum energy boundary of macro-group G respectively. At the lower and upper bounds of each macro-group, the pseudo-lethargy u attains a value of 0 or 1, respectively. The quantity $\frac{E_{p,G}}{E_{m,G}} = r_G$ is the logarithmic width of the G-th macro-group.

The macro-group structure in the present thesis is defined by:

$$\begin{aligned} E_{p1} &= 20.0\,\mathrm{MeV}, \quad & E_{m1} &= 0.625\,\mathrm{eV} \\ E_{p2} &= 0.625\,\mathrm{eV}, \quad & E_{m2} &= 1.00\cdot 10^{-5}\,\mathrm{eV} \end{aligned}$$

The definition of the spectral cross section correction translates to:

$$\delta\Sigma_{q,G}^{k,spec} = \frac{1}{\bar{\phi}_G^k}\int_0^1 \Sigma_{q,G}^{k,\infty}(u)\delta\phi_G^k(u)\mathrm{d}u \tag{2.41}$$

Where $\delta\phi_G^k(u)$ is now the spectrum variation per unit lethargy. The notation includes both G for the macro-group and u corresponding to (in principle) a continuous energy variable or a micro-group as is the case in the present thesis.

2.5.2 Spectrum variation reconstruction

In order to maintain the node-average flux values from the core calculation, the average value of $\delta\phi_G^k$ must be zero for all k and all G.

$$\int_0^1 \delta\phi_G^k(u)\mathrm{d}u = 0 \tag{2.42}$$

The reconstruction of the spectrum variation in the rehomogenization method starts by expansion of the spectrum variation in the G-th group in $N_{Q,G}$ basis functions [5]:

$$\delta\phi_G^k(u) = \sum_{i=1}^{N_{Q,G}} \beta_{i,G}^k Q_{i,G}(u) \tag{2.43}$$

By defining an integral:

$$h_{V,q,i,0,G} = \int_0^1 \Sigma_{q,G}^{k,\infty}(u)Q_{i,G}(u)\mathrm{d}u, \tag{2.44}$$

the following expression for the spectral cross section correction can be obtained:

$$\delta\Sigma_{q,G}^{k,spec} = \frac{1}{\bar{\phi}_G^k}\sum_{i=1}^{N_{Q,G}} \beta_{i,G}^k h_{V,q,i,0,G} \tag{2.45}$$

The subscript V in $h_{V,q,i,j,G}$ denotes that the term is the result of the cross section homogenization on a component of the spectrum variation. The spectral cross section correction becomes a superposition of these integrals, of which the calculation requires only infinite medium data and knowledge of pre-defined trial and weighting functions. Details of the numerical implementation of this model will be further discussed in the following chapter.

Chapter 3

Computational approach

In this chapter the computational methodology of the present thesis will be discussed. A coarse-mesh finite difference scheme, extended by the nodal expansion method (CMFD+NEM), is applied. This will be discussed in the first section of this chapter. The second section covers the spectrum variation reconstruction and cross section rehomogenization procedure. An in-house code, developed at TU Delft, is used to solve the diffusion problem with rehomogenized cross sections. This will be discussed in the third section, as well as the detailed heterogeneous transport calculations with reference to which the errors of the calculations performed in this work are determined.

3.1 Nodal diffusion method

Nodal extensions to finite difference methods have long been standard in neutronics calculations in which the spatial discretization takes place at the assembly level, due to their potential to substantially reduce the errors in reaction rates at low computational cost [8]. The application of nodal methods at the pin-by-pin level is a more recent development, having been enabled by the vast increase in computational power in recent decades [17].

We use the spatially continuous multi-group diffusion equation as the starting point for the fine mesh finite difference approach:

$$\nabla \cdot J_g(\vec{r}) + \Sigma_{t,g}(\vec{r})\phi_g(\vec{r}) = Q_g(\vec{r}), \tag{3.1}$$

where we have, for the sake of readability, condensed the source term to $Q_g(\vec{r})$:

$$Q_g(\vec{r}) = \sum_{g'=1}^{G} \Sigma_{s,g'\to g}(\vec{r})\phi_{g'}(\vec{r}) + \frac{\chi_g(\vec{r})}{k_{\text{eff}}} \sum_{g'=1}^{G} \nu\Sigma_{f,g'}(\vec{r})\phi_{g'}(\vec{r}), \tag{3.2}$$

Equation (3.1) is averaged over the node volume ΔV_k to obtain (via the divergence theorem):

$$\frac{1}{\Delta V_k} \oint_{\partial V_k} J_g(\vec{r}) \cdot \mathrm{d}^2\vec{S} + \Sigma^k_{t,g}\bar{\phi^k_g} = \bar{Q^k_g}, \tag{3.3}$$

where $\bar{\phi^k_g}$ is the node-average flux, defined as:

$$\bar{\phi^k_g} = \frac{1}{\Delta V_k} \int_{\Delta V_k} \phi_g(\vec{r})\mathrm{d}^3\vec{r}, \tag{3.4}$$

The leakage term of equation (3.3) is written out as:

$$\begin{aligned} \frac{1}{\Delta V_k} \oint_{\partial V_k} J_g(\vec{r}) \cdot \mathrm{d}^2\vec{S} &= \frac{1}{\Delta x_k \Delta y_k \Delta z_k}[(\bar{J}^k_{g,x+} - \bar{J}^k_{g,x-})\Delta y_k \Delta z_k \\ &\quad + (\bar{J}^k_{g,y+} - \bar{J}^k_{g,y-})\Delta x_k \Delta z_k + (\bar{J}^k_{g,z+} - \bar{J}^k_{g,z-})\Delta x_k \Delta y_k] \\ &= \frac{\bar{J}^k_{g,x+} - \bar{J}^k_{g,x-}}{\Delta x_k} + \frac{\bar{J}^k_{g,y+} - \bar{J}^k_{g,y-}}{\Delta y_k} + \frac{\bar{J}^k_{g,z+} - \bar{J}^k_{g,z-}}{\Delta z_k} \end{aligned} \tag{3.5}$$

In which the surface integrated interface currents are defined as:

$$J^k_{g,x\pm} = \int_{z_k-\Delta z_k/2}^{z_k+\Delta z_k/2} \int_{y_k-\Delta y_k/2}^{y_k+\Delta y_k/2} \vec{J}_g(x_k \pm \frac{\Delta x_k}{2}, y, z) \cdot \pm\hat{x}\, \mathrm{d}y\, \mathrm{d}z \tag{3.6}$$

in the x-direction. In the y and z directions similar definitions apply.
The rewritten leakage term of equation (3.5) is substituted into equation (3.3) to obtain:

$$\frac{\bar{J}^k_{g,x+} - \bar{J}^k_{g,x-}}{\Delta x_k} + \frac{\bar{J}^k_{g,y+} - \bar{J}^k_{g,y-}}{\Delta y_k} + \frac{\bar{J}^k_{g,z+} - \bar{J}^k_{g,z-}}{\Delta z_k} + \Sigma^k_{t,g}\bar{\phi}^k_g = \bar{Q}^k_g, \tag{3.7}$$

where now Fick's law is applied to express the surface currents in terms of the node average fluxes. Fick's law yields the following approximation for the current in the x direction:

$$\bar{J}^k_{g,x+} \approx -D^{k,FDM}_{NC,g,x+} \frac{\bar{\phi}^{k+1}_g - \bar{\phi}^k_g}{\frac{\Delta x_{k+1}}{2} + \frac{\Delta x_k}{2}} \tag{3.8a}$$

$$\bar{J}^k_{g,x-} \approx -D^{k,FDM}_{NC,g,x-} \frac{\bar{\phi}^k_g - \bar{\phi}^{k-1}_g}{\frac{\Delta x_k}{2} + \frac{\Delta x_{k-1}}{2}} \tag{3.8b}$$

The quantity $D^k_{NC,g,x\pm}$ is the coupled diffusion coefficient [22], which is the harmonic average of the diffusion coefficients:

$$D^{k,FDM}_{NC,g,x\pm} = \frac{\Delta x_k + \Delta x_{k\pm1}}{\frac{\Delta x_k}{D^k_g} + \frac{\Delta x_{k\pm1}}{D^{k\pm1}_g}} \tag{3.9}$$

In equations (3.8) and (3.9) specifically, the node indexing $k \pm 1$ is associated with the translation along the x direction. The currents and coupling coefficients in the y and z directions are found analogously.

The result of the spatial discretization and node coupling is a linear system of $N \times G$ equations, where N is the number of nodes and G is the number of energy groups, to which $(k_{\text{eff}}, \vec{\phi})$ is the solution. A typical numerical solution approach iterates the leakage, total removal and scattering source terms while keeping the fission source term constant. After convergence or after a fixed number of iterations the fission source and k_{eff} are updated in an outer iteration. This cycle is repeated until k_{eff} has converged.

This finite difference scheme, however, limits the detail to which the spatial flux distribution can be determined. This is especially troublesome in calculations employing coarse meshing, for example at the assembly level. Additionally no consideration is given to the interface flux discontinuity condition discussed in section 2.4. As a result the scheme is not able to accurately predict surface currents and reaction rates. To this end a nodal method is introduced, in which the flux profiles are expanded in a number of basis functions.

The nodal method which will be applied in the present thesis is the Nodal Expansion Method (NEM), in which the flux profiles are expanded in a set of polynomial functions [8]. Like most other nodal methods, the NEM is based on one-dimensional equations derived by integrating the three-dimensional diffusion equation over the two dimensions transverse to the dimension considered [8]. In the x-direction, the transverse integrated diffusion equation reads:

$$\frac{d}{dx}J_{g,x}(x) + \Sigma^k_{t,g}\phi_{g,x}(x) + \frac{1}{\Delta y_k}L^k_{g,y}(x) + \frac{1}{\Delta z_k}L^k_{g,y}(x) = Q^k_{g,x}(x), \tag{3.10}$$

where the one-dimensional current scales to the continuous gradient of the one-dimensional flux:

$$\bar{J}^k_{g,x}(x) = -D^k_g \frac{d}{dx}\bar{\phi}^k_{g,x}(x) \tag{3.11}$$

The transverse integrated flux is defined as:

$$\phi^k_{g,x}(x) = \frac{1}{\Delta y_k \Delta z_k} \int_{z_k-\Delta z_k/2}^{z_k+\Delta z_k/2} \int_{y_k-\Delta y_k/2}^{y_k+\Delta y_k/2} \phi_g(x,y,z)\mathrm{d}y\mathrm{d}z \tag{3.12}$$

and the transverse leakage rates are:

$$L^k_{g,y}(x) = \frac{1}{\Delta z_k} \int_{z_k-\Delta z_k/2}^{z_k+\Delta z_k/2} [J^k_{g,y+}(x,z) - J^k_{g,y-}(x,z)]\mathrm{d}z \tag{3.13a}$$

$$L^k_{g,z}(x) = \frac{1}{\Delta y_k} \int_{y_k-\Delta y_k/2}^{y_k+\Delta y_k/2} [J^k_{g,z+}(x,y) - J^k_{g,z-}(x,y)]\mathrm{d}y \tag{3.13b}$$

The one-dimensional fluxes, currents and leakages depend on the three-dimensional flux and current distributions, of which the exact profiles are unknown. In the Nodal Expansion Method, the one-dimensional fluxes are instead approximated by an expansion in a set of N_F polynomial basis functions:

$$\phi^k_{g,x}(x) \approx \bar{\phi}^k_g \psi^k_0(x) + \sum_{n=1}^{N_F} \alpha^k_{g,x,n} \psi^k_n(x), \tag{3.14}$$

where $\bar{\phi}^k_g$ is the node-average flux. In this thesis N_F will be restricted to 4. The basis functions for this expansion read:

$$\psi^k_0(x) = 1 \tag{3.15a}$$

$$\psi^k_1(x) = \frac{x}{\Delta x_k} \tag{3.15b}$$

$$\psi^k_2(x) = 3(\frac{x}{\Delta x_k})^2 - \frac{1}{4} \tag{3.15c}$$

$$\psi^k_3(x) = (\frac{x}{\Delta x_k})(\frac{x}{\Delta x_k} - \frac{1}{2})(\frac{x}{\Delta x_k} + \frac{1}{2}) \tag{3.15d}$$

$$\psi^k_4(x) = ((\frac{x}{\Delta x_k})^2 - \frac{1}{20})(\frac{x}{\Delta x_k} - \frac{1}{2})(\frac{x}{\Delta x_k} + \frac{1}{2}) \tag{3.15e}$$

The transverse leakage $L^k_{g,y}(x)$ is expanded up to second order:

$$L^k_{g,y}(x) = \bar{L}^k_{g,y} + \rho^k_{g,y,1}\psi^k_1(x) + \rho^k_{g,y,2}\psi^k_2(x), \tag{3.16}$$

In which the node-average y-direction leakage rate suffices the following relation with the surface average currents:

$$\bar{L}^k_{g,y} = \frac{1}{\Delta x_k} \int_{x_k-\Delta x_k/2}^{x_k+\Delta x_k/2} L^k_{g,y}(x)\mathrm{d}x = \bar{J}^k_{g,y+} - \bar{J}^k_{g,y-} \tag{3.17}$$

and the coefficients ρ are such that, assuming that $L^k_{g,y}(x)$ extends over the nodes $k-1, k, k+1$, integrating equation (3.16) over the nodes $k-1$ and $k+1$ yields the average leakages $\bar{L}^{k-1}_{g,y}$ and $\bar{L}^{k+1}_{g,y}$ respectively [8].
The leakage relation, equation (3.17), shows that the expansion coefficients along the different directions must be related across dimensions. Consequently the nodal expansion along three dimensions leads, including the node-average flux $\bar{\phi}^k_g$, to a problem with $3N_F + 1$ unknowns, and thus $3N_F + 1$ equations must be found to close the problem for each group on each node.

The first 6 equations, 2 per direction, come from the flux discontinuity and current continuity requirements. In the x direction, that is:

$$f^k_{g,x-}\phi^k_{g,x}(x_k - \frac{\Delta x_k}{2}) = f^{k-1}_{g,x+}\phi^{k-1}_{g,x}(x_{k-1} + \frac{\Delta x_{k-1}}{2}) \tag{3.18}$$

$$J^k_{g,x}(x_k - \frac{\Delta x_k}{2}) = J^{k-1}_{g,x}(x_{k-1} + \frac{\Delta x_{k-1}}{2}) \tag{3.19}$$

The continuity relations along the y and z directions follow analogous equations. Another $3(N_F - 2)$ equations are provided by applying a weighted residual method to the transverse integrated diffusion equation. In the present case that means two per direction. For $n = 1, 2$:

$$\langle \psi_n^k(x), \frac{d}{dx} J_{g,x}^k(x) \rangle + \Sigma_{t,g}^k \phi_{g,x,n}^k + \frac{1}{\Delta y_k} L_{g,y,x,n}^k + \frac{1}{\Delta z_k} L_{g,z,x,n}^k = Q_{g,x,n}^k \tag{3.20}$$

where the weighted residual moments of the flux, leakage rates and sources are defined as:

$$\phi_{g,x,n}^k = \langle \psi_n^k(x), \phi_g^k(x) \rangle \tag{3.21a}$$
$$L_{g,y,x,n}^k = \langle \psi_n^k(x), L_{g,y}^k(x) \rangle \tag{3.21b}$$
$$L_{g,z,x,n}^k = \langle \psi_n^k(x), L_{g,z}^k(x) \rangle \tag{3.21c}$$
$$Q_{g,x,n}^k = \langle \psi_n^k(x), Q_{g,x}^k(x) \rangle \tag{3.21d}$$

The inner product of ψ_n^k and any function ζ, in turn, is defined here as:

$$\langle \psi_n^k(x), \zeta(x) \rangle = \int_{x_k - \Delta x_k/2}^{x_k + \Delta x_k/2} \psi_n^k(x) \zeta(x) \mathrm{d}x \tag{3.22}$$

Again, the y and z corrolaries follow from applying analogous procedures.
The final equation relating the node-average flux and the expansion coefficients is the node-averaged diffusion equation, equation (3.7). The closed problem is a linear one of, in this case, 13 unknowns. Such a problem can easily be solved directly.

The solution to the nodal problem is applied to the finite difference method in the form of a correction to the coupled diffusion coefficient $D_{NC,g,x\pm}^{k,NEM}$, which is defined such that it satisfies the relation:

$$\bar{J}_{g,x+}^{k,NEM} = -D_{NC,g,x+}^{k,FDM} \frac{\bar{\phi}_g^{k+1} - \bar{\phi}_g^k}{\frac{\Delta x_{k+1}}{2} + \frac{\Delta x_k}{2}} + D_{NC,g,x+}^{k,NEM} \frac{\bar{\phi}_g^{k+1} + \bar{\phi}_g^k}{\frac{\Delta x_{k+1}}{2} + \frac{\Delta x_k}{2}} \tag{3.23a}$$
$$\bar{J}_{g,x-}^{k,NEM} = -D_{NC,g,x-}^{k,FDM} \frac{\bar{\phi}_g^{k} - \bar{\phi}_g^{k-1}}{\frac{\Delta x_{k}}{2} + \frac{\Delta x_{k-1}}{2}} + D_{NC,g,x-}^{k,NEM} \frac{\bar{\phi}_g^{k} + \bar{\phi}_g^{k-1}}{\frac{\Delta x_{k}}{2} + \frac{\Delta x_{k-1}}{2}} \tag{3.23b}$$

Where $\bar{J}_{g,x\pm}^{k,NEM}$ is the neutron current following from the nodal solution. Subsequent finite difference iterations employ the corrected coupled diffusion coefficient from the most recent nodal update by equating the finite difference current $\bar{J}_{g,x\pm}^{k,FDM}$ to the right hand side of equation (3.23). Before any nodal correction is applied, the coupled diffusion coefficient correction is zero, thereby rendering equation (3.23) equal to the finite difference relation expressed in equation (3.8) [22]. A *nodal update*, an update of the correction to the coupling coefficient, may be performed after an outer iteration.

3.2 Rehomogenization method

3.2.1 Spectrum variation coefficients

As shown in equation (2.43) in the previous chapter, the rehomogenization involves the expansion of the spectrum variation in a finite number of basis functions. This expansion, like the nodal expansion, requires additional equations in order to solve for all unknowns. Similarly, a weighted residual technique is used, applied over the neutron lethargy balance equation, which reads [16]:

$$L_G^k(u) + \Sigma_{t,G}^k(u) \phi_G^{env,k}(u) = \sum_{g'=1}^{N_G} \int_0^1 [\Sigma_{s,G' \to G}^k(u' \to u) \phi_{G'}^{env,k}(u') + \frac{\chi_G(u)}{k_{\text{eff}}} \nu \Sigma_{f,G'}^k \phi_{G'}^{env,k}(u')] \mathrm{d}u' \tag{3.24}$$

Here $L_G^k(u)$ is the leakage rate for pseudo-lethargy u.

The spectrum variation expansion is substituted into equation (3.24) and the equation is weighted by a set of $N_{Q,G}$ weighting functions $W_{j,G}(u)$. For readability the superscript k indicating the node is dropped. The weighted equations are of the form:

$$\begin{aligned} c_{j,G}\bar{L}_G + h_{R,t,j,G}\bar{\phi}_G + \sum_{i=1}^{N_{Q,G}} h_{V,t,i,j,G}\beta_{i,G} &= \sum_{G'=1}^{N_G}(h_{R,s,j,G'\to G}\bar{\phi}_{G'} + \sum_{i=1}^{N_{Q,G}} h_{R,s,j,G'\to G}\beta_{i,G'}) \\ + \frac{\chi_{j,G}}{k_{\text{eff}}}\sum_{G'=1}^{N_G}(h_{R,f,G'}\bar{\phi}_{G'} + \sum_{i=1}^{N_{Q,G}} h_{V,f,i,G'}\beta_{i,G'}) &\qquad j \in \{1,\ldots,N_{Q,G}\} \end{aligned} \tag{3.25}$$

Where the following definitions apply for the rehomogenization parameters corresponding to the neutron leakage and fission emission spectrum:

$$c_{j,G} = \frac{1}{\bar{L}_G}\int_0^1 W_{j,G}(u)L_G(u)\mathrm{d}u, \tag{3.26a}$$

$$\chi_{j,G} = \int_0^1 W_{j,G}(u)\chi_G(u)\mathrm{d}u, \tag{3.26b}$$

The reference infinite medium homogenization coefficients h_R are:

$$h_{R,t,j,G} = \frac{1}{\bar{\phi}_G}\int_0^1 W_{j,G}(u)\Sigma_{t,G}(u)\phi_G^\infty(u)\mathrm{d}u, \tag{3.27a}$$

$$h_{R,s,j,G'\to G} = \frac{1}{\bar{\phi}_{G'}}\int_0^1 W_{j,G}(u)\int_0^1 \Sigma_{s,G'\to G}(u'\to u)\phi_{G'}^\infty(u')\mathrm{d}u'\mathrm{d}u, \tag{3.27b}$$

$$h_{R,f,G} = \frac{1}{\bar{\phi}_G}\int_0^1 \nu\Sigma_{f,G}(u)\phi_G^\infty(u)\mathrm{d}u, \tag{3.27c}$$

and the variational homogenization coefficients h_V are:

$$h_{V,t,i,j,G} = \int_0^1 W_{j,G}(u)\Sigma_{t,G}(u)Q_{i,G}(u)\mathrm{d}u, \tag{3.28a}$$

$$h_{V,s,i,j,G'\to G} = \int_0^1 W_{j,G}(u)\int_0^1 \Sigma_{s,G'\to G}(u'\to u)Q_{i,G'}(u')\mathrm{d}u'\mathrm{d}u, \tag{3.28b}$$

$$h_{V,f,i,G} = \int_0^1 \nu\Sigma_{f,G}(u)Q_{i,G}(u)\mathrm{d}u. \tag{3.28c}$$

The homogenization parameters defined in equations , and are calculated off-line at the cross section library level. Only the (locally linear) rehomogenization problem, equation (3.25), is solved on-line. Due to the local nature of this problem, this procedure may be parallelized [16].

In an earlier implementation by Dall'Osso et al. continuity of the flux spectrum and its first derivative was imposed at the energy boundary [5], but has been disregarded due to instability. All relations between rehomogenization coefficients are residual equations.

The closed linear system of $\sum_{G=1}^{N_G} N_{Q,G}$ residual equations and unknowns is set up and solved independently for each node, to obtain the expansion coefficients $\beta_{i,G}$. Subsequently, the spectrum variation is calculated using equation (2.43) and the spectral correction to the cross sections by equation (2.45). The coefficient $h_{V,q,i,0,G}$ in (2.44) is the result of weighting the cross section expansion integrals with the function $W_{0,G} = 1$.

3.2.2 Basis functions and weighting functions

The accuracy of the spectrum reconstruction depends on the set of basis functions chosen for the rehomogenization. This thesis adopts a standard number of basis functions of 4 per group.

The diffusion and rehomogenization problems are solved in a two-group framework, i.e. $N_G = 2$, where the energy boundary is located at $E_{p2} = E_{m1} = 0.625\,\text{eV}$. For the numerical implementation the full energy domain is truncated at the low and high ends at $10^{-5}\,\text{eV}$ and $20\,\text{MeV}$ respectively. Fast and epithermal neutrons, predominantly subject to down-scattering, self-scattering and resonance absorption, are located in group $G = 1$, whereas neutrons in group $G = 2$ are subject mostly to self-scattering and thermal absorption, but to an almost negligible extent to upscattering. The neutrons in the latter group are predominant in inducing fission events.

Results from earlier studies have shown local extreme values in the spectrum variation at high energies ([5], [6], [16]). Consequently the migration mode modelled after the fission emission spectrum is used, since the emission spectrum is weakly affected by the environment.

$$\chi(E) = \sqrt(E) \exp -a_f E \tag{3.29}$$

where $a_f = 0.776$ [23]. The average of the fission emission spectrum is:

$$\chi^{avg} = \int_0^\infty \chi(E)\mathrm{d}E = \frac{\sqrt{\pi}}{2a_f^{3/2}} \tag{3.30}$$

In order to satisfy equation (2.42) regardless of the closed problem posed in the previous subsection, it is required that the average value over the whole group is zero for all basis functions. Therefore the average value of the fission emission spectrum is subtracted to obtain the definite basis function in the pseudo-lethargy domain:

$$Q_{1,1}(u) = (E_{1-})^{3/2} e^{a_f E_{1-} r_1^u} \log r_1 (r_1^u)^{3/2} - \chi^{avg} \tag{3.31}$$

Where $r_1 = \frac{E_{p1}}{E_{m1}}$ is the logarithmic width of the fast group.

The other basis functions in the fast group are modelled after Chebyshev polynomials, which obey the following regime:

$$T_0(u) = 1 \tag{3.32a}$$
$$T_1(u) = u \tag{3.32b}$$
$$T_i(u) = 2uT_{i-1}(u) - T_{i-2}(u) \qquad i \geq 2 \tag{3.32c}$$

While the standard number of basis functions is 4, an expansion with functions modelled after Chebyshev polynomials can in principle be continued indefinitely. The basis functions based on the Chebyshev polynomials must have zero average values as well, leading to the following expressions:

$$Q_{2,1}(u) = u - \frac{1}{2} \tag{3.33a}$$
$$Q_{3,1}(u) = 2u^2 - \frac{2}{3} \tag{3.33b}$$
$$Q_{4,1}(u) = 4u^3 - 3u + \frac{1}{2} \tag{3.33c}$$

The basis functions in the thermal region are zero averaged Chebyshev polynomials as well, albeit on a subinterval $u \in [b, 1]$, with $b > 0$.

$$Q_{1,2}(u) = H(u-b)(\frac{u-b}{1-b} - \frac{1}{2}) \tag{3.34a}$$
$$Q_{2,2}(u) = H(u-b)(2(\frac{u-b}{1-b})^2 - \frac{2}{3}) \tag{3.34b}$$
$$Q_{3,2}(u) = H(u-b)(4(\frac{u-b}{1-b})^3 - 3\frac{u-b}{1-b} + \frac{1}{2}) \tag{3.34c}$$
$$Q_{4,2}(u) = H(u-b)(8(\frac{u-b}{1-b})^4 - 8(\frac{u-b}{1-b})^2 + \frac{16}{15}) \tag{3.34d}$$

$H(u-b)$ is the Heaviside function which attains unit value for $u > b$ and zero elsewhere. The subinterval approach is chosen in compliance with earlier studies that showed a negligible spectrum variation in the lower thermal region for various cases ([5], [6]). The value for b used in the energy group structure of the current thesis is 0.5165, which corresponds to a neutron energy of $3 \cdot 10^{-3}$ eV. The residual equations are obtained by weighting the neutron lethargy balance equation with the basis functions themselves, rather than a separate set of test functions (Galerkin weighting).

3.3 Computational implementation

3.3.1 Reference environmental calculations

Reference environmental data for cross sections, reaction rates and the multiplication factor are obtained from the TRITON-NEWT sequence of the SCALE code system. First a cross section library is prepared based on ENDF/B-VII.1 for input isotopic compositions and temperatures. Processing of these cross sections involves 1D resonance self-shielding calculations using the multiregion approach of the CENTRM and PMC modules of SCALE. Subsequently a 2D lattice transport criticality calculation is performed on a checkerboard configuration of fuel pins or assemblies, with reflective boundary conditions in a fine energy group structure with 252 groups. The transport calculation is performed using the NEWT discrete ordinates module in S_6 quadrature. Using the flux distribution from the transport calculation the cross sections are homogenized to a four-nodes-per-pin mesh and collapsed to the two energy group structure. Detailed descriptions of the SCALE sequences can be found in the SCALE manual [12].

The configurations for which the rehomogenization assessment is performed are described below.

Pin checkerboards

Infinite checkerboard patterns of two fuel pin types provide possible test cases with a simple heterogeneity, as opposed to assembly colorsets where the heterogeneity is more complex. Performing rehomogenization calculations on these configurations serves a multitude of purposes: validation of the rehomogenization basis functions, base error estimation and parametric study. Whereas in realistic layouts, where heterogeneities occur mostly at the assembly interface, spectral effects can effectively be smoothed out over several unit cell lengths, this is not the case in checkerboard configurations. Consequently spectral effects are more severe. A simple example is a checkerboard of UO_2 fuel pins, alternating between two different enrichments. In this example the degree of heterogeneity can be described by a single metric; the fuel enrichment. The checkerboard configuration is illustrated in Figure 3.1.

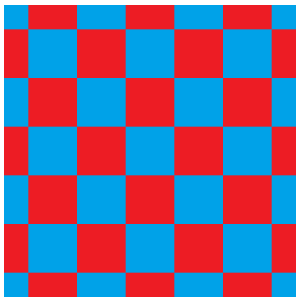

Figure 3.1: The pin checkerboard configuration. Both colors correspond to a specific pin type. Reflective boundary conditions apply on all sides.

Assembly colorsets

The assembly colorset provides a more realistic configuration, that is, one that closely resembles a possible configuration in a real pressurized water reactor. Using this configuration an actual assessment can be made regarding the suitability of the spectral rehomogenization method for pin-by-pin nodal diffusion calculations. In order to maintain simplicity the zirconium grid spacers and water

gaps that separate respectively the fuel pins and assemblies in real core configurations are ignored, since, although their contribution is not negligible near the assembly interface, they only weakly affect the neutronics compared to inter-pin heterogeneities. A sample colorset configuration is illustrated in Figure 3.2.

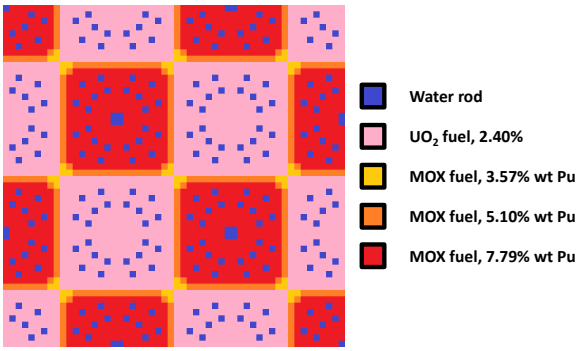

Figure 3.2: Example of an assembly colorset, a checkerboard configuration of fuel assemblies. Reflective boundary conditions apply on all sides.

3.3.2 Infinite-medium cross sections and discontinuity factors

Unit cell infinite-medium data are computed using the same sequences of the SCALE package as those that yield the reference environmental data. The NEWT S_6 discrete ordinates problem is solved for a quarter-cell, thereby exploiting the unit cell symmetry. The broad-group collapsed cross sections and discontinuity factors are input to the nodal calculation. The non-collapsed fine group cross sections are used for the off-line calculation of rehomogenization parameters defined in equations (3.2.1), (3.2.1) and (3.2.1).

The quarter-cell infinite medium homogenization cannot be employed for unit cells which contain no fissionable material, such as water rods and burnable absorbers, since a non-zero infinite medium flux is needed as a weighting function. Instead these cells are homogenized following a transport calculation in a configuration of 3×3 cells, where the non-fissile cell is surrounded by the most common fuel cell in the corresponding assembly. Such a configuration is displayed in Figure 3.3. The 3×3 configuration is chosen since it maintains the three pin spacing between the water rods located near the center of the 17×17 UOX fuel assembly. Cross sections for water rods have been obtained and compared with data from a single assembly calculation at infinite medium conditions, the results of which are reported in Appendix A. The deviations of the 3×3 cross sections from the assembly data turn out to be of comparable magnitude to those of the fuel pins.

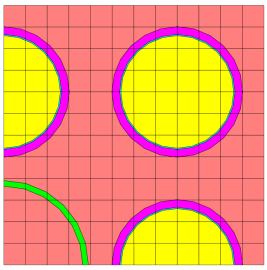

Figure 3.3: An example of the 3×3 configuration used to obtain homogenized data for cells containing no fissile material. In this particular example a water channel is homogenized in an environment of UO_2 fuel rods. Reflective boundary conditions apply on all sides.

3.3.3 Nodal calculations and rehomogenization

For the nodal diffusion calculations and the rehomogenization of cross sections a TU Delft in-house code, BRISINGR, is used.

This solver collects input infinite medium cross sections from the AMPX libraries supplied by the SCALE output, as well as the discontinuity factors. The rehomogenization coefficients are calculated using the fine-group cross section data from SCALE and input basis functions. After setting up the geometry, the code solves the fixed fission source problem iteratively via a Krylov subspace method. Subsequently the eigenvalue is re-evaluated, a correction to the nodal coupling is determined following the NEM solution and a new cycle of inner iterations begins. This double iteration cycle is repeated until convergence of the eigenvalue.

A third iterative cycle is introduced in which equations (3.25) are solved using the solution to the nodal calculation, leading to determination of the expansion coefficients $\beta^k_{i,g}$. These are used to calculate the spectral corrections $\delta\Sigma^k_{q,g}$, which along with the infinite-medium cross sections are input to a new nodal calculation. The iteration of nodal calculations with rehomogenization updates goes on until the eigenvalue has also converged in the rehomogenization problem. Iterations between nodal updates and rehomogenization can be nested in thermal-hydraulic feedback updates in industrial calculations [16]. Consequently costs from iterating the nodal calculation are amortized. BRISINGR yields output fluxes, multiplication factor and corrected cross sections.

The above procedure is visualized in Figure 3.4.

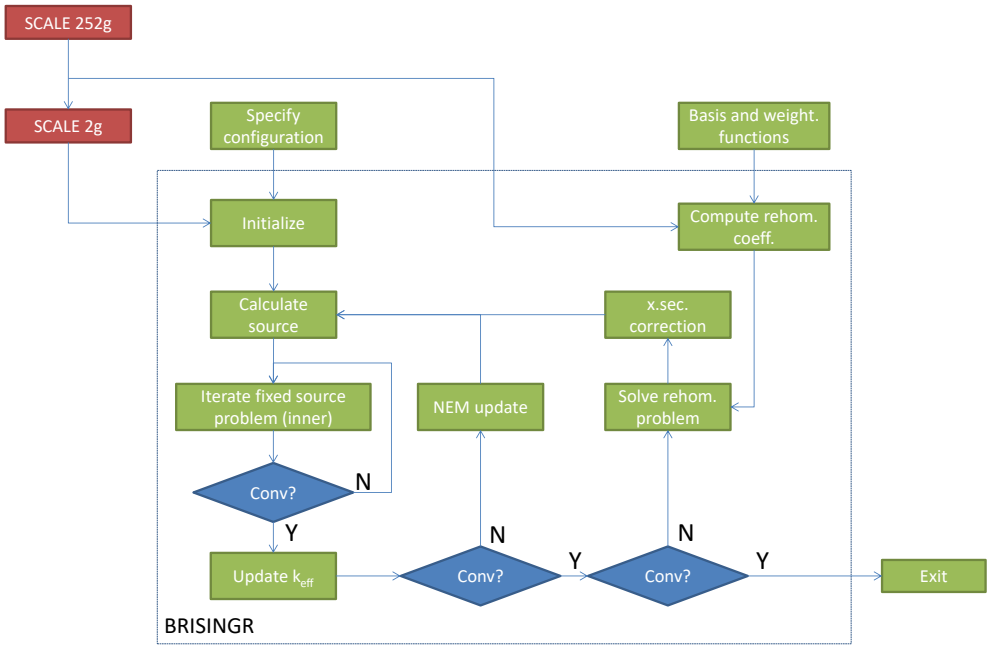

Figure 3.4: General flow diagram of the rehomogenization method, including the three-cycle iterative scheme.

In the present thesis the leakage lethargy distributions $L^k_g(u)$, required to constitute the weighted residual rehomogenization problem, are assumed to be known. As such, they are taken as input from the fine-group reference environmental calculation output. The results consequently represent an idealized outlook on the rehomogenization method, in which it is assumed that the leakage lethargy shapes can be perfectly reconstructed. A model describing the leakage lethargy shape using only nodal diffusion data is currently under development at TU Delft ([6], [16]).

Chapter 4

Results

4.1 Base error estimation

Before being able to assess the results of the calculations performed in this thesis it is necessary to obtain an order-of-magnitude estimation of the base errors, that is, the errors in integral parameters and cross sections that cannot be attributed to homogenization defects. To this end we present the results of a pin checkerboard configuration of 1.80 % enriched UO_2 cells with identical neighbours. In principle the cross section errors and therefore the cross section corrections should be zero, since this checkerboard pattern is physically equivalent to the infinite lattice of 1.80 % UO_2 cells. The deviation of these errors and corrections from zero thus provide ballpark uncertainty estimations for errors from other calculations. They should be sufficiently small compared to the errors from subsequent calculations to confirm the significance of the latter.

Aside from the reference environmental transport calculation, the following calculations are performed:

- A standard pin-by-pin nodal diffusion calculation, with no cross section correction (a),
- A nodal calculation with fourth order rehomogenization in both the fast and thermal group (b),
- A nodal calculation with correction of the cross sections using the reference spectrum variations (c), and
- A nodal calculation using reference environmental cross sections (d).

From these calculations the following results are compared:

- the deviation from the reference mulitplication factor in pcm
- the deviation from the reference fission power in %
- the deviation from the reference cross sections, Σ_t, Σ_a, $\nu\Sigma_f$, $\Sigma_{s,g\neq g'}$, $\Sigma_{s,g=g'}$, in %

The results are presented in Tables 4.1, 4.2 and 4.3.

Table 4.1: Pin-by-pin cross section base error estimates for absorption, nu-fission reactions and total of reactions.

UO_2 1.8 %	$\Sigma_{a,1}$	$\Sigma_{a,2}$	$\nu\Sigma_{f,1}$	$\nu\Sigma_{f,2}$	$\Sigma_{t,1}$	$\Sigma_{t,2}$
Reference $[cm^{-1}]$	0.00967	0.0743	0.00538	0.0920	0.540	1.26
Simulation			Error %			
No rehom. (a)	0.000164	0.000030	-0.00482	0.000032	-0.000519	0.000047
Spec. rehom. (b)	-0.00377	-0.000182	-0.00686	-0.000187	-0.00142	-0.000165
Σ corr. with ref. $\delta\phi$ (c)	-0.000306	0.000068	-0.00535	0.000070	-0.000626	-0.000029

(a)

Table 4.2: Base error estimates for scattering cross sections.

UO_2 1.8 %	$\Sigma_{s,1\to1}$	$\Sigma_{s,1\to2}$	$\Sigma_{s,2\to1}$	$\Sigma_{s,2\to2}$
Reference $[cm^{-1}]$	0.514	0.0166	0.00143	1.19
Simulation	Error %			
No rehom. (a)	0.000116	0.00154	0.000122	-0.000121
Spec. rehom. (b)	-0.000832	-0.00686	0.00154	-0.000234
Σ corr. with ref. $\delta\phi$ (c)	-0.000249	-0.000861	-0.000126	-0.000103

Table 4.3: Comparison of multiplication factor and fission power distribution errors.

Simulation	Δk_{eff} [pcm]	$\Delta P_{avg}(\%)$
No rehom. (a)	-9.78	$< 10^{-5}$ (abs)
Spec. rehom. (b)	-9.85	$< 10^{-5}$ (abs)
Σ corr. with ref. $\delta\phi$ (c)	-9.74	$< 10^{-5}$ (abs)
Ref. env. Σ (d)	-15.1	$< 10^{-5}$ (abs)

The errors presented in Tables 4.1 and 4.2 for calculation *(a)* present mainly the consistency of the SCALE lattice transport calculations. It can also be seen that, while strictly speaking the absolute value of the cross section errors increases after rehomogenization, they remain small compared to typical cross section errors which are in the order of several percents. The errors on the integral parameters suggest that a k_{eff} error increase or reduction of several tens of pcm may not be significant, and that pin-by-pin nodal calculations with infinite medium cross sections lead to very small fission power errors with respect to the analogous refined lattice transport calculations.

4.2 Validation in pin checkerboard configurations

The approach to the basis functions defined in subsection 3.2.2 has been validated for cross section rehomogenization at the assembly level [6], but not at the pin-by-pin level.

Before proceeding with rehomogenization in colorset configurations, the choice of basis functions must be validated by confirming that the reference spectrum variation can be adequately reconstructed by rehomogenization using these basis functions and by evaluating the reduction of the errors in cross section, reaction rates and multiplication factor for some test cases.

4.2.1 Checkerboard of 1.80 % and 3.10 % UO_2 pins

As a first test case we consider a pin checkerboard configuration of UO_2 fuel cells with 1.80 % enrichment neighbouring 3.10 % enriched UO_2 cells, displayed schematically in Figure 4.1. A detailed description of the material compositions and geometrical parameters for this configuration is given in Appendix B.1.1.

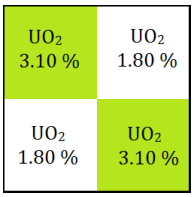

Figure 4.1: Schematic layout of the 1.80% and 3.10 % UO_2 pin checkerboard.

From the rehomogenization calculation with a fourth-order expansion (b) on the checkerboard configuration of 1.80 % and 3.10 % UO_2 pin cells we plot the spectrum variation reconstruction, that is, the approximation of:

$$\delta\phi_G^k(u)[\%] = 100\% \frac{\phi_G^{env,k}(u) - \bar{\phi}_G^k \varphi_G^{\infty,k}(u)}{\bar{\phi}_G^k}, \tag{4.1}$$

in Figure 4.2.

The rehomogenization expansion seems to be well able to follow the general trends of the flux energy dependence, both in the fast and thermal group. However, there are some substantial deviations from the reference environmental spectrum variation in the epithermal range and in the fission emission range. It seems reasonable that the expansion is unable to reconstruct the edged behaviour around $u = 0.75$ in the fast group, from the limitations of fourth order expansion in general.

The thermal spectrum in the 1.80 % UO_2 cell is hardened by the excess thermalized neutrons flowing in from the 3.10 % cell, with reference spectrum variation locally exceeding 20 % of the node-average flux. Conversely the 3.10 % cell experiences a softened thermal spectrum due to leakages into the 1.80 % cell, which has a slightly smaller absorption cross section, but also substantially fewer fission events are induced here.

Spectrum variations in the fast macro-group are of smaller magnitude, due to streaming playing a more dominant role over absorption, leading to smaller flux gradients. The fission emission spectrum correlates to the thermal flux softening, as a strong negative correlation exists between incident neutron energy and fission cross section in the thermal region.

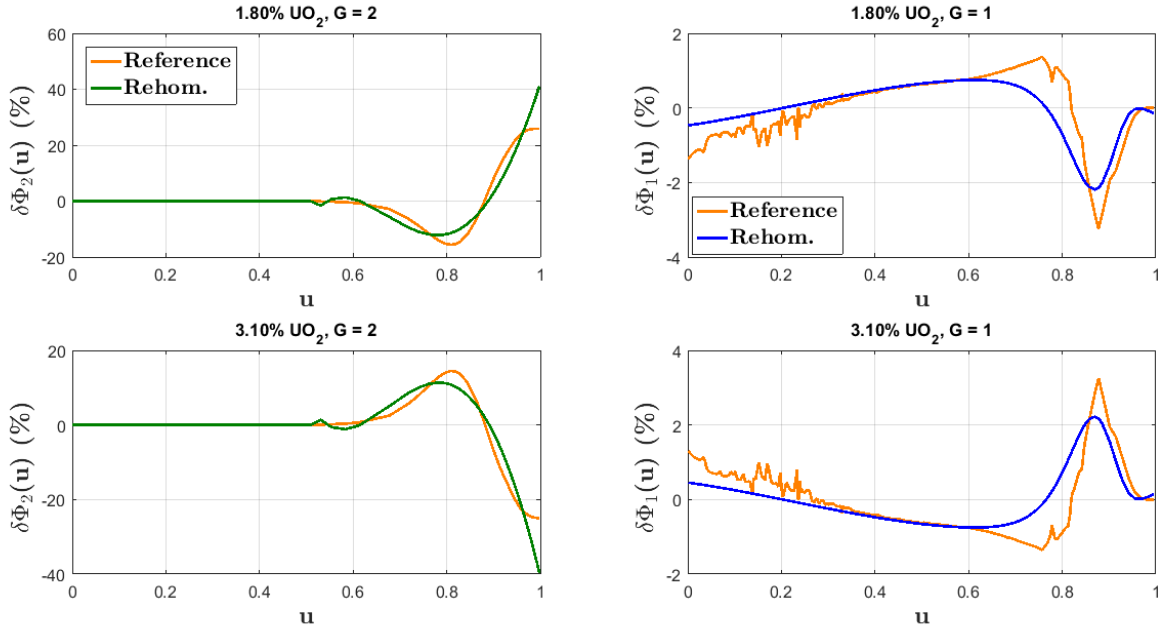

Figure 4.2: Reference spectrum variation and its reconstruction from the solution of the rehomogenization problem, for both cell types of the 1.80% / 3.10% UO_2 pin checkerboard configuration.

The effect of the spectrum variation reconstruction on the group cross sections depends also on the infinite medium cross sections for the reactions considered. In Figures 4.3 and 4.4 the infinite medium cross sections for absorption and fission neutron production are displayed for both cell types.

Qualitatively speaking, in the 1.80 % cell the rehomogenization spectrum variation in the thermal group is zero from $u = 0$ until $u \approx 0.5$, then negative until $u \approx 0.9$ and then positive until $u = 1$. The corresponding infinite medium absorption cross section lethargy distribution decreases as it approaches $u = 1$. The cross section in the lethargy region corresponding to the positive spectrum

variation is small compared to the cross section in the region corresponding to negative spectrum variation. For the 3.10 % cell, the opposite is the case. From this we predict (intuitively) that the cross section correction will be negative for the former and positive for the latter. In the fast group the global behaviour cannot be predicted in this way, due to the many resonances and overall more irregular behaviour. We can predict however that the magnitude of the cross section corrections must be substantially smaller than those in the thermal group. Furthermore we can see that the cross section behaviour in the fast group is mainly dependent on these resonances, and predict that a better reconstruction of the spectrum variation in the epithermal region will lead to a more accurate correction on the absorption and fission neutron production group cross sections, shown in Table 4.4.

Table 4.4: Spectral cross section changes with respect to the infinite medium values (%) using the rehomogenization spectrum variation, for the absorption and fission neutron production cross sections in the 1.80 % / 3.10 % UO_2 pin checkerboard.

	$\delta\Sigma_{a,1}^{(spec)}$ (%)	$\delta\Sigma_{a,2}^{(spec)}$ (%)	$\delta\nu\Sigma_{f,2}^{(spec)}$ (%)	$\delta\nu\Sigma_{f,2}^{(spec)}$ (%)
UO_2 1.80 %	0.0131	-2.25	-0.357	-2.34
UO_2 3.10 %	-0.0175	2.14	0.267	2.20

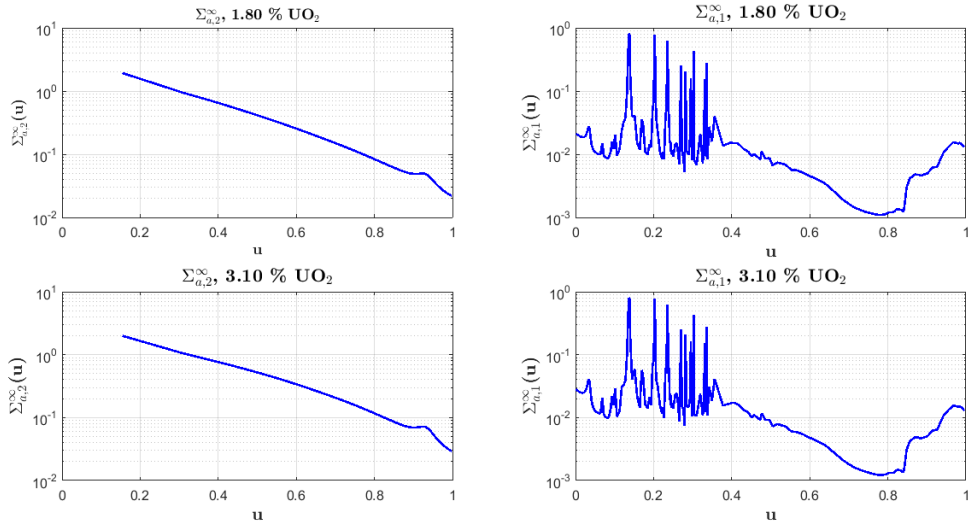

Figure 4.3: Infinite medium absorption cross section lethargy profile for both cell types of the 1.80% / 3.10% UO_2 pin checkerboard configuration.

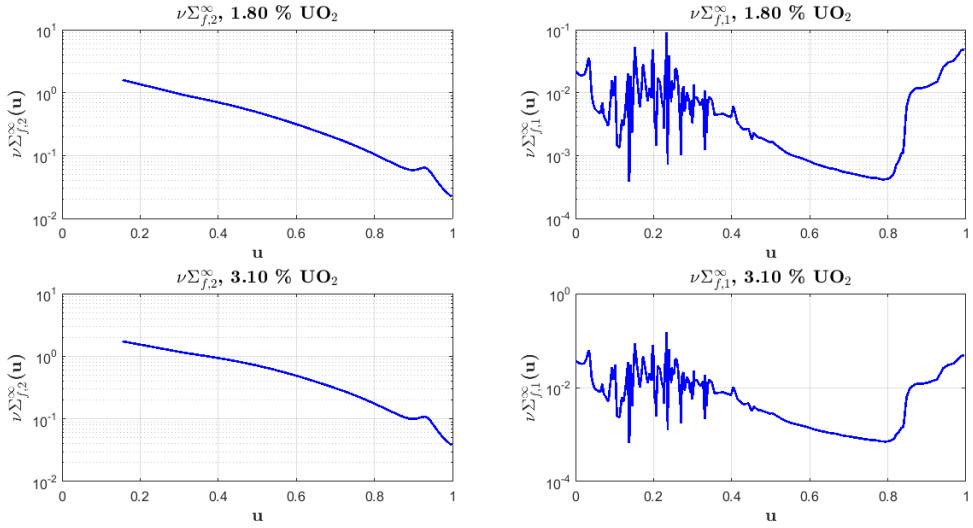

Figure 4.4: Infinite medium fission neutron production cross section lethargy profile for both cell types of the 1.80% / 3.10% UO_2 pin checkerboard configuration.

Nevertheless, the spectral rehomogenization method, as can be seen in Tables 4.5 and 4.6, shows promising results regarding the reduction of the cross section errors, specifically in the thermal group, where the spectrum variation reconstruction is more accurate. However, a slight overcorrection is visible in the thermal group in both cell types. This seems predominantly caused by the spectrum variation overestimation (in absolute terms) in the region sepcified by (approximately) $0.65 < u < 0.75$. A more accurate spectrum reconstruction would lead to better cross section corrections in the fast group as well, as discussed above for the absorption and nu-fission cross sections and as shown by calculation (c).

Table 4.5: Pin-by-pin cross section errors (%), for the absorption and nu-fission reactions and the total of reactions, for the 1.80 % / 3.10 % UO_2 pin checkerboard configurations

UO_2 1.8 %	$\Sigma_{a,1}$	$\Sigma_{a,2}$	$\nu\Sigma_{f,1}$	$\nu\Sigma_{f,2}$	$\Sigma_{t,1}$	$\Sigma_{t,2}$
Reference $[cm^{-1}]$	0.00960	0.0728	0.00528	0.0901	0.541	1.25
Simulation			Error %			
No rehom. (a)	0.644	2.06	1.96	2.22	-0.101	0.970
Spec. rehom. (b)	0.657	-0.229	1.60	-0.175	0.102	-0.264
Σ corr. with ref. $\delta\phi$ (c)	0.272	0.128	1.08	0.215	0.0277	-0.0598

(a)

UO_2 3.1 %	$\Sigma_{a,1}$	$\Sigma_{a,2}$	$\nu\Sigma_{f,1}$	$\nu\Sigma_{f,2}$	$\Sigma_{t,1}$	$\Sigma_{t,2}$
Reference $[cm^{-1}]$	0.0107	0.101	0.00748	0.150	0.538	1.29
Simulation			Error %			
No rehom. (a)	-0.647	-1.91	-1.58	-2.02	0.101	-0.926
Spec. rehom. (b)	-0.664	0.186	-1.32	0.136	-0.106	0.256
Σ corr. with ref. $\delta\phi$ (c)	-0.246	-0.162	-0.783	-0.228	-0.0282	0.0542

(b)

Table 4.6: Scattering cross section errors(%).

	UO_2 1.8 %				UO_2 3.1 %			
	$\Sigma_{s,1\to1}$	$\Sigma_{s,1\to2}$	$\Sigma_{s,2\to1}$	$\Sigma_{s,2\to2}$	$\Sigma_{s,1\to1}$	$\Sigma_{s,1\to2}$	$\Sigma_{s,2\to1}$	$\Sigma_{s,2\to2}$
Reference $[cm^{-1}]$	0.515	0.0163	0.00164	1.18	0.511	0.0161	0.00167	1.18
Simulation	Error %				Error %			
No rehom. (a)	-0.172	1.73	-12.8	0.922	0.172	-1.68	12.2	-0.860
Spec. rehom. (b)	0.0613	1.08	6.07	-0.275	-0.0657	-1.05	-5.78	0.270
Σ corr. with ref. $\delta\phi$ (c)	0.0245	-0.00126	-0.00098	-0.0716	-0.0250	0.00063	0.00076	0.0728

Table 4.7: Comparison of multiplication factor and fission power distribution errors and number of rehomogenization iterations.

			UO_2 1.8 %	UO_2 3.1 %
Simulation	No. rehom. iter	Δk_{eff} [pcm]	$\Delta P_{avg}(P_{g=1}, P_{g=2})(\%)$	$\Delta P_{avg}(P_{g=1}, P_{g=2})(\%)$
No rehom. (a)	-	-188	2.72 (2.73, 2.72)	-1.71 (-1.88, -1.67)
Spec. rehom. (b)	8	-36.6	0.465 (2.35, -0.0914)	-0.292 (-1.62, 0.0560)
Σ corr. with ref. $\delta\phi$ (c)	-	-54.0	0.669 (1.73, 0.356)	-0.421 (-1.19, -0.218)
Ref. env. Σ (d)	-	-34.8	0.230 (0.732, 0.0832)	-0.145 (-0.504, -0.0510)

The errors on both integral parameters (multiplication factor and fission powers) are substantially reduced by rehomogenization as well, again especially the fission rate in the thermal group. It is suggested that this is mainly a consequence of the thermal group nu-fission cross section error reduction, provided that the thermal flux error is limited. This will be investigated more thoroughly in section 4.3.

Eight rehomogenization iterations are required for this problem. Therefore, the computational burden would increase about eightfold compared to a standard nodal calculation if no thermal-hydraulic feedback is considered.

4.2.2 Checkerboard of 2.40 % UO_2 and 3.57 % MOX pins

Another test case considered is a checkerboard configuration of double-clad 2.40 % UO_2 pins neighbouring MOX fuel pins with 3.57 wt% PuO_2. We consider this checkerboard to validate the set of basis functions also for pin-by-pin heterogeneities that are not characterized solely by enrichment differences.

This configuration is displayed schematically in Figure 4.5.

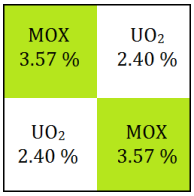

Figure 4.5: Schematic layout of the (UO_2 2.40% + MOX 3.57 %) pin checkerboard.

Rehomogenization leads to the spectrum variation reconstruction displayed in Figure 4.6. The spectrum variation in the thermal group is of a magnitude vastly larger than that observed in the 1.80 % / 3.10 % UO_2 checkerboard, approaching 100 % of the node-average flux near the macro-group boundary. With assembly-level homogenization, no local spectrum variations have been found that

exceed 40 % [16]. This can be partly explained by the large thermal-to-fast absorption cross section ratio of the MOX fuel cell, compared to that of the UO_2 cell as derived from the reference cross section values in Table 4.8, suggesting a vastly harder spectrum overall. The spectrum variation reconstruction by rehomogenization is performed well in the thermal group. In the fast group the reconstruction is able to approximate the value at the 0.625 eV energy boundary, but it overestimates the reference spectrum variation subsequently. While to some extent able to follow the global trend, the reconstruction fails to reproduce the fission emission spectrum. This is of limited impact to the fission and absorption cross sections, as their contributions from the fission emission region are limited. On the other hand it has large consequences for the fast-group self-scattering cross section, which predominantly determines the magnitude of the fast group total cross section. However, since self-scattering at the macro-group level provides zero net contribution to the neutron flux, the effect on reactor behaviour is limited.

This is reflected in the macro-group cross section corrections displayed in Tables 4.8 and 4.9. Thermal group cross section errors are reduced over the whole range, including the up-scattering cross sections, albeit subject to a slight overcorrection. Fast group down-scattering cross sections are subject to large errors in the infinite-medium case. These errors are sharply reduced following rehomogenization. Another vast improvement is observed in the fast group absorption cross sections, both for the UO_2 and the MOX fuel pins. Fast group self-scattering cross sections, however, deteriorate following rehomogenization and so do the total cross sections, as they are predominantly determined by self-scattering.

Interestingly, in the MOX fuel cell, relatively large thermal cross section errors persist even after reference spectrum correction (c), suggesting also a strong spatial effect. This may in part be due to a higher total cross section, meaning a smaller thermal neutron mean free path, as well as a large absorption cross section that can lead to large intra-nodal flux gradients.

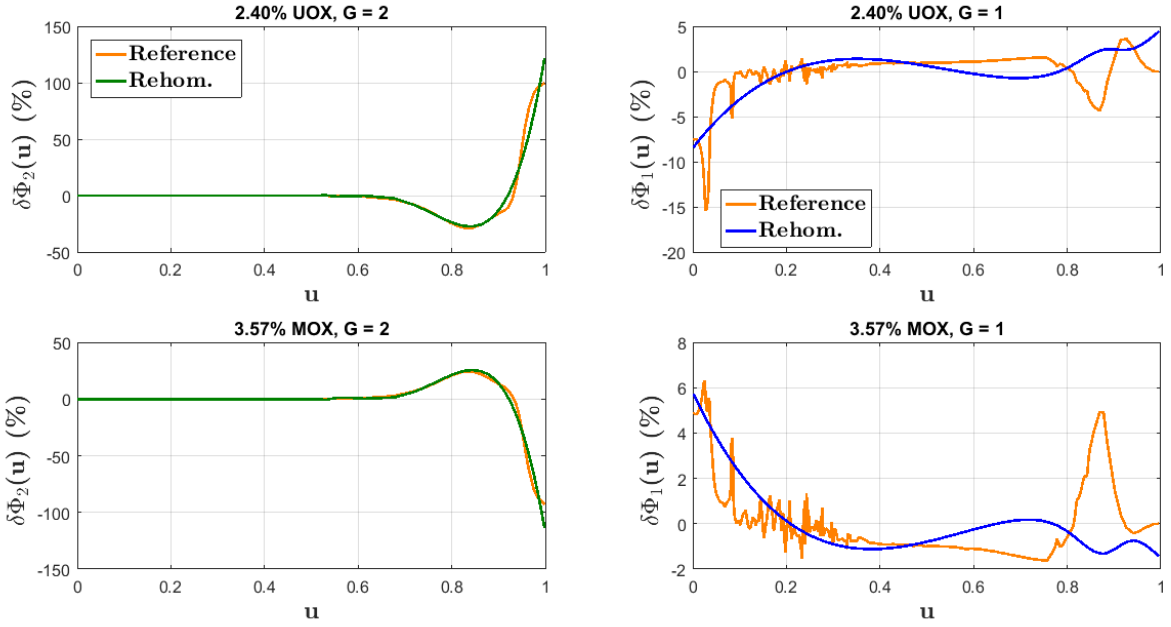

Figure 4.6: Reference spectrum variation and reconstruction for both energy groups in both cell types of the (UO_2 2.40% + MOX 3.57 %) pin checkerboard.

Results on the global performance indicators are displayed in Table 4.10. The multiplication factor k_{eff} improves vastly, as well as the power distributions, albeit not as much as in the 1.80 % / 3.10 % UO_2 case. A better pin power improvement is however achieved in calculation (d), implying that the spatial effects noted above also have large consequences on the pin power distribution.

The number of rehomogenization iterations is larger than that of the 1.80 % / 3.10 % UO_2 case, however, in an absolute sense these numbers are dependent on the set tolerances for convergence.

Table 4.8: Pin-by-pin cross section errors (%), for the absorption and nu-fission reactions and the total of reactions, for the 2.40 % UO_2 / 3.57 % MOX pin checkerboard configuration.

UO_2 2.40 %	$\Sigma_{a,1}$	$\Sigma_{a,2}$	$\nu\Sigma_{f,1}$	$\nu\Sigma_{f,2}$	$\Sigma_{t,1}$	$\Sigma_{t,2}$
Reference $[cm^{-1}]$	0.00994	0.0918	0.00583	0.106	0.535	1.25
Simulation			Error %			
No rehom. (a)	1.27	3.97	3.25	4.49	-0.176	1.65
Spec. rehom. (b)	0.169	0.612	3.35	0.958	-0.351	-0.0515
Σ corr. with ref. $\delta\phi$ (c)	0.471	0.325	1.80	0.657	0.0451	-0.181

(a)

MOX 3.57 %	$\Sigma_{a,1}$	$\Sigma_{a,2}$	$\nu\Sigma_{f,1}$	$\nu\Sigma_{f,2}$	$\Sigma_{t,1}$	$\Sigma_{t,2}$
Reference $[cm^{-1}]$	0.0141	0.214	0.00765	0.298	0.534	1.41
Simulation			Error %			
No rehom. (a)	-4.96	-2.88	-2.58	-3.33	-0.0454	-1.44
Spec. rehom. (b)	-1.19	-1.60	-2.14	-1.94	0.292	-0.104
Σ corr. with ref. $\delta\phi$ (c)	-1.06	-1.23	-1.48	-1.53	-0.0683	0.0279

(b)

Table 4.9: Scattering cross section errors(%).

	UO_2 2.40 %				MOX 3.57 %			
	$\Sigma_{s,1\to1}$	$\Sigma_{s,1\to2}$	$\Sigma_{s,2\to1}$	$\Sigma_{s,2\to2}$	$\Sigma_{s,1\to1}$	$\Sigma_{s,1\to2}$	$\Sigma_{s,2\to1}$	$\Sigma_{s,2\to2}$
Reference $[cm^{-1}]$	0.510	0.0147	0.00254	1.16	0.506	0.0143	0.00268	1.20
Simulation			Error %				Error %	
No rehom. (a)	-0.158	11.0	-30.9	1.54	0.290	-7.06	27.1	-1.25
Spec. rehom. (b)	-0.353	-0.431	3.29	-0.111	0.293	1.65	-3.27	0.170
Σ corr. with ref. $\delta\phi$ (c)	0.0413	-0.0953	-0.0159	-0.222	-0.0459	0.115	0.0167	0.252

Table 4.10: Comparison of multiplication factor and fission power distribution errors and number of rehomogenization iterations.

			UO_2 2.40 %	MOX 3.57 %
Simulation	No. rehom. iter	Δk_{eff} [pcm]	$\Delta P_{avg}(P_{G=1}, P_{G=2})(\%)$	$\Delta P_{avg}(P_{G=1}, P_{G=2})(\%)$
No rehom. (a)	-	1100	5.66 (4.31, 6.60)	-3.01 (-3.59, -2.95)
Spec. rehom. (b)	17	316	3.30 (4.13, 2.88)	-1.76 (-3.44, -1.29)
Σ corr. with ref. $\delta\phi$ (c)	-	45.8	2.60 (2.93, 2.42)	-1.38 (-2.44, -1.08)
Ref. env. Σ (d)	-	0.260	0.983 (1.11, 0.926)	-0.523 (-0.923, -0.414)

4.2.3 Summary

It has been estabilished, from the two test cases considered in this section, that spectral rehomogenization applied to pin-by-pin checkerboard systems leads to substantial reductions on the thermal cross section errors, pin power distributions and the multiplication factor k_{eff}. This is consistent with the error reductions following cross section corrections using the reference spectrum variations, which are approximated well by rehomogenization in the thermal group. While reference spectrum corrections also significantly reduce cross section errors in the fast group, the present implementation of the rehomogenization method is not capable of consistently reproducing these error reductions. Spectrum variations for the UO_2 / MOX checkerboard are large, near 100 % of the node-average flux in the thermal group. This degree of spectrum variation has not been observed at the assembly level.

4.3 Parametric study - heterogeneity

4.3.1 Cross section, pin power and multiplication factor error

We are interested in the dependence of the rehomogenization performance on the degree of heterogeneity between pin cells. To this end the simulations (*a*-*d*), described in section 4.1, are performed for pin checkerboards, consisting of UO_2 pins alternating between two enrichments. One enrichment is kept fixed at 1.80 %, whereas the enrichments in the neighbouring cells are varied between the following values: 1.60 %, 1.80 %, 2.00 %, 2.20 %, 2.40 %, 2.60 %, 3.10% and 3.60 %. Consequently the enrichment difference is treated as a parameter characterizing the heterogeneity between pins.

The layout of the checkerboard and the material compositions of the UO_2 fuels, cladding and moderator are described in detail in Appendix B.1.1. The results of the calculations performed on these checkerboard configurations are compared to those of their respective reference transport calculations. The solutions and resulting cross sections of the latter are displayed in Appendix C.
It should be noted that the configurations, in which the pins with varying enrichments assume enrichments 1.80 % and 3.10 %, are identical to the configurations considered in sections 4.1 and 4.2.1 respectively. The deviations from the reference cross sections are displayed per simulation type as a function of the enrichment difference in Figures 4.7, 4.8, 4.9, 4.10 and 4.11.

First the errors on the total cross section in the thermal group ($G = 2$) are considered. The error on the nodal diffusion calculation without rehomogenization (*a*) increases steeply with heterogeneity as the reflective boundary conditions for the infinite medium calculations are violated to increasing extent. The calculations employing spectral rehomogenization (*b*) also show errors increasing with heterogeneity, but substantially less steeply. Even for larger heterogeneity the thermal total cross sections resulting from spectral rehomogenization follow the reference spectrum-corrected cross sections (*c*) closely, which themselves show little deviation from the reference environmental cross sections. Errors still present in (*c*) may be due to spatial effects, for which the reference spectrum correction does not account.

The total cross section errors in the fast group, on the other hand, seem to be reduced initially, but for larger heterogeneities are subject to large overcorrections. This may be a result of the limited ability to reconstruct the spectrum variation near the energy group boundary. This will be further discussed in subsection 4.3.2.

For small heterogeneity the thermal group absorption cross sections from rehomogenization follow the reference spectrum corrected cross sections closely. However, at enrichment differences larger than 1 % they are subject to the same overcorrections observed in the thermal total cross sections.

For the absorption cross section the spectral rehomogenization method also fails to reduce the error magnitude in the fast group, but in contrast to the case of the total cross section, the value of the cross section is shifted in the wrong direction, rather than being subject to an overcorrection. A discussion on the influence of the spectrum variation reconstruction on this behaviour follows also in 4.3.2.

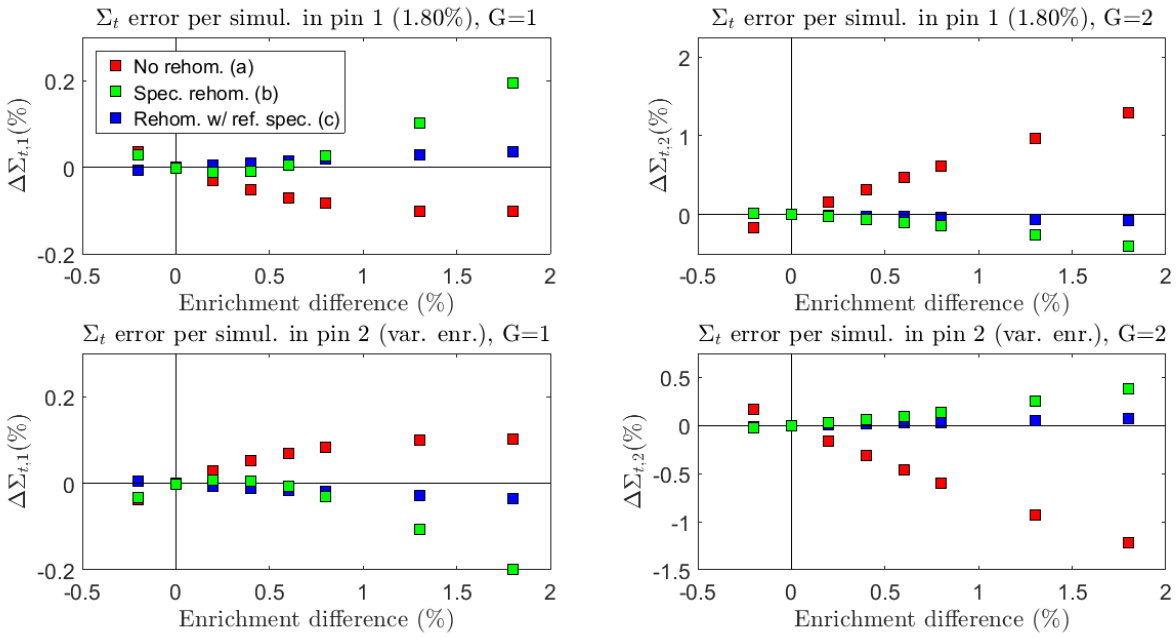

Figure 4.7: Total cross section errors for the varying enrichment pin checkerboard, per pin type, per group, for each simulation, plotted against the enrichment difference.

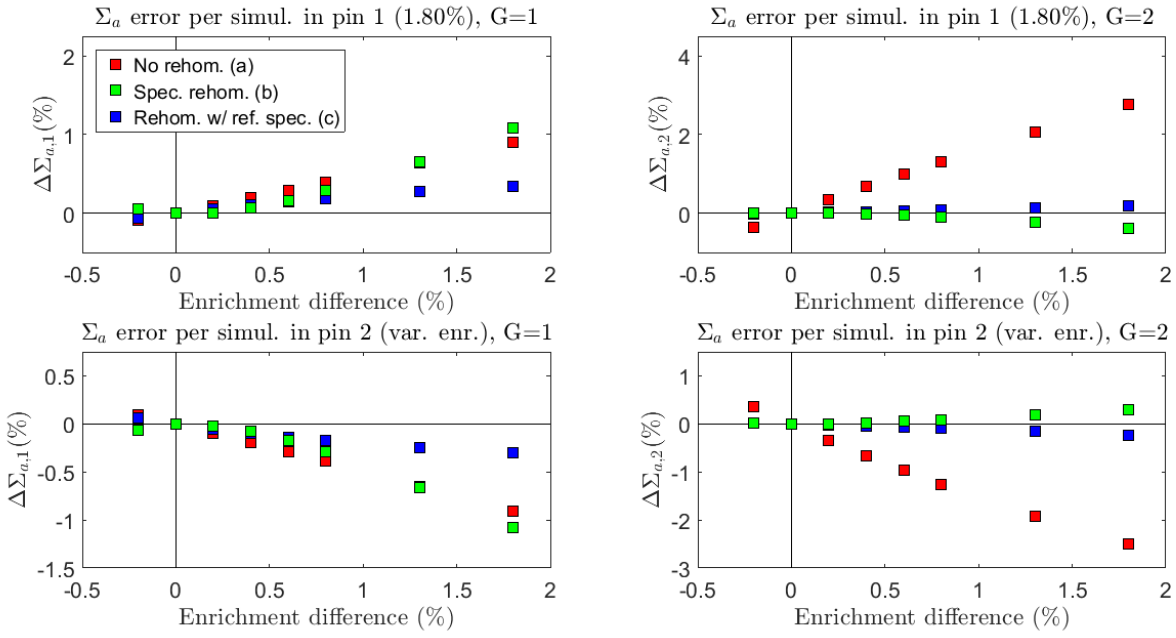

Figure 4.8: Absorption cross section errors for the varying enrichment pin checkerboard, per pin type, per group, for each simulation, plotted against the enrichment difference.

As for the fission neutron production cross section, both the fast group and the thermal group errors show error magnitude reduction following rehomogenization, despite slight overcorrections in the thermal group. Though the error magnitude following the spectral rehomogenization (b) is smaller than the error magnitude following the reference spectrum correction (c) in the thermal group, it should be understood that (b) is an approximation to the (c). As such, in order to obtain an impression

of the inaccuracy of (b), one should add the difference between errors from (b) and (c) to the error magnitude from calculation (c). Taking this into account, nevertheless, the error reduction with respect to the nodal calculation without rehomogenization is quite substantial. The error reduction in the fast group however is less pronounced. Another observation from the fast group fission neutron production result is that the cross section error reduction following a reference spectrum correction is limited, indicating a non-negligible spatial effect.

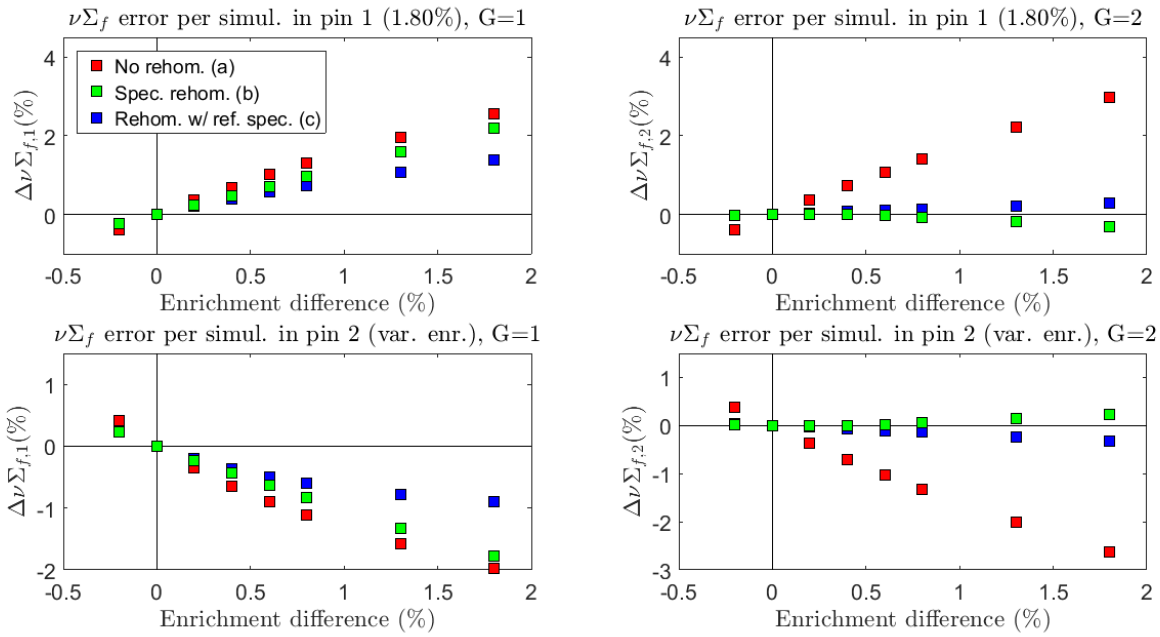

Figure 4.9: Fission neutron production cross section errors for the varying enrichment pin checkerboard, per pin type, per group, for each simulation, plotted against the enrichment difference.

We consider also the cross sections characterizing the scattering reactions, within one energy group as well as between the two groups. As for cross-group scattering, it is observed that cross section errors must be caused mainly by spectral effects, since a perfect spectrum reconstruction reduces the error to near zero. Rehomogenization of both the cross- and self-scattering cross sections to the first group leads to an overcorrection, although the error magnitude is reduced still. The same holds for the self-scattering in the second group. Whereas errors on the up-scattering from the thermal group are typically large compared to other cross section errors, up-scattering cross sections are generally small, meaning even errors exceeding 15 % have little impact on overall reactor behaviour.

Regarding the general behaviour for all cross sections, it has been noted earlier, in section 4.2.1, that cross sections in the thermal macro-group are generally subject to environmental effects of larger magnitude than those in the fast group and that this is likely a result of stronger flux gradients.

Concerning the overall reactor behaviour in terms of multiplication factor and power production, it becomes apparent from Figure 4.12 that spectral rehomogenization reduces the errors in these parameters as well. From the environmental reference data in Appendix C it can be determined that the fission rate $\Sigma_f\phi$ in the thermal group is approximately three times larger than that in the fast group. As a consequence the fission cross section error reduction from the thermal group weighs in about three times more heavily in the overall power production error, provided that the errors on the node-average fluxes are of limited magnitude.

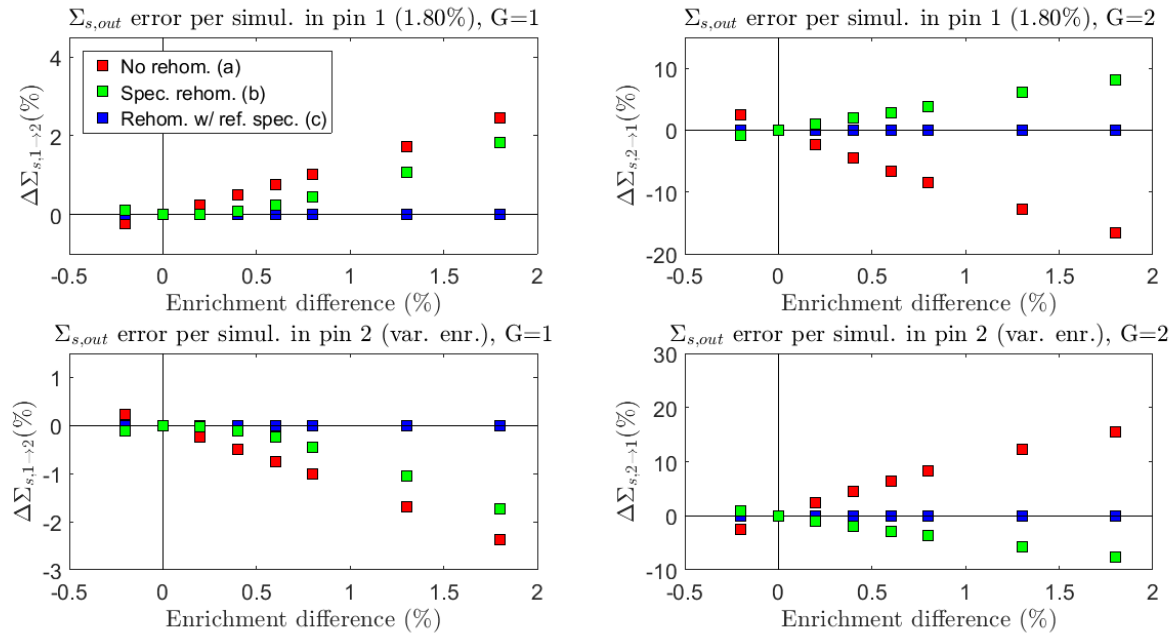

Figure 4.10: Out-scattering cross section errors for the varying enrichment pin checkerboard, per pin type, per group, for each simulation, plotted against the enrichment difference.

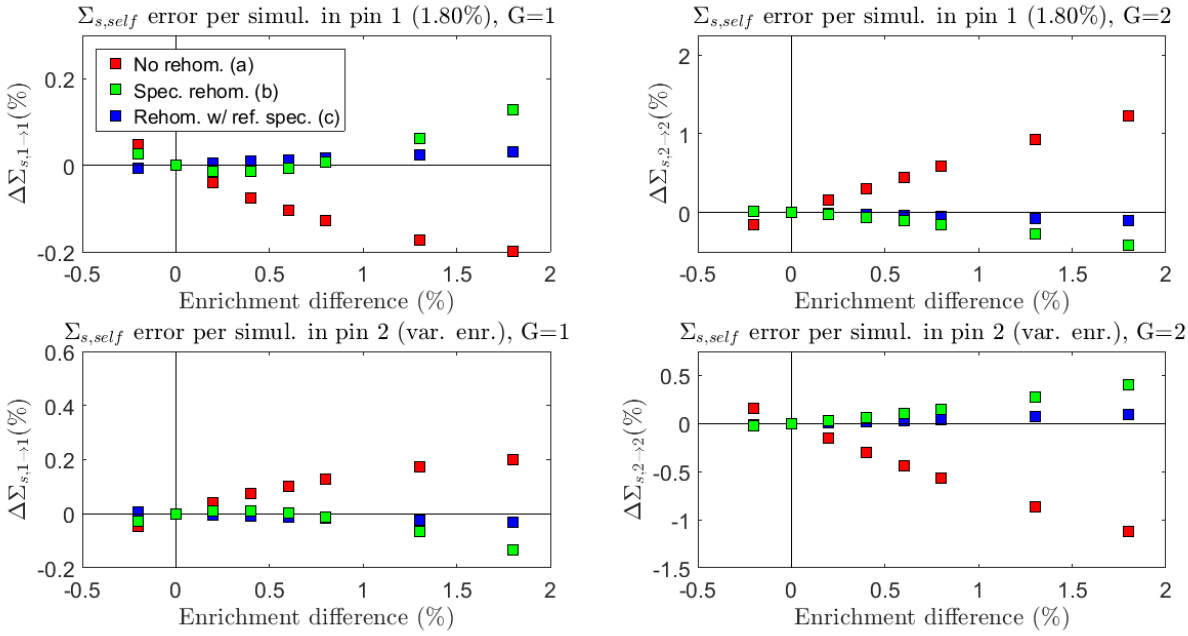

Figure 4.11: Self-scattering cross section errors for the varying enrichment pin checkerboard, per pin type, per group, for each simulation, plotted against the enrichment difference.

Flux distribution errors are plotted in Figure 4.13. The magnitude of fast group flux errors is a few times larger than that of thermal group ones. Moreover, it is found that the spectral index, that is:

$$SI^k = \frac{\bar{\phi}^k_{(G=1)}}{\bar{\phi}^k_{(G=2)}} \tag{4.2}$$

is consistently underestimated when using infinite-medium cross sections without rehomogenization. Fast group flux errors are barely affected by the use of reference environmental cross sections (d) or approximations to these (b-c). Thermal flux errors are reduced to a larger extent, most notably in the pins with higher enrichment, although a small overcorrection is introduced. Since thermal group reactions dominate overall reactor behaviour, it can be expected, with both thermal cross section errors and thermal flux errors being reduced, that overall reaction rate errors other than fission are reduced through rehomogenization as well.

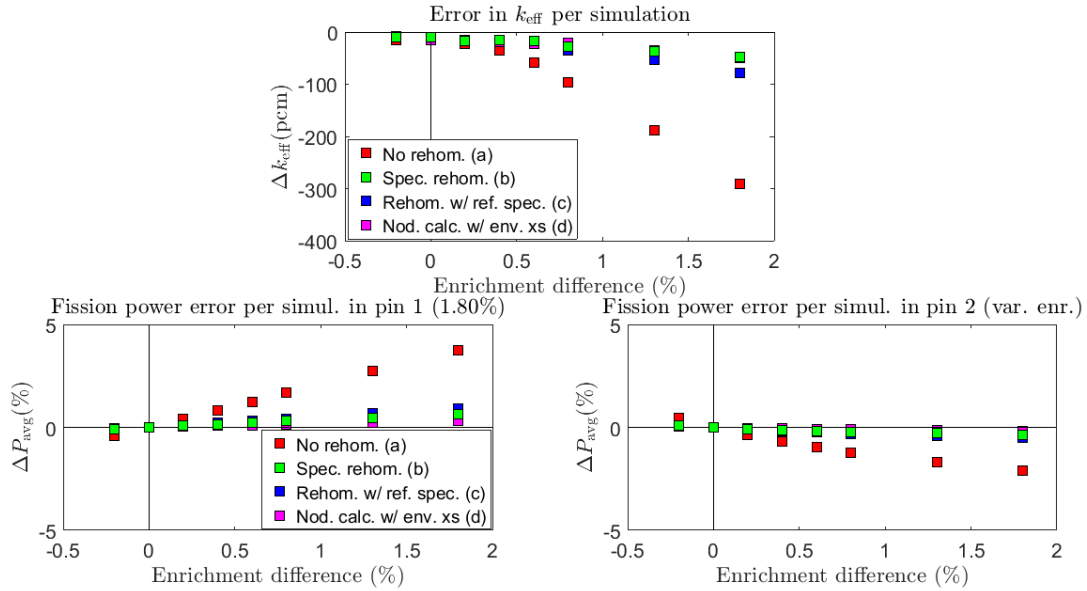

Figure 4.12: Errors on integral parameters for the varying enrichment pin checkerboard, per pin type, per group, for each simulation, plotted against the enrichment difference.

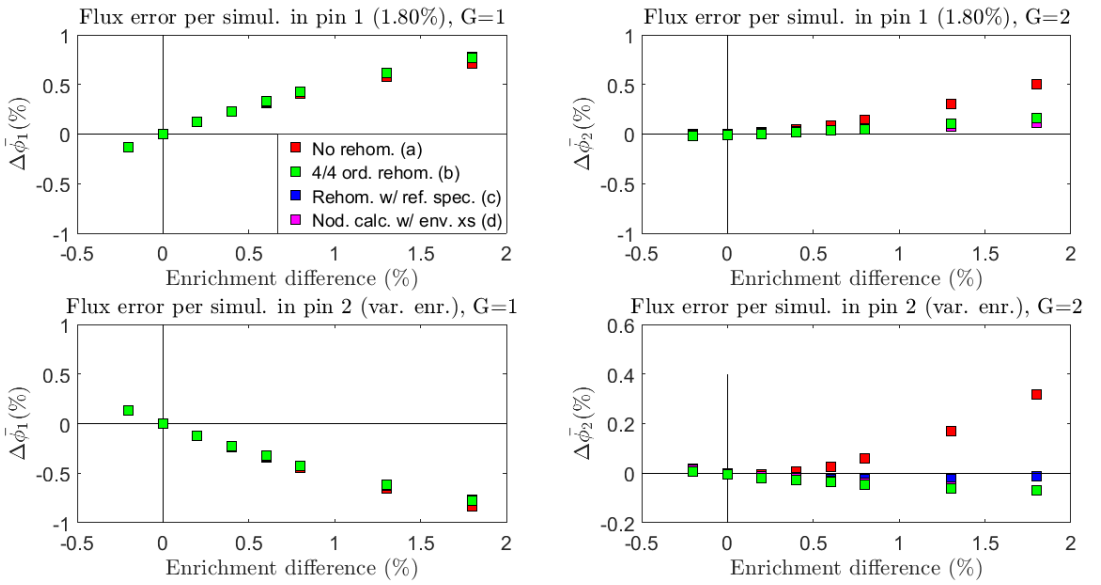

Figure 4.13: Flux distribution errors for the varying enrichment pin checkerboard, per pin type, per group, for each simulation, plotted against the enrichment difference.

4.3.2 Spectrum variation reconstruction

We are interested in what is causing the increase in fast group total and absorption cross section errors with rehomogenization at large enrichment difference. To this end we investigate to what level of accuracy the spectrum variation is reconstructed for various cases, as well as the fine-group total and absorption cross section lethargy shapes.

In Figures 4.14 and 4.15 the spectrum variation reconstructions are plotted for the 1.80 % / 2.00 % and the 1.80 % / 3.60 % checkerboards respectively. In both cases the thermal group spectrum variation is adequately reconstructed. In the 1.80 % / 2.00 % the spectrum variation reconstruction is performed well in the epithermal region, but less so in the fission emission region. The converse is true for the 1.80 % / 3.60 % case. Absorption cross section behaviour, as shown in Figure 4.16, is predominantly determined in the epithermal region. The effective region is more extensive in case of the total cross section, as shown in Figure 4.17, but the cross section magnitude also declines near the fission emission region. This suggests that an adequate reconstruction in the fission emission spectrum is of limited influence on the error reduction in the cross sections. This partly explains why rehomogenization in the 1.80 % / 2.00 % case gives better results compared to the reference spectrum corrections, than the 1.80 % / 2.00 % does, although one should also consider the overall vastly smaller magnitude of the spectrum variation.

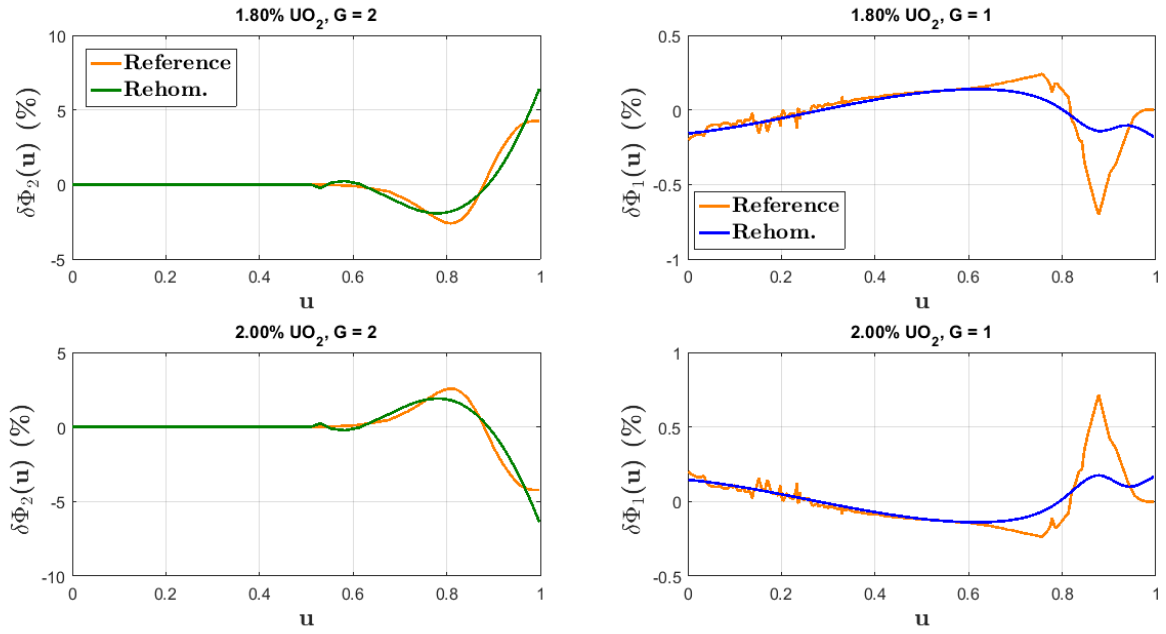

Figure 4.14: Reference flux spectrum variation and reconstruction for the 1.80 % / 2.00 % UO_2 pin checkerboard following 4th order rehomogenization.

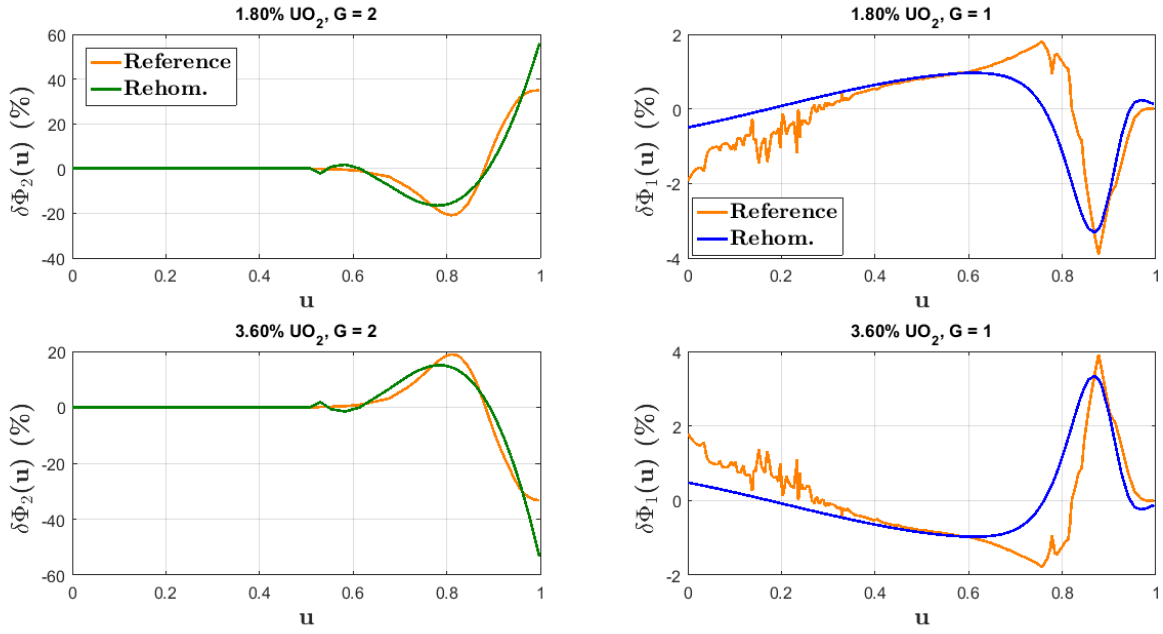

Figure 4.15: Reference flux spectrum variation and reconstruction for the 1.80 % / 3.60 % UO_2 pin checkerboard following 4th order rehomogenization.

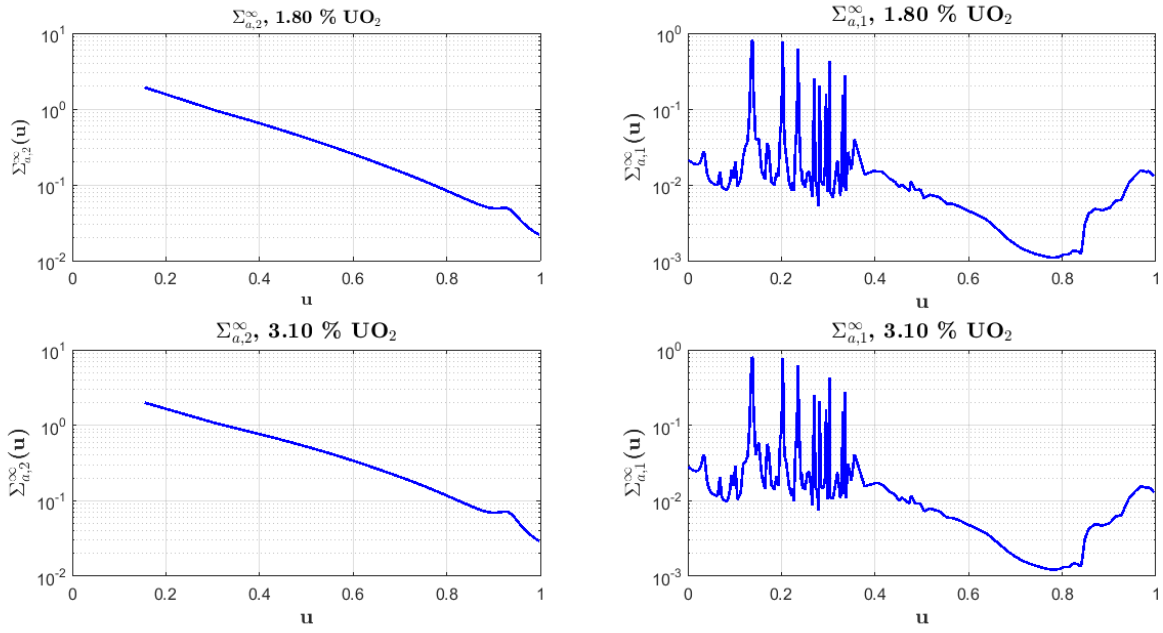

Figure 4.16: Absorption cross section lethargy distribution, per group, of the 1.80 % UO_2 cell.

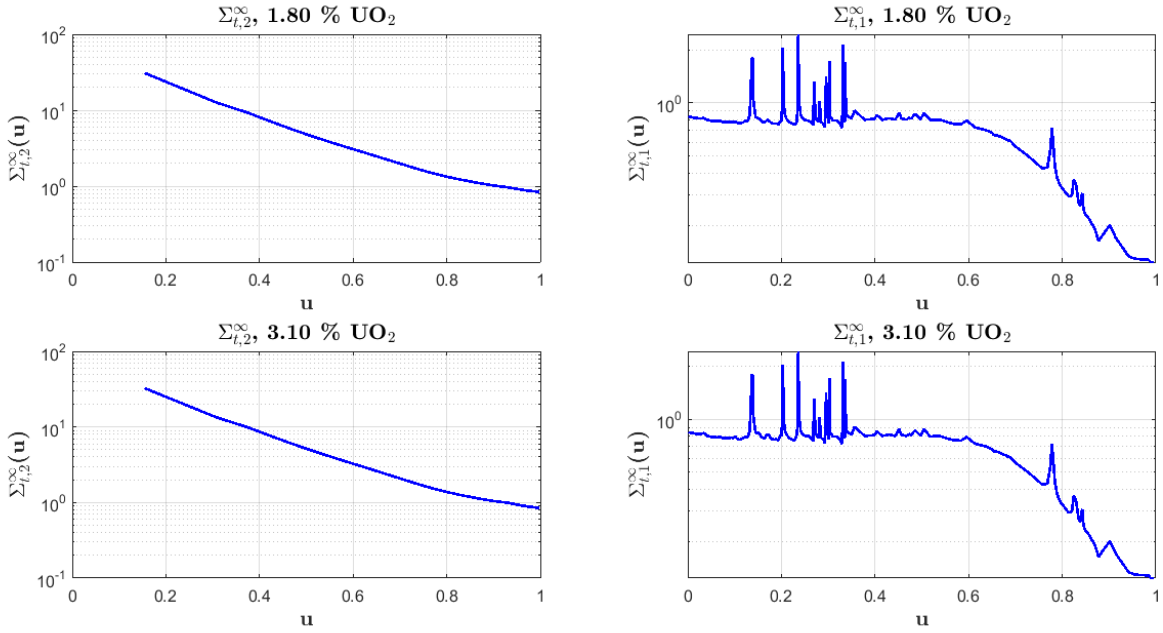

Figure 4.17: Total cross section lethargy distribution, per group, of the 1.80 % UO_2 cell.

We try to achieve a better spectrum variation reconstruction by increasing the expansion order in the fast group to 8. Now focussing only on the total and absorption cross section errors, the results are presented in Figures 4.18 and 4.19.

The expansion order increase does not lead to an improvement of the cross sections. The fast group even sees a slight deterioration. We observe, from the spectrum variation reconstruction, displayed in Figure 4.20, that the accuracy of the reconstruction in the fast group has not improved in the epithermal region. Instead the rehomogenization curve oscillates around an absolute value underestimation of the reference spectrum variation, while the peak values in the fission emission spectrum nearly coincide.

Finally we consider the best fit of the reference spectrum variation to the 4^{th} order expansion, which is shown in Figure 4.21.

The total and absorption cross section errors following this theoretical spectrum variation reconstruction are substantially improved, as seen in Table 4.11. It leads us to conclude that, even though we observed a substantial overall improvement, better results can be achieved if the spectrum variation reconstruction is enhanced in the resonance region, for instance by a choice of trial functions that adds more weight to this region.

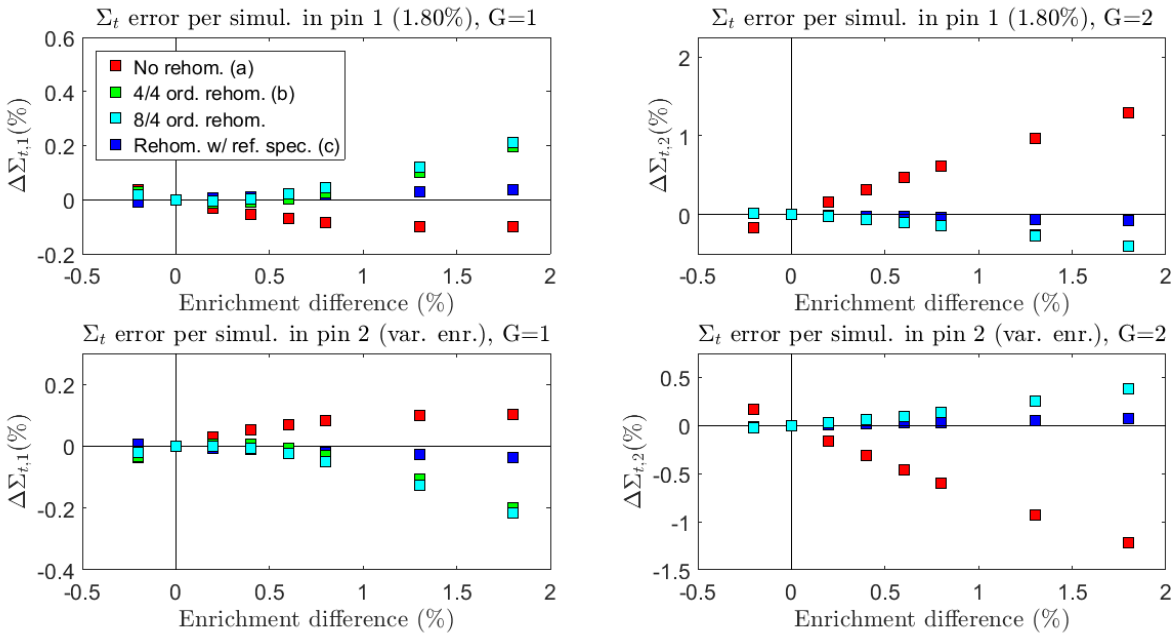

Figure 4.18: Total cross section errors for the varying enrichment pin checkerboard, per pin type, per group, for each simulation, including fast group-8th order rehomogenization.

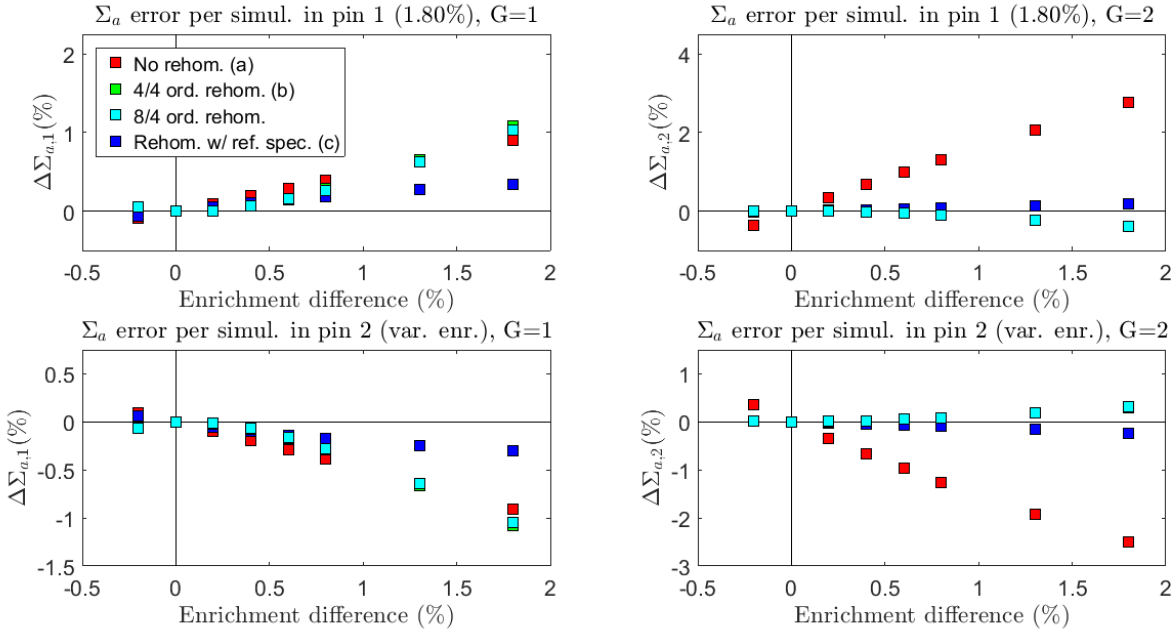

Figure 4.19: Absorption cross section errors for the varying enrichment pin checkerboard, per pin type, per group, for each simulation, including fast group-8th order rehomogenization.

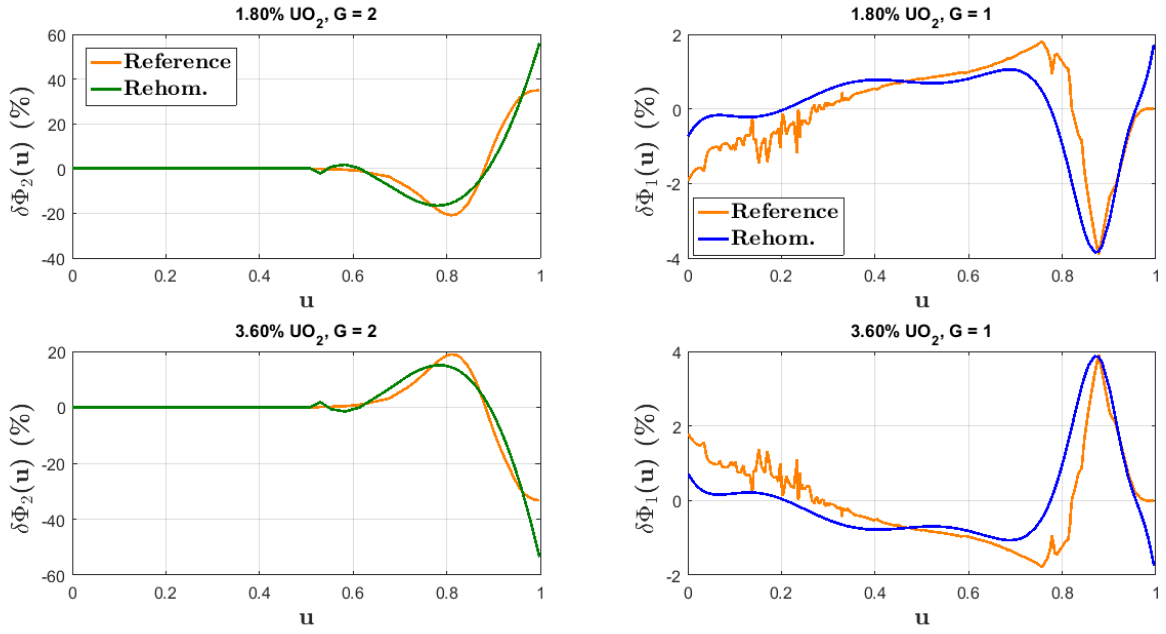

Figure 4.20: Reference flux spectrum variation for the varying enrichment pin checkerboard and reconstruction following rehomogenization of 4th order in the thermal group and 8th order in the fast group.

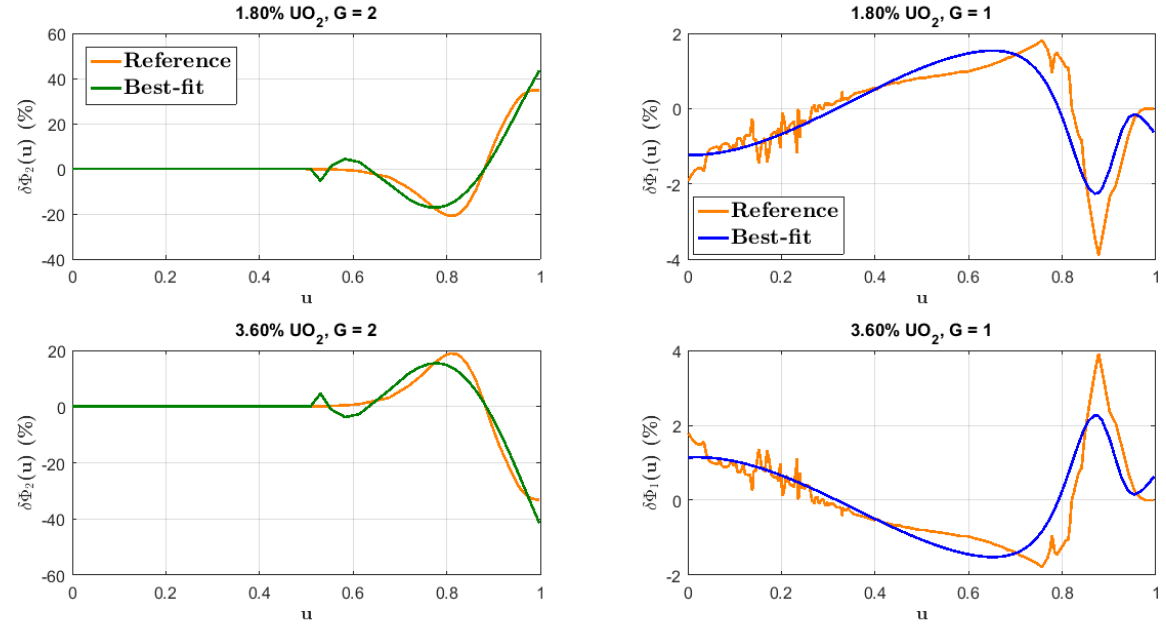

Figure 4.21: Reference flux spectrum variation for the varying enrichment pin checkerboard and least-squares fit of 4th order expansion.

Table 4.11: Total and absorption cross section errors, per group, per pin type, for different simulations, including a spectral cross section correction following the least squares fit of the reference spectrum variation.

	Pin 1 (1.80 %)				Pin 2 (3.60 %)			
Simulation	$\Sigma_{t,1}$	$\Sigma_{t,2}$	$\Sigma_{a,1}$	$\Sigma_{a,2}$	$\Sigma_{t,1}$	$\Sigma_{t,2}$	$\Sigma_{a,1}$	$\Sigma_{a,2}$
No rehom. (a)	-0.1014	1.294	0.9021	2.768	0.1015	-1.217	-0.9128	-2.498
Rehom 4/4 ord. (b)	0.1948	-0.3989	1.079	-0.3884	-0.1992	0.383	-1.084	0.3018
Best fit corr.	0.03737	-0.2296	-0.04696	-0.04815	-0.03842	0.2046	-0.0005057	-0.03407
Ref. spec. corr. (c)	0.03512	-0.08077	0.3453	0.1736	-0.03535	0.07031	-0.3035	-0.2321

4.3.3 Transport effect

Since the rehomogenization problem is dependent on the solution of the nodal diffusion calculation, we are interested in how the diffusion approximation contributes to the errors in the flux distribution and multiplication factor with increasing heterogeneity. For this purpose a set of S_6 transport calculations is conducted on the checkerboards using homogenized cross sections from the infinite medium heterogeneous calculations. The results, computed using the SCALE NEWT algorithm in a meshing scheme of 2×2 nodes per pin, are compared with those of the nodal diffusion calculations employing infinite-medium cross sections (a). The results are displayed in Figures 4.22 and 4.23.

It is found that, with regard to the results obtained with environmental cross sections in subsection 4.3.1, the difference between transport and diffusion is of limited effect to the multiplication factor.

To the flux errors, the diffusion approximation is however of substantial importance. This is clearly visible in the fast group, when comparing Figures 4.12 and 4.23 The difference can be explained by the limited validity of diffusion theory in sub-mean free path meshing. These deviations may play a role in the limited rehomogenization performance in the fast group.

Errors in the thermal group flux show less symmetric behaviour. Errors on the transport and diffusion calculations grow in different directions with increasing heterogeneity in the 1.80 % pin, whereas in the pin with varying enrichment, the thermal flux errors exceed those from the nodal diffusion calculation. It is difficult to point out a specific cause to these effects, though one possible explanation could be that both the nodal diffusion calculation, through the diffusion approximation, and the S_6 calculation, through lack of a nodal expansion, are incapable of reconstructing flux gradients associated with the strong absorbing behaviour of the fuel rods, especially as enrichments become larger.

The use of environmental cross sections, however, substantially reduces the thermal group flux errors, as seen in 4.12, and this seems only to limited extent related to the transport effect.

It should be noted that no nodal expansion has been applied in the S_6 calculations, adding a source of inconsistency to this comparison.

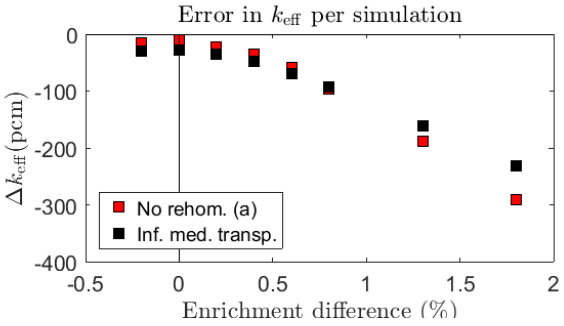

Figure 4.22: Multiplication factor error for the varying enrichment pin checkerboard, per pin type, per group, plotted against the enrichment difference for nodal diffusion calculation (a) and a transport calculation with infinite-medium homogenized cells.

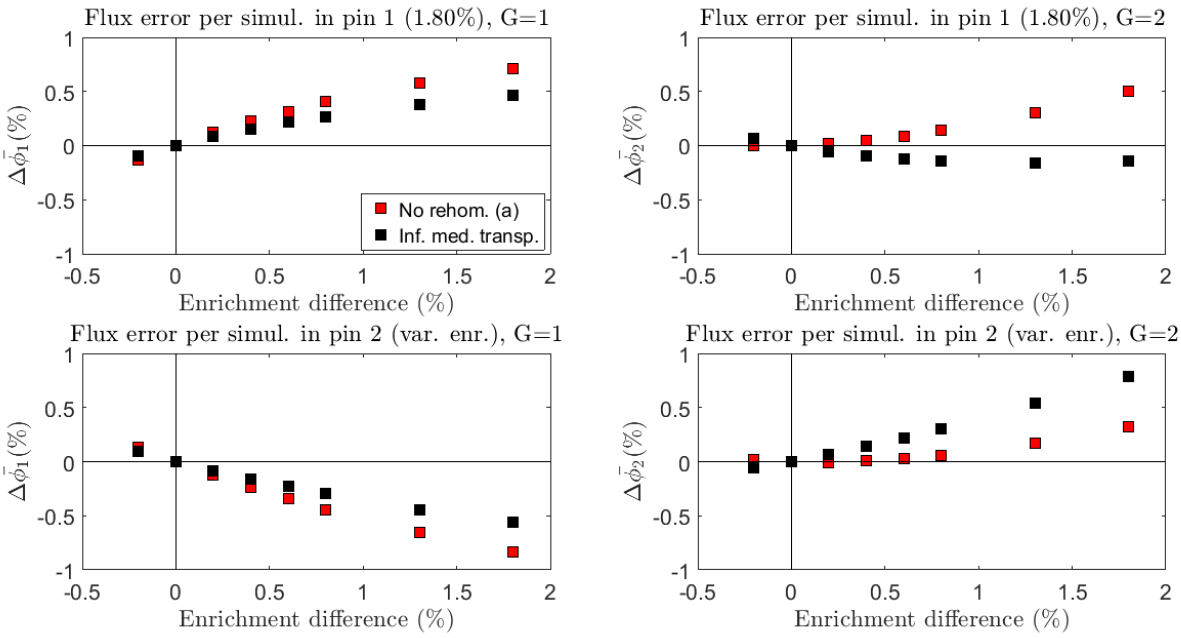

Figure 4.23: Flux errors for the varying enrichment pin checkerboard, per pin type, per group, plotted against the enrichment difference for nodal diffusion calculation (a) and a transport calculation with infinite-medium homogenized cells.

4.3.4 Summary

A parametric study on the influence of the heterogeneity on the rehomogenization performance has shown an overall cross section error reduction in the thermal group following rehomogenization, as well as on the resulting fluxes, pin powers and multiplication factor. These error reductions are generally not achieved in the fast group, mostly due to inability to reconstruct the spectrum variation especially in the epithermal region. Part of the overall inaccuracies in the fast group cross sections may be attributed to the errors introduced by the diffusion approximation.

4.4 Application to the (UOX + Gd) colorset

We move on from the pin checkerboard configuration to study the effect of spectral rehomogenization in assembly colorsets, configurations that are more representative of an actual PWR environment. We consider a colorset of a (17×17) UOX assembly with 1.8 % enrichment neighbouring a 3.9 % enriched UOX assembly that is loaded with 12 burnable absorber rods containing depleted uranium (0.25 %) and 7.65 wt% GdO. The colorset layout is shown in Figure 4.24. Detailed descriptions of the assemblies making up the colorset are given in Appendix B.2. It should be noted that grid spacers and water gaps, separating pins and assemblies respectively, are disregarded for the purpose of this study. The calculation results are displayed in Table 4.12, in terms of multiplication factor error, power distribution and cross section errors in an extreme value sense as well as in a root mean square sense.

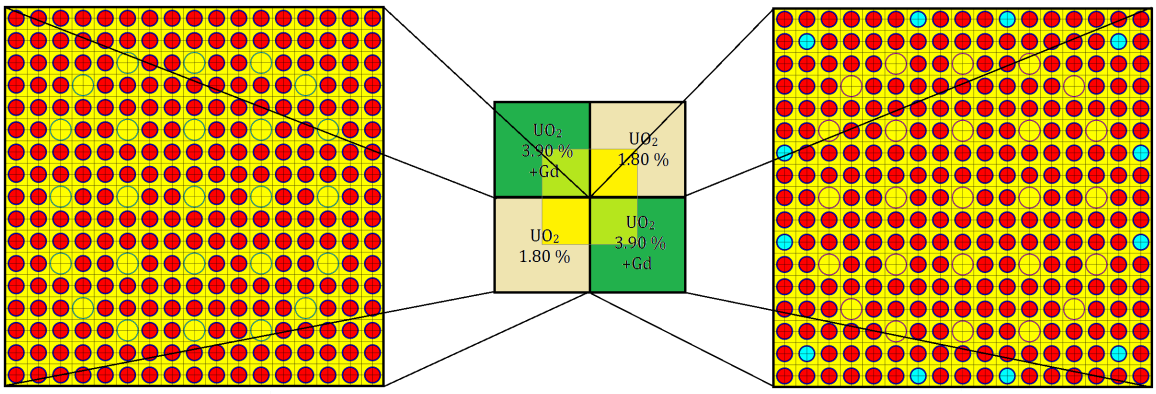

Figure 4.24: Schematic layout of the (UOX + Gd) colorset with assembly layouts. The cyan colored cylinders represent the Gd-loaded rods.

Table 4.12: Comparison of errors on multiplication factor (k_{eff}) and pin power distribution errors per assembly and for the full colorset (a), total and absorption cross section per group (b), fission neutron production and fission cross section (c) and out-scatter and self-scatter cross section errors (d), in an extreme value (max/min) and a root mean square (rms) sense.

		ΔP (ass. 1) (%)		ΔP (ass. 2) (%)		ΔP_{avg} (%)	
Simulation	Δk_{eff} (pcm)	max/min	rms	max/min	rms	max/min	rms
No rehom. (a)	262.53	-4.949	2.648	-3.647	2.752	-4.949	2.7
Spec. rehom (b)	-551.34	-4.973	2.462	-3.524	1.627	-4.973	2.087
Ref. spec. corr. (c)	-548.42	-3.398	1.035	-3.415	1.917	-3.415	1.54
Nodal calc. w/ env. xs. (d)	-796.24	-1.687	0.4732	-2.536	1.383	-2.536	1.034

(a)

	$\Delta\Sigma_{t,1}$ (%)		$\Delta\Sigma_{t,2}$ (%)		$\Delta\Sigma_{a,1}$ (%)		$\Delta\Sigma_{a,2}$ (%)	
Simulation	max/min	rms	max/min	rms	max/min	rms	max/min	rms
No rehom. (a)	-1.743	0.8282	-18.76	2.711	-9.633	2.422	-29.8	4.368
Spec. rehom (b)	1.811	0.7725	-1.832	0.5483	-5.537	2.113	-7.889	1.366
Ref. spec. corr. (c)	-0.06731	0.02342	-2.337	0.4676	-0.5678	0.2373	-8.758	1.371

(b)

	$\Delta\nu\Sigma_{f,1}$ (%)		$\Delta\nu\Sigma_{f,2}$ (%)		$\Delta\Sigma_{f,1}$ (%)		$\Delta\Sigma_{f,2}$ (%)	
Simulation	max/min	rms	max/min	rms	max/min	rms	max/min	rms
No rehom. (a)	-3.196	1.5	-3.991	3.55	-3.154	1.454	-3.991	3.55
Spec. rehom (b)	-3.06	1.297	-4.401	1.245	-3.017	1.281	-4.4	1.245
Ref. spec. corr. (c)	-0.9537	0.7204	-5.75	1.37	-0.8762	0.6826	-5.749	1.37

(c)

	$\Delta\Sigma_{s,1\to2}$ (%)		$\Delta\Sigma_{s,2\to1}$ (%)		$\Delta\Sigma_{s,1\to1}$ (%)		$\Delta\Sigma_{s,2\to2}$ (%)	
Simulation	max/min	rms	max/min	rms	max/min	rms	max/min	rms
No rehom. (a)	-18.73	3.789	-20.78	19.83	-1.528	0.8323	-14.3	2.145
Spec. rehom (b)	-5.796	2.922	-37.54	7.589	1.732	0.7365	-1.365	0.6181
Ref. spec. corr. (c)	-0.2585	0.09343	-0.06046	0.02587	-0.05705	0.02146	-1.215	0.4476

(d)

We observe a slight error reduction for the assembly power in the UOX assembly due to rehomogenization, whereas the error reduction in the UGd assembly is more pronounced. Rehomogenization

leads to a slight overcorrection in the power in the latter, compared to the reference spectrum correction. Overall still a power distribution error of about 1 % (rms) may be attributed to the diffusion approximation and the spatial and spectral discretizations. Approximation of the reference environmental cross sections leads to an unexpectedly steep deterioration in the multiplication factor. The cause of this effect is unclear.

Thermal group cross sections overall sharply improve following a reference spectrum correction, and do so after rehomogenization as well (albeit to limited extent). As is the case in the pin checkerboard configurations discussed previously, the improvement is generally less pronounced in the fast group, and it may be a result of the limited spectrum reconstruction capability in this group that was also observed previously. It is worth mentioning that the extreme error magnitudes in the thermal total and absorption cross sections are sharply reduced as well.

To better understand the origin of these error reductions, we consider the power and cross section error distributions in more detail. Firstly, in Figure 4.25, the reference power distribution is plotted in units that have been normalized such that the total flux integrated over both energy and space equals unity. The power production in the 3.90 % UO_2 pins is understandibly higher than that in the 1.80 % pins. No power is produced in the water rods and very little in the burnable absorbers, due to both their low fissile content and self-shielding effects.

The percentual deviation from this power distribution is shown per simulation in Figure 4.26. All errors are plotted to the same scale along the color axis. The reference spectrum correction leads to a near-complete error eradication near the center of the UOX assembly, but leaves larger errors in the UGd assembly. However, the larger part of these power distribution errors persist even when reference cross sections are used, albeit to a lesser extent. It is understood that this inaccuracy must be a consequence of a flux overestimation in the Gd rods associated with the diffusion approximation. Spectral rehomogenization is capable of correcting the fission power overestimation in the vicinity of the assembly interface, as well as in the fuel cells neighbouring the Gd-loaded pins, thereby partly adressing the infinite medium inaccuracies stated by Tatsumi et al. [19]. While capable of slightly reducing the fission power error in the UOX assembly, the extent of this error reduction is limited. In the UGd assembly power errors are overcorrected. This is consistent with our observations from Table 4.12.

We are interested in what may be causing the limited power accuracy in the UOX assembly after rehomogenization. For this purpose we investigate the error distribution on the group fission neutron production cross sections (which are assumed not to deviate substantially from the actual fission cross section errors), depicted in Figure 4.27. The thermal fission neutron production error distribution following rehomogenization largely follows that of the reference spectrum correction, leading to the near elimination of errors close to the center-assemblies and an overcorrection to the fission neutron production cross section in the Gd absorber rods. The latter is of limited consequence to the total power production, as the reference fission rate in the Gd rods is very low compared to that in the (enriched) UO_2 cells. Following rehomogenization, fission neutron production in the fast group is subject to persistent underestimation near the UOX center-assembly and overestimation in the Gd rods. The former error is largely resolved by the reference spectrum correction. While this follows the pattern observed in the fission power error distribution, fission in the fast group only accounts for approximately one fifth of the total power. Further sources of error in the power distribution must be sought for in the thermal group. Since fission cross section errors are largely eliminated in the thermal group, the thermal fission rate error must be largely caused by deviation from the reference flux distribution.

Errors on the flux distributions are displayed in Figure 4.28. The flux overestimation in the UO_2 rods neighbouring the Gd-loaded rods is vastly reduced, as is consistent with the pin power error distribution. Moreover, as expected, the large thermal flux underestimation in the non-corrected calculation (a) vanishes after reference spectrum correction (c), but persists after rehomogenization (b). The thermal flux distributions could partly explain the behaviour of k_{eff} observed in Table 4.12. In (a) vast flux overestimations occur in the 3.90 % UO_2 cells close to the Gd rods, leading to fission rate overestimations that counter the fission rate underestimations in the UOX assembly, as well as the absorption rate overestimation in the Gd rods. The fission rate overestimation is reduced after spectral correction (b-c), to nearly vanish in the case of reference environmental cross sections (d).

At the same time absorption rate overestimation persists in the Gd rods as well as a slight fission rate underestimation at the UGd assembly centers. The large persistent errors in the Gd rods can be attributed to the diffusion equation, which is known for reduced performance in strong absorbers.

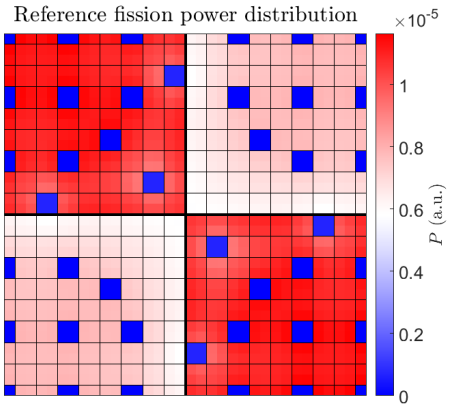

Figure 4.25: Reference fission power distribution in the (UOX + Gd) colorset in normalized units.

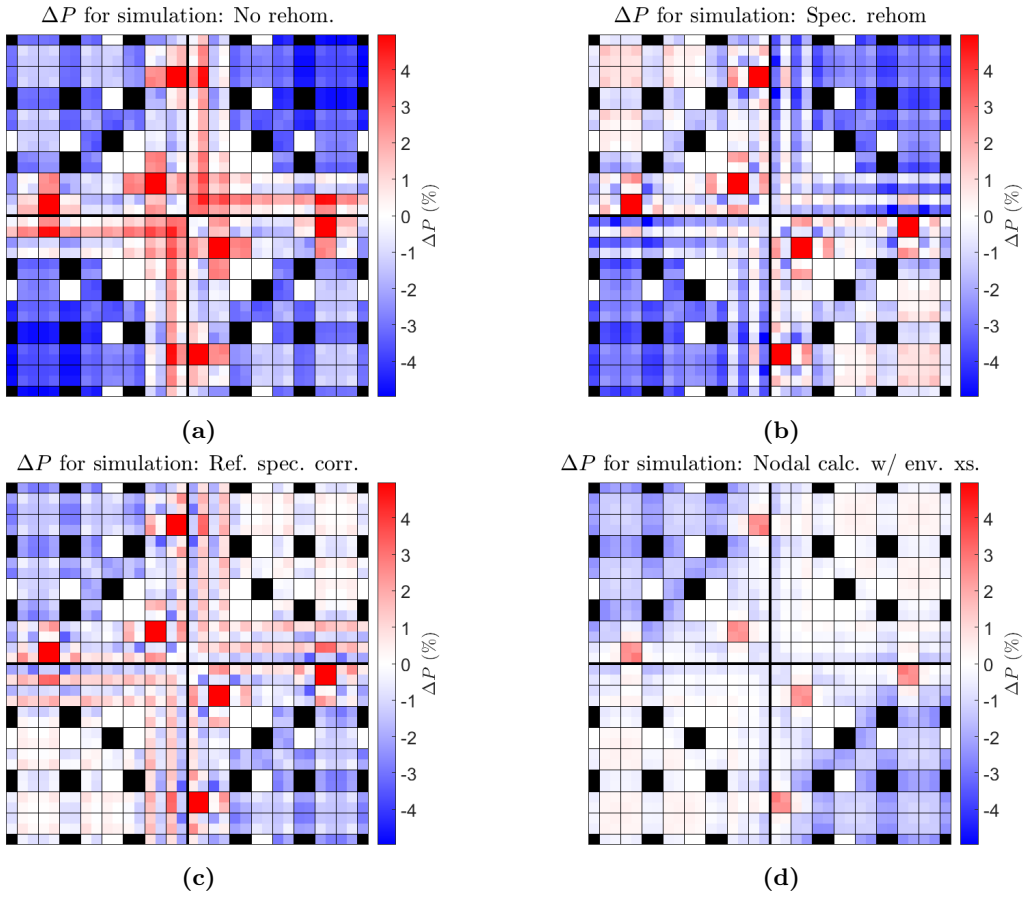

Figure 4.26: Deviations from the reference power distribution for the standard pin-by-pin nodal calculation (a), nodal calculation with spectral rehomogenization (b), nodal calculation with reference spectrum-corrected cross sections (c) and reference environmental cross sections(d).

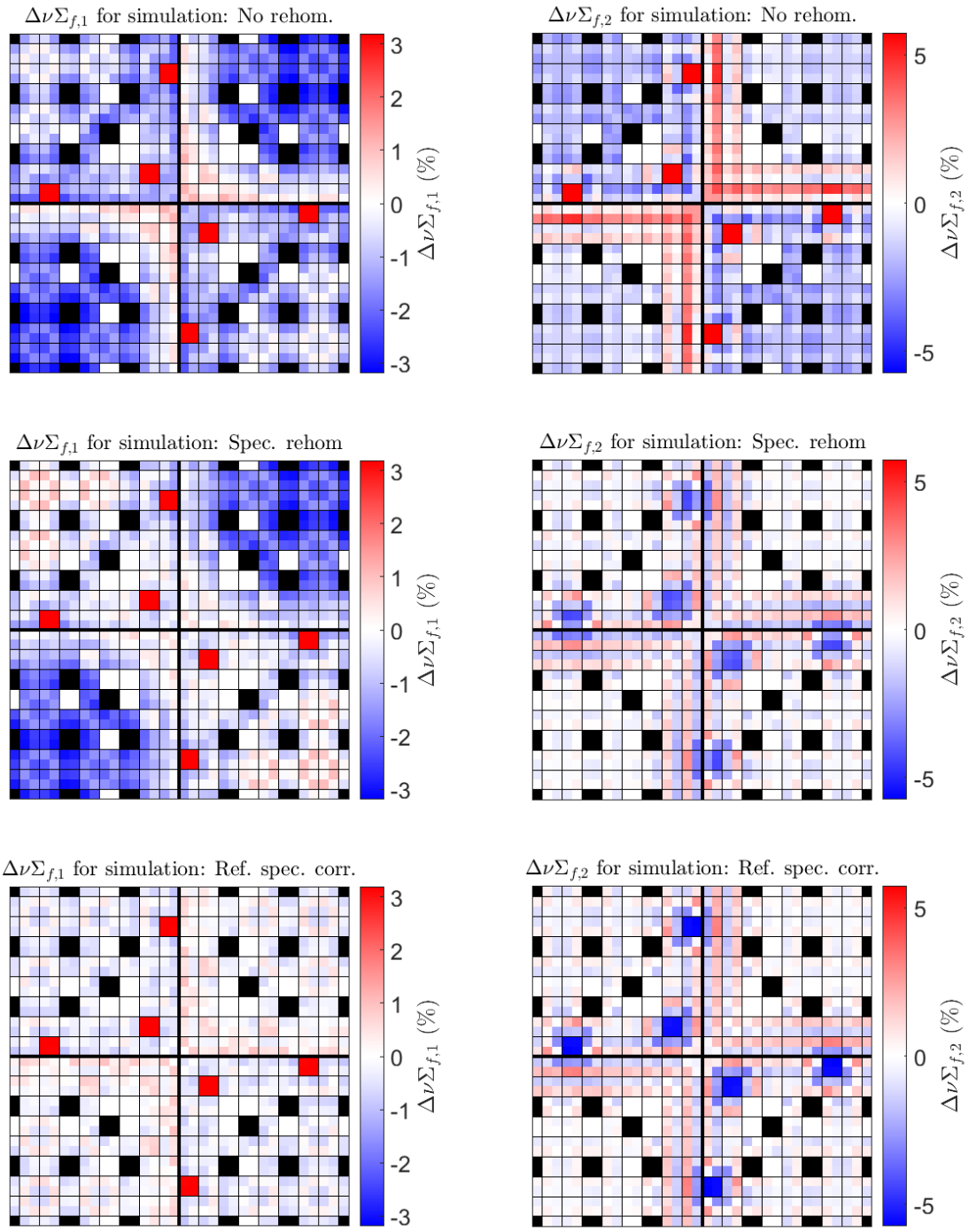

Figure 4.27: Fission neutron production cross section error distributions for the standard pin-by-pin nodal simulation (top), nodal calculation with spectral rehomogenization (middle) and reference spectrum correction (bottom), for the fast (left) and thermal (right) energy groups.

The main reactions governing the thermal flux distribution are down-scattering of fast neutrons and thermal absorption. In Figure 4.29 we consider the cross section error distributions associated with these reactions. The extreme values of the thermal absorption cross section error, mentioned in the discussion of the overall overview (Table 4.12), coincide with the Gd loaded rods. There are few other pronounced errors in the thermal group absorption cross section, apart from a slight overestimation near the assembly interface in the UOX assembly, and even less so after rehomogenization, although rehomogenization does introduce a slight absorption cross section overestimation in the UGd

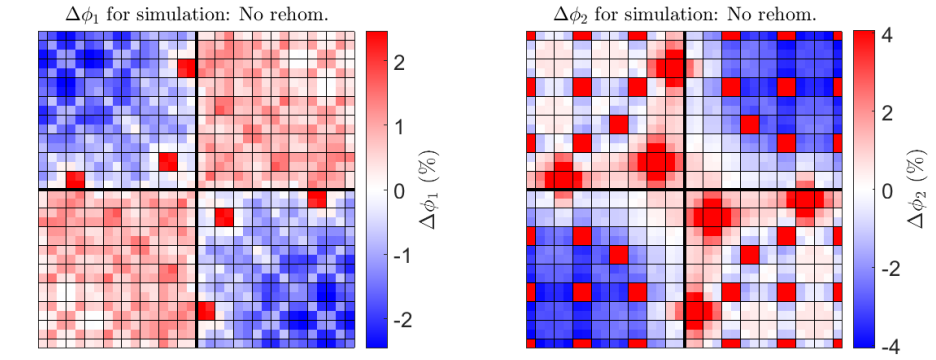

(a)

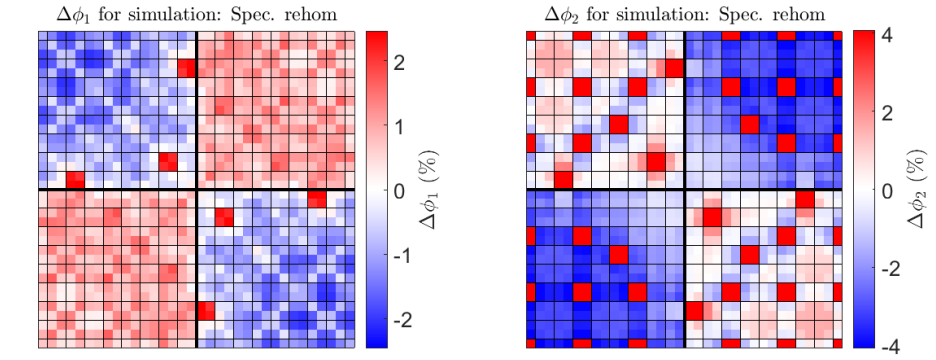

(b)

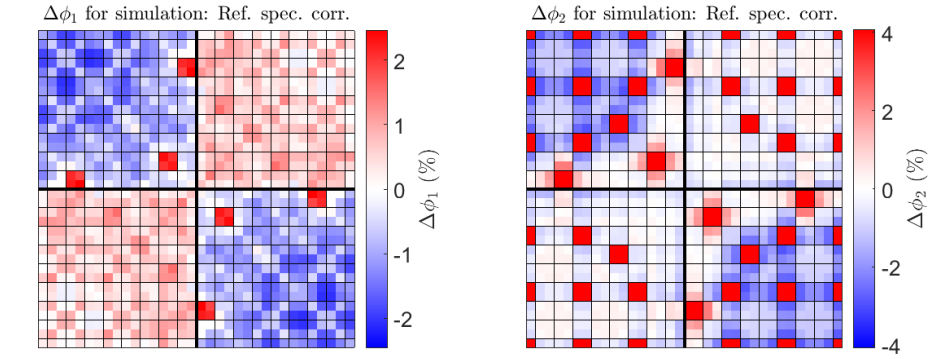

(c)

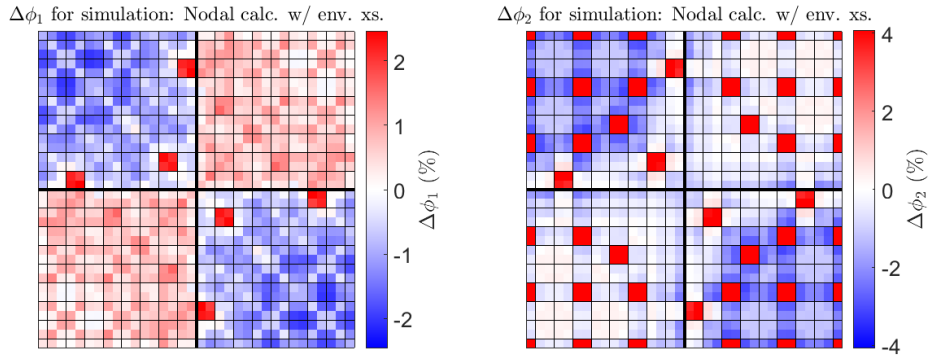

(d)

Figure 4.28: Flux error distributions for the standard pin-by-pin nodal simulation (a), nodal calculation with spectral rehomogenization (b), reference spectrum correction (c) and nodal simulation with reference environmental cross sections (d) for the fast (left) and thermal (right) energy groups.

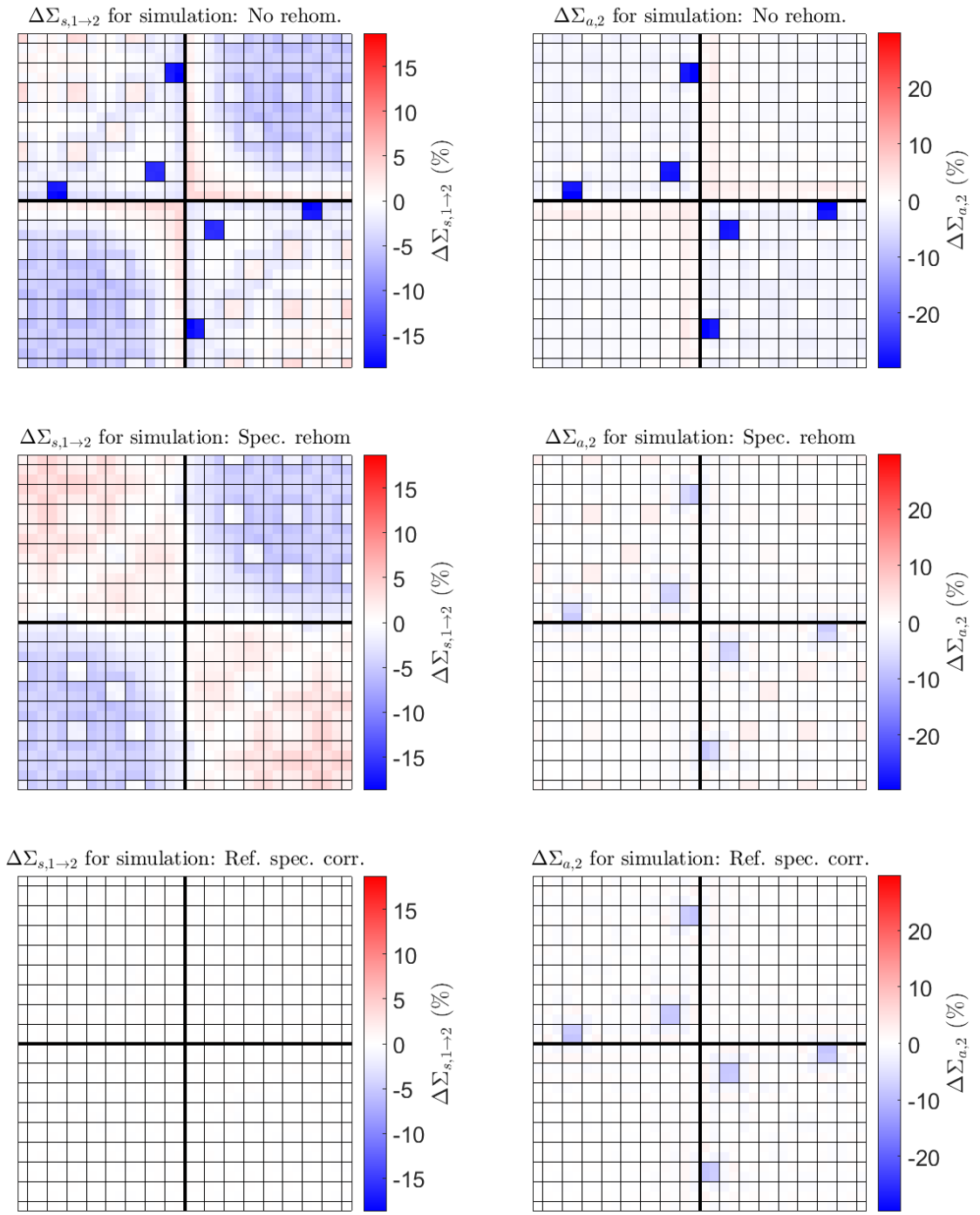

Figure 4.29: Fast group out-scatter (left) and thermal group absorption (right) cross section error distributions for the standard pin-by-pin nodal simulation (top), nodal calculation with spectral rehomogenization (middle) and reference spectrum correction (bottom).

assembly water channels. Looking at the down-scattering cross section errors from the fast group, we can identify both the underestimation near the UOX center-assembly that persists after rehomogenization, as well as the overcorrection on the UO_2 rods near the UGd center-assembly. Both these errors vanish in the case of the reference spectrum correction. It is suggested that this is the leading cause for the limited capability to reproduce the fission power distribution.

Seeing that the down-scattering cross section in the fast group falls of with increasing energy

(Figure 4.30), we conclude that this is consistent with our earlier observation from the pin checkerboard configuration, that the current implementation of the spectral rehomogenization method is insufficiently capable of reconstructing the flux spectrum variation in the epithermal region.

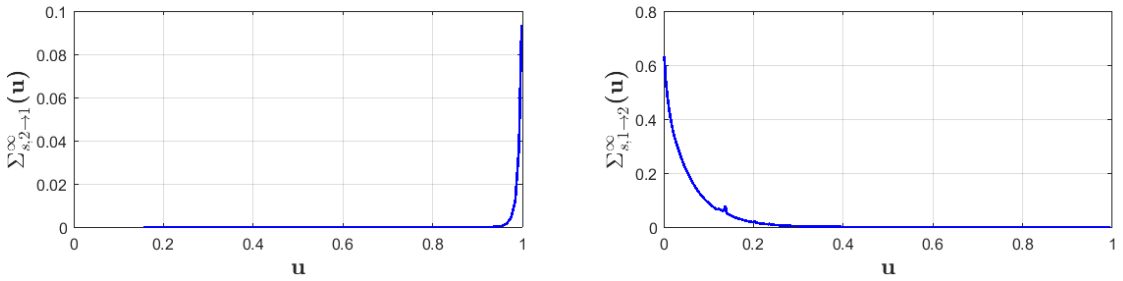

Figure 4.30: Infinite medium out-scatter cross section lethargy distribution for the 1.80 % UO_2 cell.

4.4.1 Summary

Spectral rehomogenization in the (UOX + Gd) colorset has been found to lead to substantial error reductions for thermal group cross sections, and to lesser extent for fast group cross sections as well. Thermal flux and fission power overestimations in fuel cells in the close neighbourhood of Gd rods have also been mitigated by rehomogenization.

Fission power underestimations in the UOX assembly have been attributed to fast fission cross section and thermal flux underestimations, the latter of which themselves have been linked to the limited capability to reduce fast group down-scattering cross section errors. It has been suggested that this is a result of an inaccurate spectrum variation reconstruction in the epithermal region, which is consistent with findings from the checkerboard calculations.

4.5 Application to the (UOX + MOX) colorset

Next we consider the application of rehomogenization to a checkerboard configuration of (18 × 18) UOX and MOX assemblies. The UOX assembly consists of double-clad UO_2 fuel pins with 2.40 % enrichment, whereas the MOX assembly contains 7.77 wt% PuO_2 on the inside, 5.09 wt% on the edges and 3.57 wt% near the vertices. An overview of the colorset is displayed in Figure 4.31. The detailed assembly layouts and material compositions are described in Appendix B.3. Grid spacers and water gaps are again disregarded. A general overview of the resulting extreme value and root mean square errors on cross sections and on pin powers (both integral and per assembly) is given in Table 4.13, as well as errors on the multiplication factor.

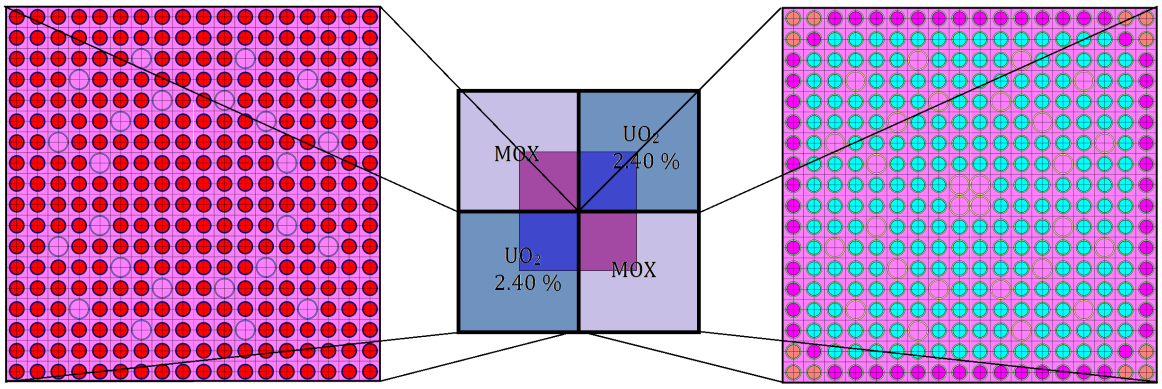

Figure 4.31: Schematic overview of the (UOX + MOX) colorset with assembly layouts. MOX fuel pins located close to the assembly boundary have lower fissile Pu content.

Table 4.13: Comparison of errors on multiplication factor (k_{eff}) and pin power distribution errors per assembly and for the full colorset (a), total and absorption cross section per group (b), fission neutron production and fission cross section (c) and out-scatter and self-scatter cross section errors (d), in an extreme value (max/min) and a root mean square (rms) sense.

		ΔP (ass. 1) (%)		ΔP (ass. 2) (%)		ΔP_{avg} (%)	
Simulation	Δk_{eff} (pcm)	max/min	rms	max/min	rms	max/min	rms
No rehom. (a)	583.86	-6.375	1.946	-3.139	1.465	-6.375	1.722
Spec. rehom (b)	821.05	-10.91	4.087	-4.039	1.892	-10.91	3.184
Ref. spec. corr. (c)	645.47	-8.864	3.028	-3.897	2.366	-8.864	2.717
Nodal calc. w/ env. xs. (d)	652.33	-7.061	2.726	5.329	2.073	-7.061	2.421

(a)

	$\Delta\Sigma_{t,1}$ (%)		$\Delta\Sigma_{t,2}$ (%)		$\Delta\Sigma_{a,1}$ (%)		$\Delta\Sigma_{a,2}$ (%)	
Simulation	max/min	rms	max/min	rms	max/min	rms	max/min	rms
No rehom. (a)	-2.835	0.6491	-3.821	1.411	-9.51	2.997	-5.092	1.992
Spec. rehom (b)	-2.839	0.5247	-7.087	1.473	-8.873	2.574	-12.82	2.725
Ref. spec. corr. (c)	-0.1042	0.02383	-1.136	0.4562	-0.9255	0.3518	-4.734	1.49

(b)

	$\Delta\nu\Sigma_{f,1}$ (%)		$\Delta\nu\Sigma_{f,2}$ (%)		$\Delta\Sigma_{f,1}$ (%)		$\Delta\Sigma_{f,2}$ (%)	
Simulation	max/min	rms	max/min	rms	max/min	rms	max/min	rms
No rehom. (a)	-2.704	0.727	-6.202	2.095	-2.722	0.7738	-6.189	2.091
Spec. rehom (b)	-2.577	0.7478	-4.876	1.71	-2.605	0.8057	-4.863	1.709
Ref. spec. corr. (c)	-0.8199	0.2915	-5.875	1.839	-0.8508	0.3682	-5.863	1.836

(c)

	$\Delta\Sigma_{s,1\to2}$ (%)		$\Delta\Sigma_{s,2\to1}$ (%)		$\Delta\Sigma_{s,1\to1}$ (%)		$\Delta\Sigma_{s,2\to2}$ (%)	
Simulation	max/min	rms	max/min	rms	max/min	rms	max/min	rms
No rehom. (a)	-13.78	5.675	44.38	17.52	-2.388	0.7044	-4.756	1.514
Spec. rehom (b)	-12.85	3.554	65.23	14.92	-2.43	0.4331	-7.082	1.63
Ref. spec. corr. (c)	-0.5594	0.2278	-0.2103	0.08955	-0.06893	0.01627	2.049	0.7461

(d)

While errors seem to deteriorate in many respects following rehomogenization, it should be noted that the extreme value and root mean square pin power errors also deteriorate when reference environmental cross sections are used instead of infinite medium ones. Pin power errors following a calculation with infinite-medium cross sections (a), also shown in Figure 4.33, display numerically small errors, but this appears likely to be caused by a multitude of inaccuracies that coincidentally cancel out to large extent. Nevertheless, following rehomogenization, the RMS power distribution error is of large magnitude, as is the thermal absorption cross section error.

A surprisingly large multiplication factor error exists in all calculations. We may gain a better understanding of this by plotting the power distribution error on a map of the colorset. The reference pin power distribution is plotted in Figure 4.32, with percentual deviations plotted per simulation in Figure 4.33,

The large k_{eff} overestimations are likely caused by the fission power overestimation in the MOX assembly, that cannot be compensated by the underestimation in the UOX assembly due to the latter's vastly lower reference power. The additional overestimation after rehomogenization may be related to a large thermal absorption cross section underestimation located in the MOX assembly, as seen in Table 4.13.

Pin power errors in the non-rehomogenized calculation are generally low. However, the global shape of the error distribution does not correspond to that of the calculation with reference environmental cross sections. This complies with the general notion that infinite medium cross sections show substantial inconsistencies with the environmental ones, possibly leading to larger errors in other reaction rate distributions.

The pin power error distribution shape resulting from calculation (d) is partly restored by rehomogenization, specifically at the UOX assembly vertices.

As at least two thirds of fission power is accounted for by thermal fission, we are interested in

whether the changes in the pin power error distribution following cross section rehomogenization correspond to those in the fission cross section. Again we consider the fission neutron production cross section error distribution in Figure 4.34.

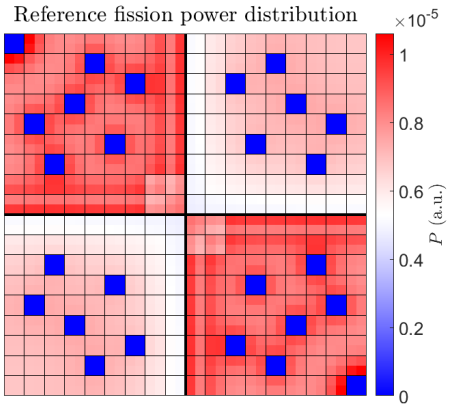

Figure 4.32: Reference fission power distribution in the (UOX + MOX) colorset in normalized units.

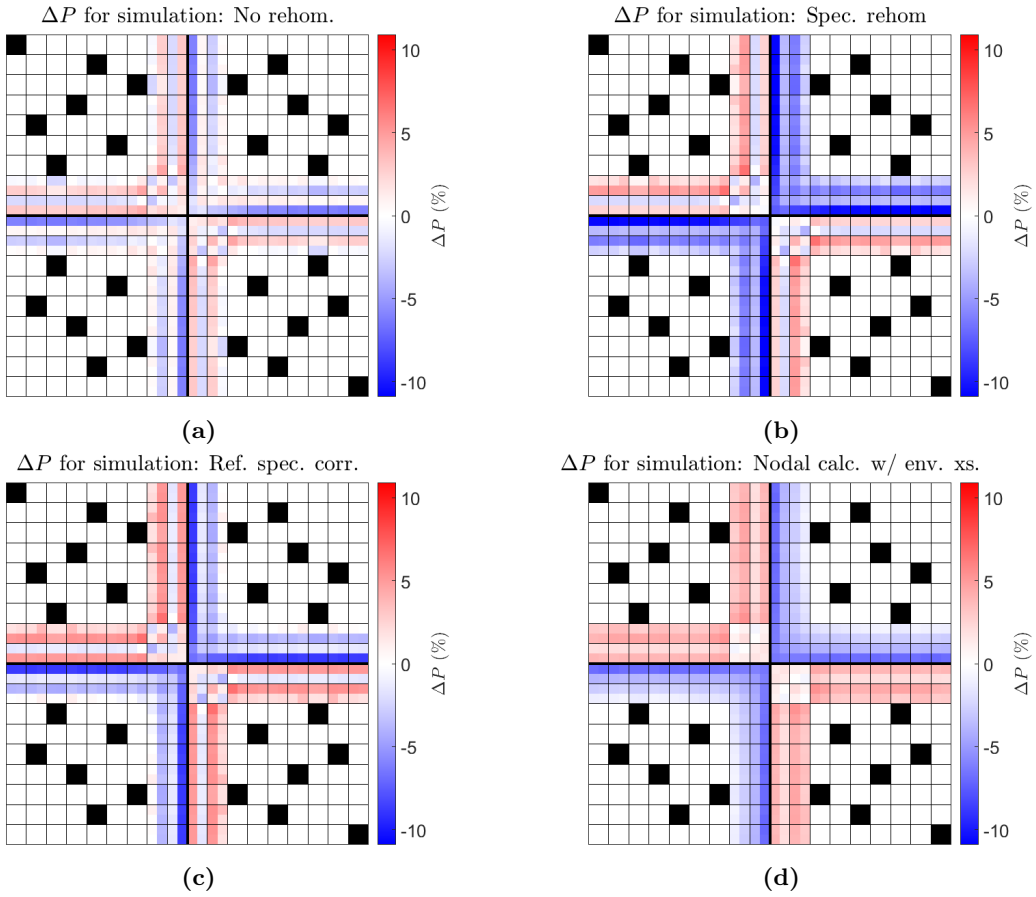

Figure 4.33: Deviations from the reference power distribution for the standard pin-by-pin nodal calculation (a), nodal calculation with spectral rehomogenization (b), nodal calculation with reference spectrum-corrected cross sections (c) and reference environmental cross sections(d).

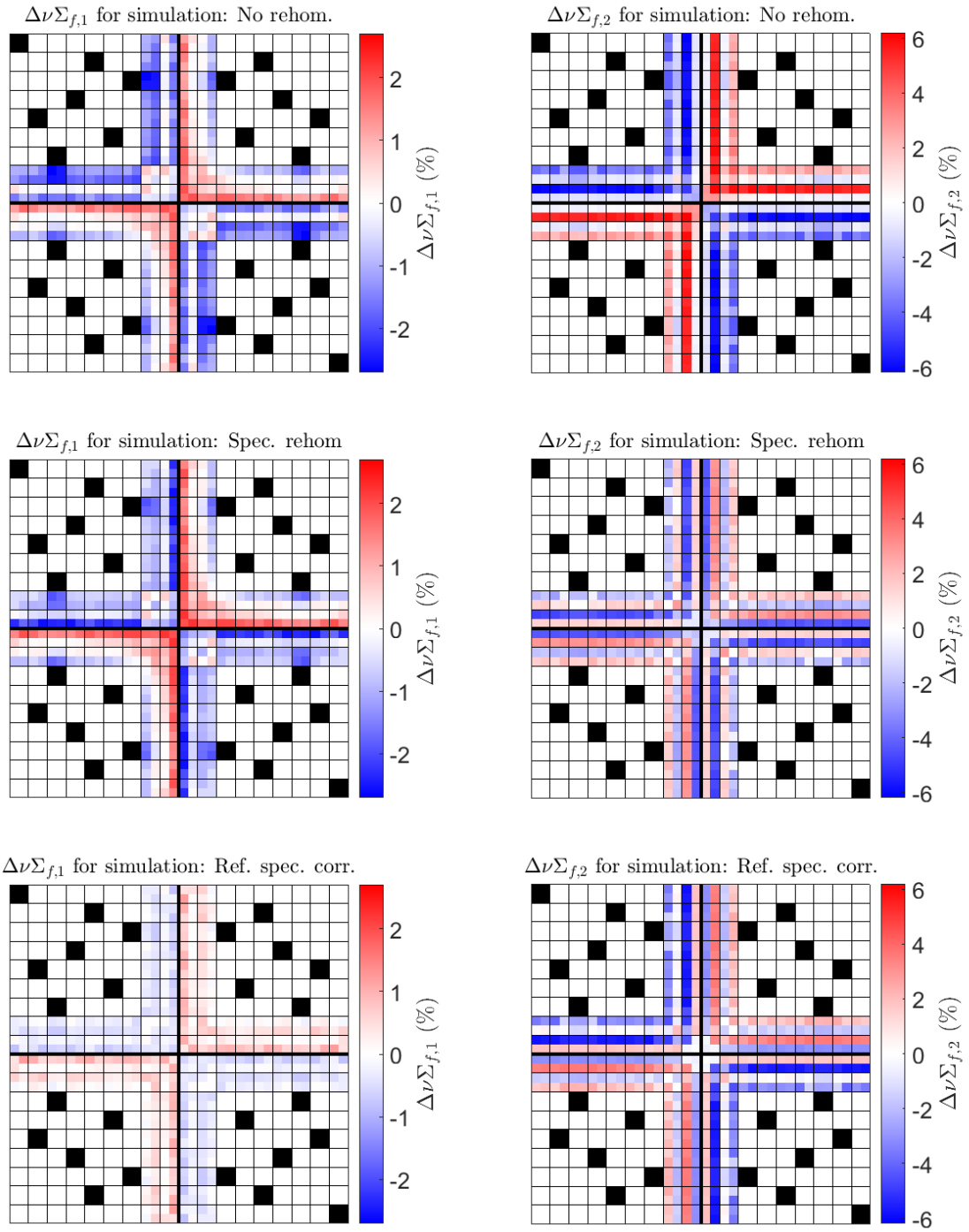

Figure 4.34: Fission neutron production cross section error distributions for the standard pin-by-pin nodal simulation (top), nodal calculation with spectral rehomogenization (middle) and reference spectrum correction (bottom), for the fast (left) and thermal (right) energy groups.

While the thermal group fission neutron production cross section error is somewhat reduced by the reference spectrum correction, especially at the assembly-center-facing nodes of the interface pins, the overall error reduction is not very substantial. This suggests that spatial effects play a larger role at these assembly interfaces than they do for example in the (UOX + Gd) colorset, and possibly also effects related to the cross term in equation 2.38. Introducing spatial corrections may further improve these cross sections, however even with reference environmental cross sections, pin power errors remain substantial as seen previously in Figure 4.33.

Spectral rehomogenization is to large extent able to reproduce the error distribution obtained by the reference spectrum correction in the thermal group, suggesting a good spectrum variation reconstruction. This is also consistent with the result in Table 4.13.

The thermal fission neutron production cross section errors near the UOX assembly vertex shifts from purely positive values to mixed positive and negative values, implying an overall fission rate reduction. This corresponds indeed to the shift in pin power errors towards deeper negative values, shown in Figure 4.33.

In the fast group, as seen in the (UOX + Gd) colorset as well, the cross section correction following rehomogenization is less adequate at reproducing the results from the reference spectrum correction, again implying that spectral rehomogenization in its current implementation does not perform well at reconstructing the reference fast group spectrum.

Lastly we consider the error distributions on the absorption cross sections in both groups, shown in Figure 4.35. Most cells show a decrease in thermal absorption cross section error. However, a large underestimation of the thermal cross section error is introduced at the water rods in the MOX assembly. It is clear that these underestimations must be mainly responsible for the large deterioration in thermal absorption cross section errors observed in Table 4.13.

When disregarding the water rods, RMS errors on thermal absorption cross sections change to 2.043 %, 1.343 % and 1.554 % for calculations (a), (b) and (c) respectively. This means a noticable error reduction overall, but also an overcorrection.

Again the fast group cross section correction following rehomogenization is poor, except for the overestimation correction at the UOX assembly edge. A similar overestimation correction on the fast group absorption cross section has been observed in the pin checkerboard configuration discussed in subsection 4.2.2.

The effect of rehomogenization on the water rods in the MOX assembly is further investigated by considering a checkerboard configuration of water rods neighbouring 7.77 wt% PuO_2 MOX pins displayed schematically in Figure 4.36. Results for all simulations are displayed in Table 4.14.

The infinite medium fast group absorption cross section of the MOX pin shows a 15 % underestimation of its value in the checkerboard environment, which demonstrates the large moderation effect of the water rod on its surroundings. Rehomogenization, however, substantially reduces this error and comes close to the reference spectrum correction. The latter result however, is still subject to a substantial error. This applies to the thermal group as well.

The thermal absorption cross section error magnitude in the water rod is increased following rehomogenization, just as seen in the colorset. From the spectrum variation reconstruction in Figure 4.37 it becomes clear that rehomogenization gives a poor reconstruction of the environmental spectrum in the water rod, with the reconstruction being of opposite sign to the reference spectrum variation in a large part of the thermal region.

Since the magnitude of the thermal range spectrum variation is large overall, errors resulting from this inaccuracy quickly become large as well, even considering the small magnitude of the cross section lethargy distribution in the region associated with non-zero spectrum variation, as seen in Figure 4.38.

One possible explanation for this behaviour may lie in an inconsistency in the method. Due to water rods being homogenized in a 3×3 configuration, some environmental effects have already been accounted for during the initial homogenization. Then accounting for these a second time, via rehomogenization, could result in the introduction of these errors. In this case one may consider to exclude the water rods from rehomogenization, or to obtain input cross sections via a different method, such as a transport calculation with a fixed external neutron source.

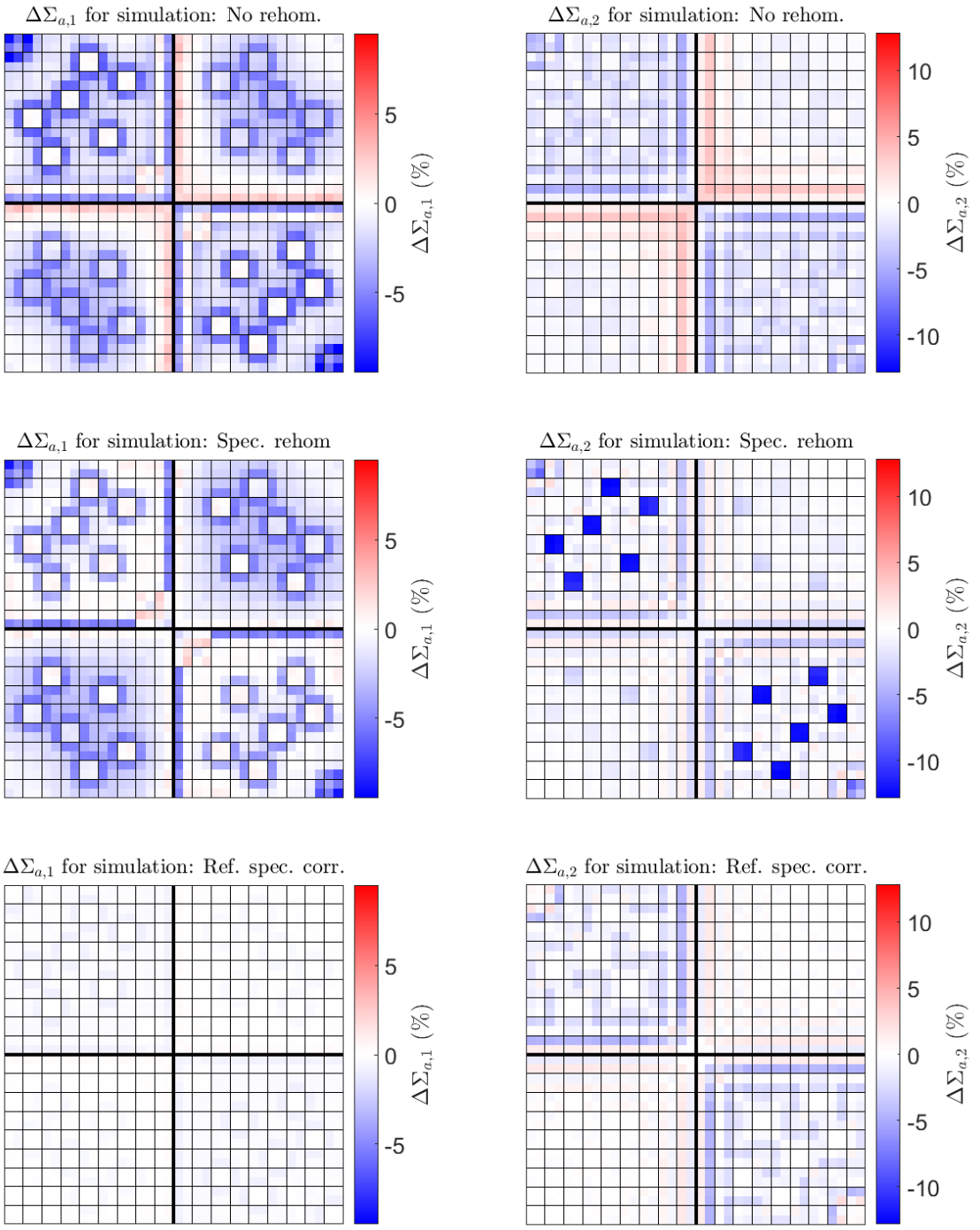

Figure 4.35: Absorption cross section error distributions for the standard pin-by-pin nodal simulation (top), nodal calculation with spectral rehomogenization (middle) and reference spectrum correction (bottom), for the fast (left) and thermal (right) energy groups.

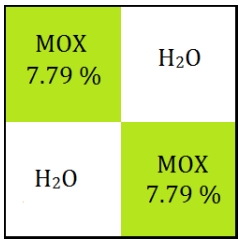

Figure 4.36: Schematic layout of the (Water channel + MOX 7.77 % pin) checkerboard.

Table 4.14: Comparison of absorption cross section errors resulting from the various simulation types, per energy group and per cell type of the (Water channel + MOX 7.77 % pin) pin checkerboard.

	H_2O		MOX 7.77 %	
Simulation	$\Delta\Sigma_{a,1}$ (%)	$\Delta\Sigma_{a,2}$ (%)	$\Delta\Sigma_{a,1}$ (%)	$\Delta\Sigma_{a,2}$ (%)
Reference (cm^{-1})	0.001399	0.04738	0.01871	0.3367
No rehom. (a)	-9.633	-5.553	-15.00	-5.788
Spec rehom. (b)	6.034	-8.454	-5.686	-1.861
Rehom. w/ ref. spec. (c)	0.04503	0.2766	-2.168	-3.171

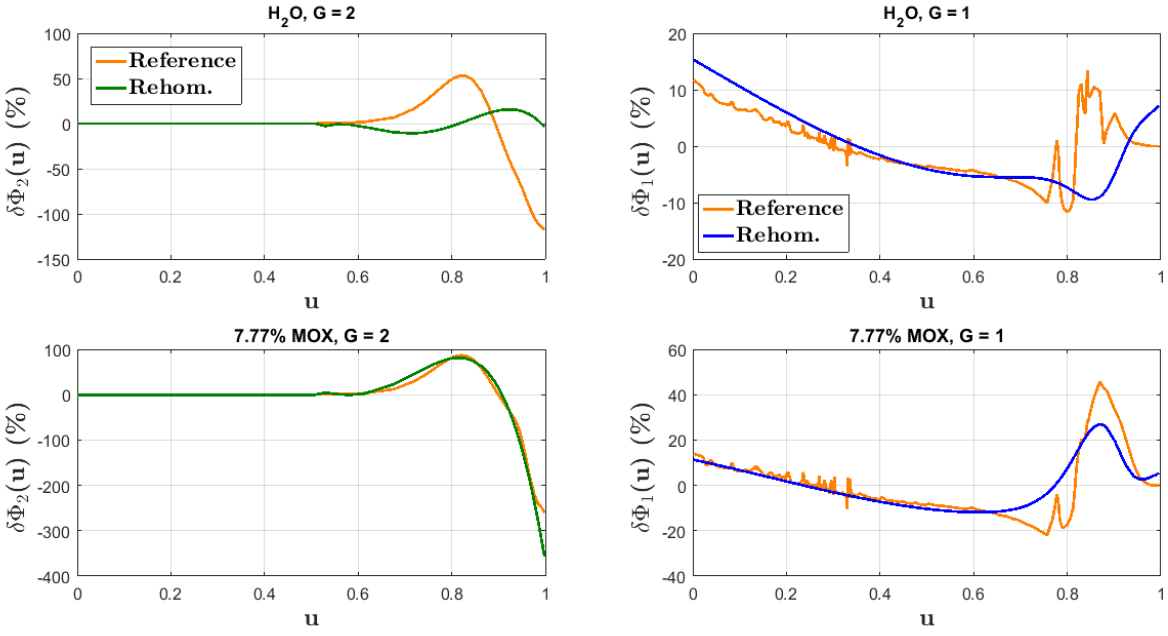

Figure 4.37: Reference spectrum variation and reconstruction for both energy groups in both cell types of the (Water channel + MOX 7.77 % pin) checkerboard.

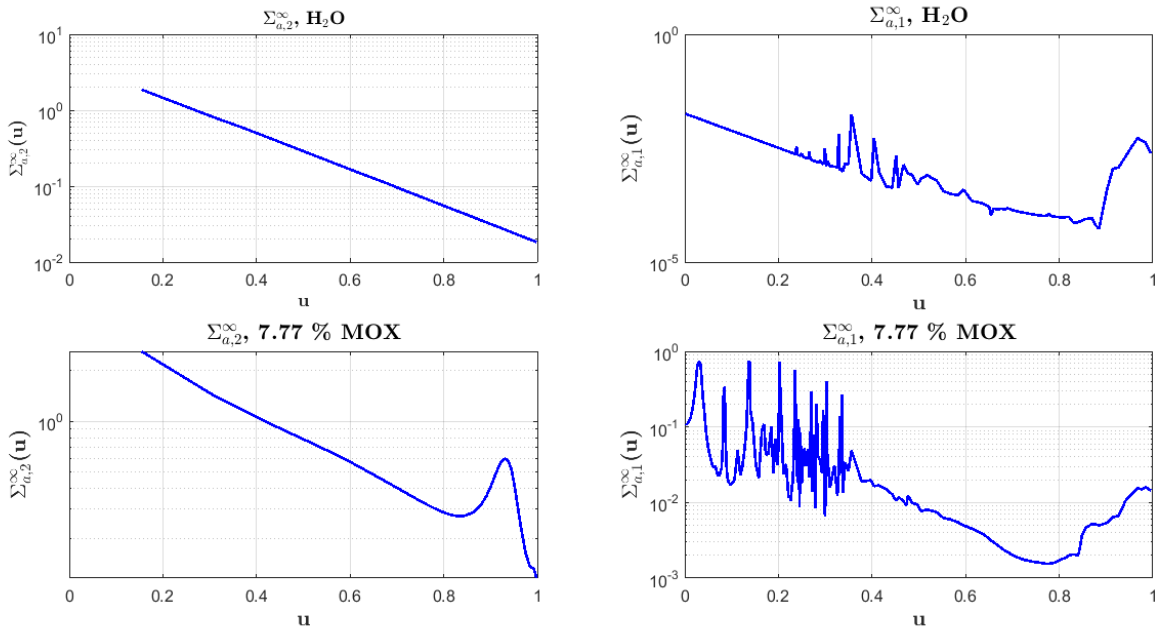

Figure 4.38: 3×3 **/ infinite medium absorption cross section lethargy distribution for both energy groups in both cell types of the (Water channel + MOX 7.77 % pin) checkerboard.**

4.5.1 Summary

The findings regarding spectral rehomogenization in the (UOX + MOX) colorset are to a large extent similar to those in the (UOX + Gd) colorset, in the sense that overall reference spectrum corrected cross sections are well approximated in the thermal group (with exception of those in the water rods), but less so in the fast group. Pin power errors have been found to increase, although this is in line with the shift from nodal calculations employing infinite medium cross sections to those with reference environmental ones. Furthermore, while some error reduction is achieved in thermal group fission neutron production cross sections via reference spectrum correction or rehomogenization, errors up to 5-6 % persist, suggesting a strong effect related to the intra-nodal spatial flux distribution as well. Finally, profound errors on the thermal group cross sections are introduced in the MOX assembly water rods following rehomogenization. These large errors are caused by a failure to reconstruct the thermal group spectrum variation.

Chapter 5

Conclusions and Recommendations

The cross section spectral rehomogenization model developed at AREVA NP has been applied to two-group pin-by-pin diffusion criticality calculations with a nodal expansion method on infinite pin checkerboards and assembly colorsets. Resulting pin power distributions, cross sections and the multiplication factor k_{eff} have been compared to the results of reference discrete ordinates transport calculations in order to determine the feasibility at the pin-level and its accuracy.

The rehomogenization method has been validated in two pin checkerboard test cases, in which it has been estabilished that spectral cross section effects in the thermal group can generally be well recovered. Error reductions in most fast group cross sections are less substantial in the present implementation, and some cross sections even deteriorate, although the consequences of the latter are limited. Moreover, the cross section corrections have been found to be consistent with the reconstruction of the spectrum variations. Pin power distributions and the multiplication factor have been shown to drastically improve in both cases following rehomogenization.

A parameter study has been performed on the effect of the enrichment difference as a heterogeneity measure on the errors in the aforementioned parameters in a pin checkerboard system. Reference spectrum corrections show substantial improvement in every quantity over the whole heterogeneity range, and while with spectral rehomogenization improvements on k_{eff} and pin powers are attained as well, above a certain level of heterogeneity larger inaccuracies are introduced to some fast group cross sections due to the limited capability of spectrum reconstruction in the epithermal region. A different set of weighting functions may improve these results. Increasing the order of the rehomogenization expansion does not solve this issue. The limited-accuracy spectrum variation reconstruction may also be partly attributed to inconsistencies between the neutron diffusion and neutron transport paradigms.

The spectral rehomogenization method has been applied to a colorset of UOX and Gd-loaded assemblies, as well as a colorset of UOX and MOX assemblies. In the (UOX + Gd) colorset, thermal absorption cross sections for the Gd-loaded rods have improved drastically. Pin power errors are reduced in the center of the Gd-loaded assembly, as well as in fuel rods neighbouring Gd rods, but not in the center of the UOX assembly. This problem has been attributed to the persisting errors in the cross section error distribution for down-scattering to the thermal group, which itself is a consequence of the limited epithermal spectrum reconstruction capability. The multiplication factor k_{eff} is underestimated following rehomogenization by several hundreds of pcm, but approaches the value obtained with reference environmental cross sections. This error is therefore attributed to the diffusion approximation.

In the (UOX + MOX) colorset, spectral rehomogenization slightly reduces the thermal fission cross sections, but errors persist to some extent, even after reference spectrum correction. An investigation of spatial effects may be beneficial. Thermal group absorption cross sections also improve for most cells, however large errors are introduced in the thermal absorption cross sections in MOX assembly water rods. This may be a consequence of inconsistencies in the methodology, leading to a failure to reconstruct the spectrum variation accurately. Spectral rehomogenization yields an overall

increase in pin power error magnitude, but the resulting error distribution approximates the result of a pin-by-pin diffusion calculation with reference environmental cross sections, suggesting a good overall approximation of the reference environmental cross sections most relevant to the fission power.

A common feature found in the results is the limited capability of spectrum variation reconstruction by rehomogenization, generally in the epithermal region of the fast group. One could opt to change the sets of basis and weighting functions for the rehomogenization expansion, such as by replacing one of the fast group (Galerkin) weighting functions by a weighting function that weighs in more heavily towards the epithermal end, as the behaviour in this region is dominant in determining the fast-group cross sections.

Some experience has already been obtained also with a proper orthogonal decomposition-based method at the assembly level [16], which could be extended to the pin-by-pin level as well.

Part of the fast group errors may also be attributed to the diffusion approximation, specifically in the fast group. A further investigation on how fast group flux errors influence the conditioning of the rehomogenization problem is recommended.

The rehomogenization method was validated using reference results for the neutron leakage lethargy distributions. For practical applications, a leakage model based exclusively on information available from the nodal diffusion calculation must be implemented. Since the diffusion approximation is suitable to limited extent for pin-by-pin calculations, the accuracy of the results is expected to somewhat decline. Rigourously, adressing the leakage model should be accompanied by an investigation on spectral corrections to diffusion coefficients, as employed in [6].

Furthermore, infinite medium data for water channels have been obtained from periodic configurations of water channels being spaced three unit fuel cells apart in both radial directions. Although broad group nodal cross sections from this approach have been validated, this is not the case for cross section fine-group or continuous energy distributions. This may provide a source of error that may partly cause the thermal absorption cross section deterioration observed in the (UOX + MOX) colorset. One may consider a different approach, preferably more consistent with infinite medium fuel cell homogenization. Alternatively one may choose to exclude the water rods from rehomogenization.

A source of inconsistency with conventional nodal methods is introduced by using infinite medium data from regular criticality calculations. Conventionally infinite medium cross sections and discontinuity factors are obtained by weighting fine-group cross sections with spectra obtained through a critical buckling search [12]. Attempts to validate that the resulting infinite medium data should reproduce a unity multiplication factor in a two-group diffusion problem have been unsuccessful. Consequently regular criticality calculation data have been used.

Finally, a better reproduction of the reference results may be possible to obtain when the complete rehomogenization model is utilized, including corrections to spatial and burnup effects. A potential weakness however lies in the cancellation of favourable error reductions, as corrections related to different effects may be of different signs [6].

Bibliography

[1] J. Leppänen, *Development of a New Monte Carlo Reactor Physics Code*, PhD thesis, VTT, 2007

[2] J.J. Duderstadt, L.J. Hamilton, *Nuclear Reactor Analysis*, John Wiley and sons, 1976

[3] W.M. Stacey, *Nuclear Reactor Physics*, Wiley-VCH Verlag GmbH & Co, 2007

[4] A. Dall'Osso, *A spatial rehomogenization method in nodal calculations*, Annals of Nuclear Energy 33, pp. 869-877, 2006

[5] A. Dall'Osso, D. Tomatis, Y. Du *Improving Cross Sections via Spectral Rehomogenization*, Proceedings of International Conference: PHYSOR 2010

[6] M. Gamarino, D. Tomatis, A. Dall'Osso, D. Lathouwers, J.L. Kloosterman, T.H.J.J. van der Hagen, *Investigation of Rehomogenization in the Framework of Nodal Cross Section Corrections*, Proceedings of International Conference: PHYSOR 2016

[7] *Evaluated Nuclear Data File (ENDF)*, National Nuclear Data Center, Brookhaven National Laboratory, 2011-12-22, retrieved 2017-04-12 ¡http://www.nndc.bnl.gov/¿

[8] R.D. Lawrence, *Progress in Nodal Methods for the Solution of the Neutron Diffusion and Transport Equations*, Progress in Nuclear Energy, Vol. 17, No. 3, pp. 271-301, 1986

[9] K. Koebke, *A new approach to homogenization and group condensation*, IAEA Technical Committee Meeting on Homogenization Methods in Reactor Physics, 1978

[10] K.S. Smith, *Spatial homogenization methods for Light Water Reactors*, Thesis, Massachusetts Institute of Technology, 1980

[11] K.S. Smith, *Assembly Homogenization Techniques for Light Water Reactor Analysis*, Progress in Nuclear Energy, Vol. 17, No. 3, pp. 303-335, 1986

[12] B.T. Rearden, M.A. Jessee, *SCALE Code System, ORNL/TM-2005/39 Version 6.2*, Oak Ridge National Laboratory, 2016

[13] A. Yamamoto, Y. Kitamura, Y. Yamane, *Cell homogenization methods for pin-by-pin core calculations tested in slab geometry*, Annals of Nuclear Energy 31, pp. 825-847, 2004

[14] A. Yamamoto, M. Tatsumi, Y. Kitamura, Y. Yamane, *Improvement of the SPH Method for Multi-assembly Calculations*, Proceedings of International Conference: PHYSOR 2004

[15] Y. Berman, *An improved homogenization technique for pin-by-pin diffusion calculations*, Annals of Nuclear Energy 53, pp. 238-243, 2013

[16] M. Gamarino, A. Dall'Osso, D. Lathouwers, J.L. Kloosterman, *Spectral Rehomogenization of Nodal Cross-Sections via Proper Orthogonal Decomposition*, Proceedings of International Conference: M&C 2017

[17] M. Tatsumi, A. Yamamoto *Advanced PWR Core Calculation Based on Multi-group Nodal-transport Method in Three-dimensional Pin-by-Pin Geometry*, Journal of Nuclear Science and Technology, 40:6, pp. 376-387, 2003

[18] T. Kozlowski, Y. Xu, T.J. Downar, D.Lee *Cell Homogenization Method for Pin-by-Pin Neutron Transport Calculations*, Nuclear Science and Engineering: 169, pp. 1-18, 2011

[19] M. Tatsumi, A. Yamamoto, S. Kosaka, E. Saji, *A study on oeffects of pin cell homogenization in an actual reactor core geometry*, Proceedings of the International Conference: PHYSOR 2000

[20] K.S. Smith, *Practical and Efficient Iterative Method for LWR Fuel Assembly Homogenization*, Transactions of the American Nuclear Society, 71, 1994

[21] A. Dall'Osso, *Introducing the migration mode method for the solution of the space and energy dependent diffusion equation*, Annals of Nuclear Energy 30, pp. 1829-1845, 2003

[22] T.J. Downar, D. Lee, Y. Xu, T. Kozlowski, *PARCS v2.6, U.S. NRC Core Neutronics Simulator, Theory Manual*, Purdue University, 2004

[23] J.R. Lamarsh, *Introduction to Nuclear Reactor Theory*, Addison-Wesley, 1966

Appendices

Appendix A

Validation of non-fissile input cross sections

As a criticality calculation on non-multiplying media cannot be performed, a different approach must be sought to determine input cross sections of non-fissile materials for nodal diffusion calculations. The current approach is to surround the non-fissile cells (such as water rods) by fuel pins of the type that surrounds them in the real environment in a 3×3 pin configuration with reflective boundary conditions.

This approach offers a configuration of limited complexity for the lattice calculation. Additionally, the three-cell spacing between water rods near the center of the UOX and UGd assemblies is maintained by this approach.

In order to validate this approach, the cross sections resulting from a transport calculation on such 3×3 configurations are compared to the cross sections from a 1.80 % UOX fuel assembly calculation with reflective boundary conditions. The assembly layout and material compositions are identical to those of the 1.80 % UOX assembly described in Appendix B.2.1. The pin cells in the assembly calculation here are homogenized on a one-node-per-pin basis. The relative deviations for the single pin or 3×3 cross sections with respect to the single assembly values are displayed in the figures below for the reactions: total, absorption, fission neutron production, out-scattering and self-scattering.

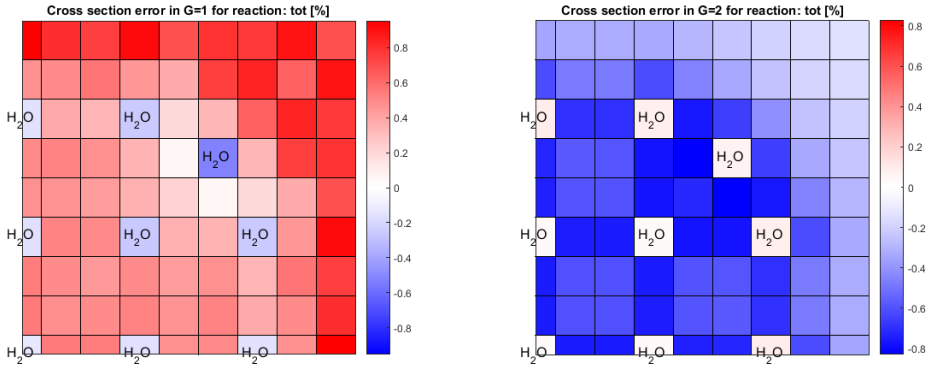

Figure A.1: Total cross section percentual deviations of 1.80 % UO_2 pins and water rods from their infinite medium or (3×3) calculations with respect to their respective values in an infinite array of UOX assemblies.

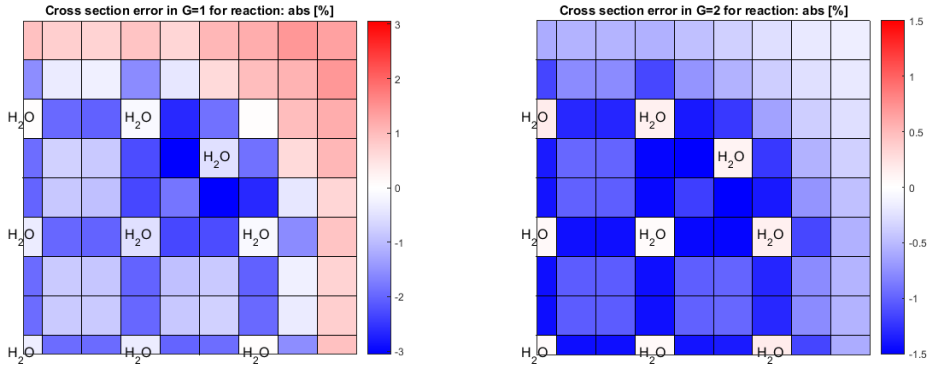

Figure A.2: Absorption cross section percentual deviations of 1.80 % UO_2 pins and water rods from their infinite medium or (3×3) calculations with respect to their respective values in an infinite array of UOX assemblies.

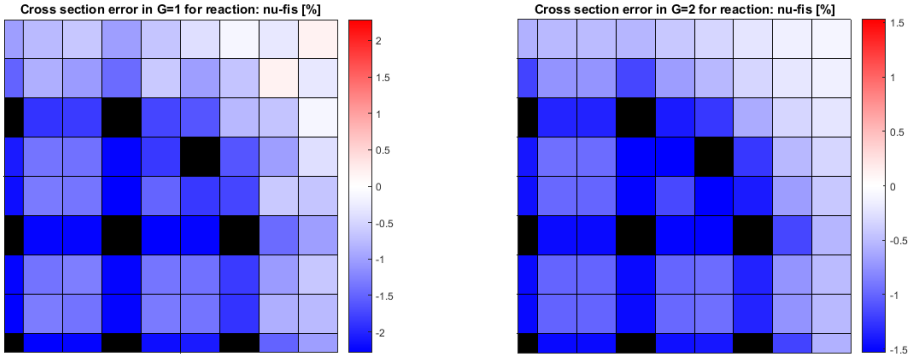

Figure A.3: Fission neutron production cross section percentual deviations of 1.80 % UO_2 pins and water rods from their infinite medium or (3×3) calculations with respect to their respective values in an infinite array of UOX assemblies.

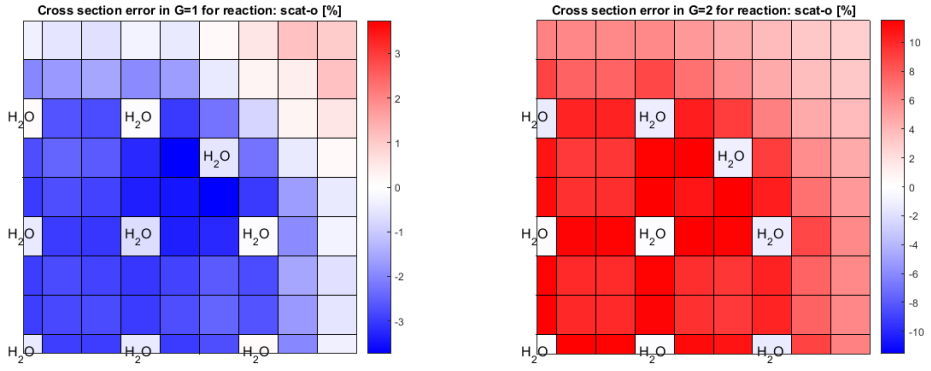

Figure A.4: Out-scattering cross section percentual deviations of 1.80 % UO_2 pins and water rods from their infinite medium or (3×3) calculations with respect to their respective values in an infinite array of UOX assemblies.

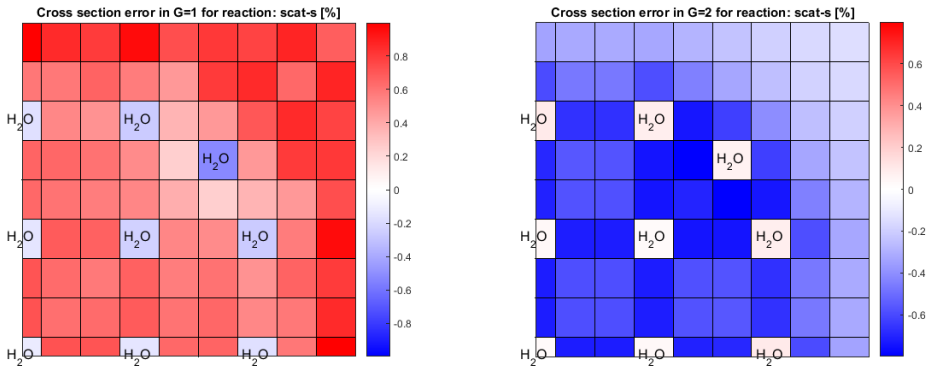

Figure A.5: Self-scattering cross section percentual deviations of 1.80 % UO_2 pins and water rods from their infinite medium or (3×3) calculations with respect to their respective values in an infinite array of UOX assemblies.

For none of the reactions considered are the cross section deviations of the water rods of large magnitude compared to those of the UO_2 cells. Thus the present approach of using cross sections for non-fissile cells from a transport calculation on a 3×3 configuration is deemed justified.

Appendix B

Checkerboard and assembly layouts and compositions

B.1 Checkerboard configurations

B.1.1 UO_2 pin checkerboard with varying enrichments

In the pin checkerboard configuration with varying enrichment, the extent of pin-by-pin heterogeneity is expressed in a single metric - the fuel enrichment difference between two adjacent pins. The infinite two-dimensional checkerboard is simulated using a configuration of four quarter-cells with reflective boundary conditions, described in Figure B.1.

Table B.1 contains a detailed description of the 1.80 % enriched unit cell parameters: radii, temperature and isotopic composition as well as global parameters. The isotopic compositions of differently enriched fuel pins are identical with the exception of the ^{235}U and ^{238}U densities. These are determined by asserting that their total nuclide density ($N_{\mathrm{U}-235} + N_{\mathrm{U}-238}$) is maintained and that:

$$\frac{235N_{\mathrm{U}-235}}{234N_{\mathrm{U}-234} + 235N_{\mathrm{U}-235} + 236N_{\mathrm{U}-236} + 238N_{\mathrm{U}-238}} = \frac{e}{100}$$

Where e is the fuel enrichment in %.

Table B.1: Geometric parameters and compositions of the 1.80 % UO_2 fuel cell. Atom species without mass number denote natural composition. The notation $R\mathbf{E}\pm x$ is equivalent to $R\cdot 10^{\pm x}$.

Zone	fuel	void	cladding
Radius (cm)	0.409575	0.417875	0.474876
Temperature (K)	845.95	670.0	581.83
Isotopes (density$((\mathrm{b}\cdot\mathrm{cm})^{-1})$)	^{16}O (4.589E-2)	^{4}He 1.0E-15	C (5.752E-5)
	^{234}U (5.958E-6)		^{50}Cr (3.296E-6)
	^{235}U (4.182E-4)		^{52}Cr (6.356E-5)
	^{236}U (1.253E-6)		^{53}Cr (7.208E-6)
	^{238}U (2.252E-2)		^{54}Cr (1.794E-6)
	^{238}Pu (2.602E-9)		Fe (1.483E-4)
	^{239}Pu (2.591E-9)		^{16}O (3.083E-4)
	^{240}Pu (2.580E-9)		Si (8.427E-6)
	^{241}Pu (2.570E-9)		Zr (4.241E-2)
	^{242}Pu (2.559E-9)		^{112}Sn (4.674E-6)
			^{114}Sn (3.180E-6)
			^{115}Sn (1.638E-6)
			^{116}Sn (7.005E-5)
			^{117}Sn (3.700E-5)
			^{118}Sn (1.167E-4)
			^{119}Sn (4.139E-5)
			^{120}Sn (1.570E-4)
			^{122}Sn (2.231E-5)
			^{124}Sn (2.790E-5)
Cell pitch (cm): 1.261984	ρ_{mod} ($\mathrm{g\,cm^{-3}}$): 0.7142	T_{mod} (K): 579.55	ρ_{B-10} (ppm): 1465.0

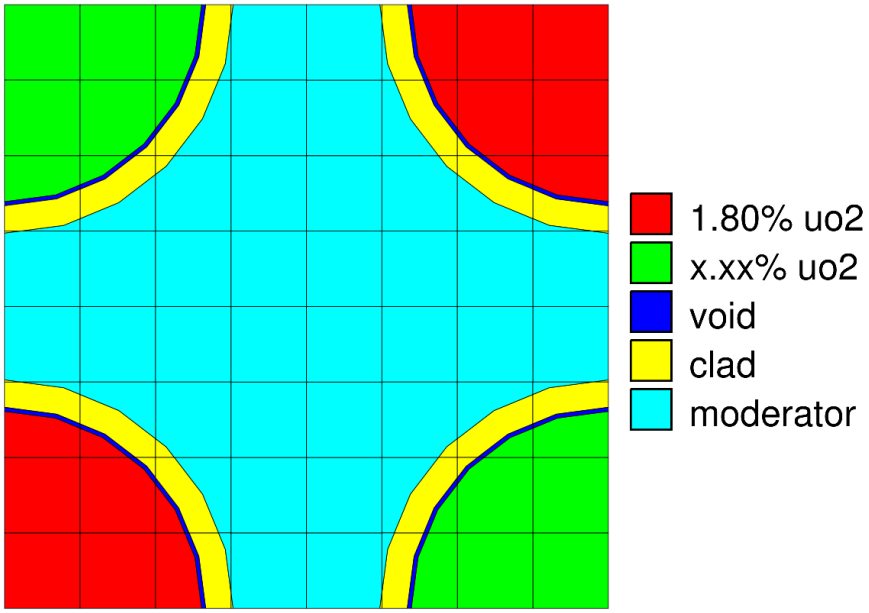

Figure B.1: Pin checkerboard layout for 1.80 % UO_2 fuel pins neighbouring UO_2 fuel pins with varying enrichments.

B.1.2 UO_2 – MOX checkerboard

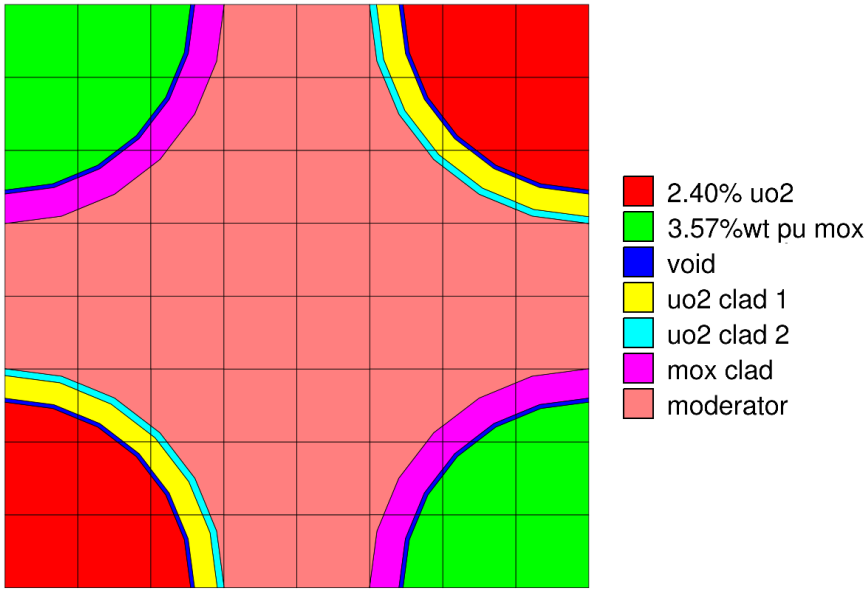

Figure B.2: Pin checkerboard layout for double-clad 2.40 % UO_2 fuel pins neighbouring MOX fuel pins with 3.57 % PuO_2 weight.

Table B.2: Geometric parameters and compositions of the unit cells constituting the UOX - MOX pin checkerboard. Atom species without mass number denote natural composition. The notation $R\mathbf{E}\pm x$ is equivalent to $R\cdot 10^{\pm x}$.

Zone	fuel	void	clad 1	clad 2
Radius (cm)	0.4025	0.411	0.46	0.475
Temperature (K)	845.95	670.0	581.83	581.83
Isotopes (density$((\mathrm{b}\cdot\mathrm{cm})^{-1})$)	^{16}O (4.576E-2)	^{4}He 1.0E-15	C (4.988E-5)	^{50}Cr (5.646E-6)
	^{234}U (8.996E-6)		^{50}Cr (2.858E-6)	^{52}Cr (1.089E-4)
	^{235}U (5.558E-4)		^{52}Cr (5.512E-5)	^{53}Cr (1.235E-5)
	^{236}U (2.616E-6)		^{53}Cr (6.250E-6)	^{54}Cr (3.073E-6)
	^{238}U (2.230E-2)		^{54}Cr (1.556E-6)	Fe (1.993E-4)
	^{238}Pu (2.594E-9)		Fe (1.286E-4)	^{16}O (3.479E-4)
	^{239}Pu (2.583E-9)		^{16}O (2.673E-4)	Si (1.344E-5)
	^{240}Pu (2.572E-9)		Si (7.307E-6)	Zr (4.296E-2)
	^{241}Pu (2.561E-9)		Zr (3.678E-2)	^{112}Sn (2.598E-6)
	^{242}Pu (2.551E-9)		^{112}Sn (4.053E-6)	^{114}Sn (1.768E-6)
			^{114}Sn (2.757E-6)	^{115}Sn (9.107E-7)
			^{115}Sn (1.421E-6)	^{116}Sn (3.895E-5)
			^{116}Sn (6.075E-5)	^{117}Sn (2.057E-5)
			^{117}Sn (3.209E-5)	^{118}Sn (6.487E-5)
			^{118}Sn (1.012E-4)	^{119}Sn (2.301E-5)
			^{119}Sn (3.589E-5)	^{120}Sn (8.727E-5)
			^{120}Sn (1.361E-4)	^{122}Sn (1.240E-5)
			^{122}Sn (1.935E-5)	^{124}Sn (1.551E-5)
			^{124}Sn (2.419E-5)	
			^{4}He (2.098E-17)	

(a) Geometric parameters and compositions of the double-clad 2.40 % UO_2 fuel cell.

Zone	fuel	void	clad
Radius (cm)	0.4025	0.411	0.475
Temperature (K)	845.95	670.0	581.83
Isotopes (density$((\mathrm{b}\cdot\mathrm{cm})^{-1})$)	^{241}Am (1.161E-5)	^{4}He (1.0E-15)	^{4}He (1.635E-17)
	^{16}O (4.606E-2)		^{93}Nb (3.784E-4)
	^{238}Pu (1.553E-5)		^{16}O (3.077E-4)
	^{239}Pu (4.627E-4)		S (2.467E-6)
	^{240}Pu (2.201E-4)		Zr (3.810E-2)
	^{241}Pu (6.648E-5)		
	^{242}Pu (5.210E-5)		
	^{234}U (1.746E-7)		
	^{235}U (5.711E-5)		
	^{236}U (2.635E-9)		
	^{238}U (2.214E-2)		

(b) Geometric parameters and compositions of the 3.57 % wt PuO_2 MOX fuel cell.

Cell pitch (cm):	ρ_{H_2O} ($\mathrm{g\,cm^{-3}}$):	T_{mod} (K):	ρ_{B-10} (ppm):
1.27970	0.7142	579.55	2899.6

(c) Global parameters and moderator properties of the UOX - MOX pin checkerboard

B.2 Assemblies for the (UOX + Gd) colorset

B.2.1 1.80% UOX assembly (17 × 17)

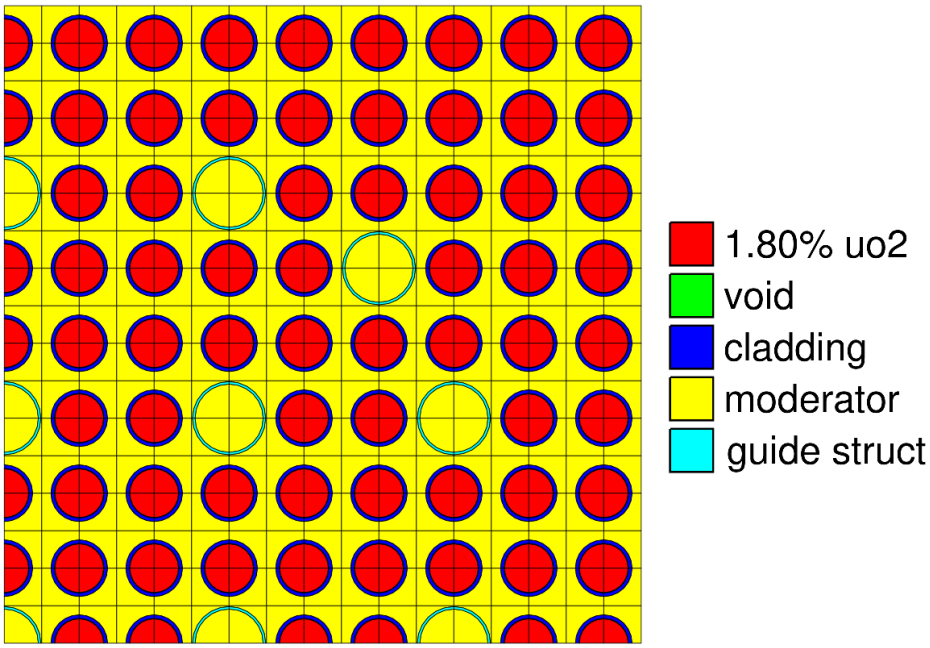

Figure B.3: Layout for the UOX fuel assembly used in the (UOX + Gd) colorset. The cell types employed in this assembly are (*a*) 1.80 % UO_2 fuel rods and (*b*) water channels surrounded by guide tubes for control rods and detectors.

Table B.3: Geometric parameters and compositions of the unit cells constituting the UOX assembly. Atom species without mass number denote natural composition. The notation $R\mathbf{E} \pm x$ is equivalent to $R \cdot 10^{\pm x}$.

Zone	fuel	void	cladding
Radius (cm)	0.409575	0.417875	0.474875
Temperature (K)	841.00	670.0	579.55
Isotopes (density$((\mathrm{b}\cdot\mathrm{cm})^{-1})$)	^{16}O (4.589E-2)	^{4}He (1.E-15)	C (5.070E-5)
	^{238}Pu (2.602E-9)		^{50}Cr (2.905E-6)
	^{239}Pu (2.591E-9)		^{52}Cr (5.603E-5)
	^{240}Pu (2.580E-9)		^{53}Cr (6.353E-6)
	^{241}Pu (2.570E-9)		^{54}Cr (1.581E-6)
	^{242}Pu (2.559E-9)		Fe (1.307E-4)
	^{234}U (2.818E-6)		^{4}He (1.784e-17)
	^{235}U (4.182E-4)		^{16}O (2.717E-4)
	^{236}U (9.887E-7)		Si (7.427E-6)
	^{238}U (2.252E-2)		Zr (3.738E-2)
			^{112}Sn (4.119E-6)
			^{114}Sn (2.803E-6)
			^{115}Sn (1.444E-6)
			^{116}Sn (6.175E-5)
			^{117}Sn (3.261E-5)
			^{118}Sn (1.029E-4)
			^{119}Sn (3.648E-5)
			^{120}Sn (1.384E-4)
			^{122}Sn (1.966E-5)
			^{124}Sn (2.459E-5)

(a) Geometric parameters and compositions of the 1.80 % UO_2 fuel cell.

Radius (cm)	inner: 0.5723786	outer: 0.6129408
Temperature (K)		579.55
Isotopes (density$((\mathrm{b}\cdot\mathrm{cm})^{-1})$)		C (5.734E-5)
		^{50}Cr (3.286E-6)
		^{52}Cr (6.337E-5)
		^{53}Cr (7.186E-6)
		^{54}Cr (1.789E-6)
		Fe (1.479E-4)
		^{16}O (3.073E-4)
		Si (8.401E-6)
		Zr (4.228E-2)
		^{112}Sn (4.659E-6)
		^{114}Sn (3.170E-6)
		^{115}Sn (1.633E-6)
		^{116}Sn (6.984E-5)
		^{117}Sn (3.689E-5)
		^{118}Sn (1.163E-4)
		^{119}Sn (4.126E-5)
		^{120}Sn (1.565E-4)
		^{122}Sn (2.224E-5)
		^{124}Sn (2.781E-5)

(b) Geometric parameters and composition of the guide tubes.

Cell pitch (cm):	ρ_{mod} ($\mathrm{g\,cm^{-3}}$):	T_{mod} (K):	ρ_{B-10} (ppm):
1.26558	0.7142	579.55	1829.1

(c) Global parameters and moderator properties of the UOX assembly.

B.2.2 3.90% UOX assembly with (0.25% UO_2 + 7.65% GdO) loading (17 × 17)

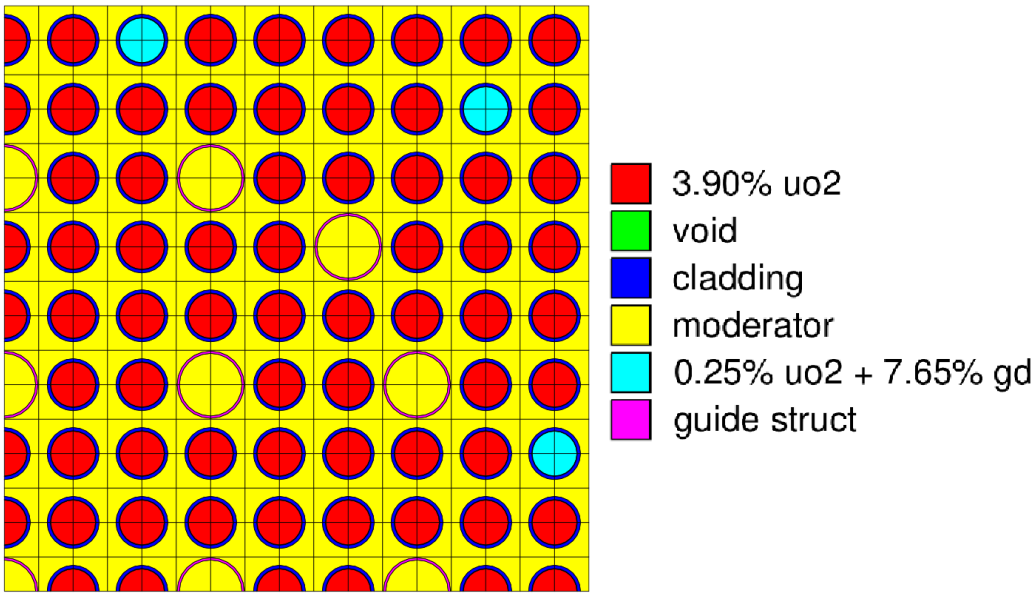

Figure B.4: Layout for the UGd fuel assembly used in the (UOX + Gd) colorset. The cell types employed in this assembly are (*a*) 3.90 % UO_2 fuel rods, (*b*) 0.25 % UO_2 rods with 7.65 % Gd loading and (*c*) water channels surrounded by guide tubes.

Table B.4: Geometric parameters and compositions of the unit cells constituting the UGd assembly. Atom species without mass number denote natural composition. The notation $R\mathbf{E}\pm x$ is equivalent to $R\cdot 10^{\pm x}$.

Zone	fuel	void	cladding
Radius (cm)	0.409600	0.417875	0.474875
Temperature (K)	841.00	670.0	579.55
Isotopes (density$((\mathrm{b}\cdot\mathrm{cm})^{-1})$)	^{16}O (4.571E-2)	^{4}He (1.E-15)	C (5.070E-5)
	^{238}Pu (2.592E-9)		^{50}Cr (2.905E-6)
	^{239}Pu (2.581E-9)		^{52}Cr (5.603E-5)
	^{240}Pu (2.570E-9)		^{53}Cr (6.353E-6)
	^{241}Pu (2.559E-9)		^{54}Cr (1.581E-6)
	^{242}Pu (2.549E-9)		Fe (1.307E-4)
	^{234}U (7.858E-6)		^{4}He (1.784e-17)
	^{235}U (9.024E-4)		^{16}O (2.717E-4)
	^{236}U (1.411E-6)		Si (7.427E-6)
	^{238}U (2.195E-2)		Zr (3.738E-2)
			^{112}Sn (4.112E-6)
			^{114}Sn (2.803E-6)
			^{115}Sn (1.444E-6)
			^{116}Sn (6.175E-5)
			^{117}Sn (3.261E-5)
			^{118}Sn (1.029E-4)
			^{119}Sn (3.648E-5)
			^{120}Sn (1.384E-4)
			^{122}Sn (1.966E-5)
			^{124}Sn (2.459E-5)

(a) Geometric parameters and compositions of the 3.90 % UO_2 fuel cell.

Table B.4: Geometric parameters and compositions of the unit cells constituting the UGd assembly (continued).

Zone	fuel	void	cladding
Radius (cm)	0.409600	0.417875	0.474875
Temperature (K)	841.00	670.0	579.55
Isotopes (density$((\mathrm{b}\cdot\mathrm{cm})^{-1})$)	^{16}O (4.4989E-2)	^{4}He (1.E-15)	C (5.070E-5)
	^{238}Pu (2.528E-9)		^{50}Cr (2.905E-6)
	^{239}Pu (2.517E-9)		^{52}Cr (5.603E-5)
	^{240}Pu (2.507E-9)		^{53}Cr (6.353E-6)
	^{241}Pu (2.496E-9)		^{54}Cr (1.581E-6)
	^{242}Pu (2.486E-9)		Fe (1.307E-4)
	^{234}U (2.571E-9)		^{4}He (1.784e-17)
	^{235}U (5.191E-5)		^{16}O (2.717E-4)
	^{236}U (6.017E-7)		Si (7.427E-6)
	^{238}U (2.045E-2)		Zr (3.738E-2)
	^{152}Gd (5.312E-6)		^{112}Sn (4.119E-6)
	^{154}Gd (5.790E-5)		^{114}Sn (2.803E-6)
	^{155}Gd (3.931E-4)		^{115}Sn (1.444E-6)
	^{156}Gd (5.437E-4)		^{116}Sn (6.175E-5)
	^{157}Gd (4.157E-4)		^{117}Sn (3.261E-5)
	^{158}Gd (6.598E-4)		^{118}Sn (1.029E-4)
	^{160}Gd (5.806E-4)		^{119}Sn (3.648E-5)
			^{120}Sn (1.384E-4)
			^{122}Sn (1.966E-5)
			^{124}Sn (2.459E-5)

(b) Geometric parameters and compositions of the 0.25 % UO_2 cell loaded with 7.65 % wt GdO.

Radius (cm)	inner: 0.5723786	outer: 0.6129408
Temperature (K)		579.55
Isotopes (density$((\mathrm{b}\cdot\mathrm{cm})^{-1})$)		C (5.734E-5)
		^{50}Cr (3.286E-6)
		^{52}Cr (6.337E-5)
		^{53}Cr (7.186E-6)
		^{54}Cr (1.789E-6)
		Fe (1.479E-4)
		^{16}O (3.073E-4)
		Si (8.401E-6)
		Zr (4.228E-2)
		^{112}Sn (4.659E-6)
		^{114}Sn (3.170E-6)
		^{115}Sn (1.633E-6)
		^{116}Sn (6.984E-5)
		^{117}Sn (3.689E-5)
		^{118}Sn (1.163E-4)
		^{119}Sn (4.126E-5)
		^{120}Sn (1.565E-4)
		^{122}Sn (2.224E-5)
		^{124}Sn (2.781E-5)

(c) Geometric parameters and composition of the guide tubes.

Cell pitch (cm):	ρ_{mod} ($\mathrm{g\,cm^{-3}}$):	T_{mod} (K):	ρ_{B-10} (ppm):
1.26558	0.7142	579.55	1829.1

(d) Global parameters and moderator properties of the UGd assembly.

B.3 Assemblies for the (UOX + MOX) colorset

B.3.1 2.40% UOX assembly (18 × 18)

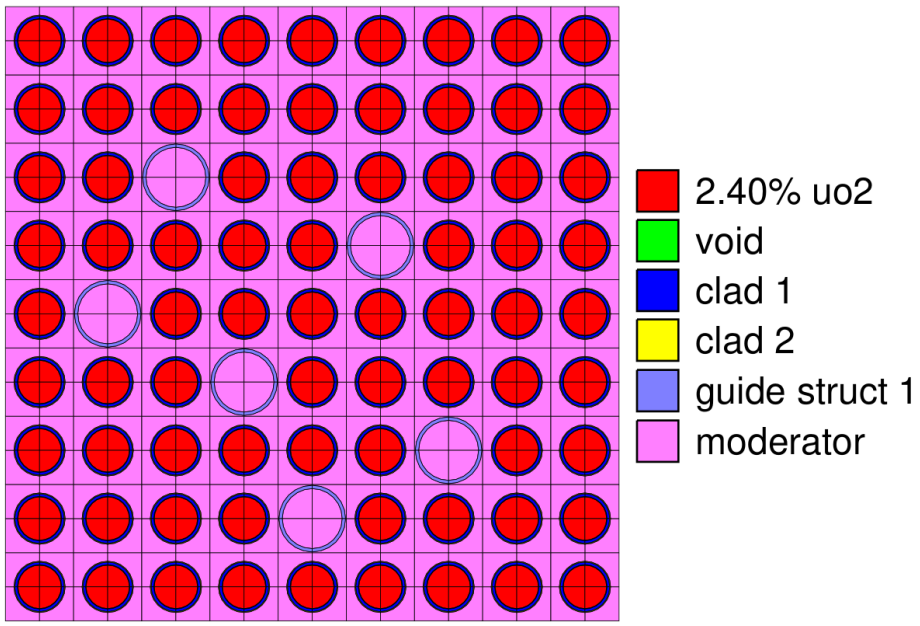

Figure B.5: Layout for the UOX fuel assembly used in the (UOX + MOX) colorset. The cell types employed in this assembly are (*a*) double-clad 2.40 % UO_2 fuel rods and (*b*) water channels surrounded by guide tubes.

Table B.5: Geometric parameters and compositions of the unit cells constituting the UOX assembly. Atom species without mass number denote natural composition. The notation $R\mathbf{E}\pm x$ is equivalent to $R\cdot 10^{\pm x}$.

Zone	fuel	void	clad 1	clad 2
Radius/*half-pitch* (cm)	0.4025	0.411	0.46	0.475
Temperature (K)	845.95	670.0	581.83	581.83
Isotopes (density$((\mathrm{b}\cdot\mathrm{cm})^{-1})$)	^{16}O (4.576E-2)	^{4}He 1.0E-15	C (4.988E-5)	^{50}Cr (5.646E-6)
	^{234}U (8.996E-6)		^{50}Cr (2.858E-6)	^{52}Cr (1.089E-4)
	^{235}U (5.558E-4)		^{52}Cr (5.512E-5)	^{53}Cr (1.235E-5)
	^{236}U (2.616E-6)		^{53}Cr (6.251E-6)	^{54}Cr (3.073E-6)
	^{238}U (2.230E-2)		^{54}Cr (1.556E-6)	Fe (1.993E-4)
	^{238}Pu (2.594E-9)		Fe (1.286E-4)	^{16}O (3.479E-4)
	^{239}Pu (2.583E-9)		^{16}O (2.673E-4)	Si (1.344E-5)
	^{240}Pu (2.572E-9)		Si (7.307E-6)	Zr (4.296E-2)
	^{241}Pu (2.561E-9)		Zr (3.678E-2)	^{112}Sn (2.598E-6)
	^{242}Pu (2.550E-9)		^{112}Sn (4.053E-6)	^{114}Sn (1.768E-6)
			^{114}Sn (2.757E-6)	^{115}Sn (9.107E-7)
			^{115}Sn (1.421E-6)	^{116}Sn (3.895E-5)
			^{116}Sn (6.075E-5)	^{117}Sn (2.057E-5)
			^{117}Sn (3.209E-5)	^{118}Sn (6.487E-5)
			^{118}Sn (1.012E-4)	^{119}Sn (2.301E-5)
			^{119}Sn (3.589E-5)	^{120}Sn (8.727E-5)
			^{120}Sn (1.361E-4)	^{122}Sn (1.240E-5)
			^{122}Sn (1.934E-5)	^{124}Sn (1.551E-5)
			^{124}Sn (2.419E-5)	
			^{4}He (2.098E-17)	

(a) Geometric parameters and compositions of the double-clad 2.40 % UO_2 fuel cell.

Radius (cm)	inner: 0.558600	outer: 0.616955
Temperature (K)		581.83
Isotopes (density$((\mathrm{b}\cdot\mathrm{cm})^{-1})$)		C (5.771E-5)
		^{50}Cr (3.307E-6)
		^{52}Cr (6.378E-5)
		^{53}Cr (7.232E-6)
		^{54}Cr (1.800E-6)
		Fe (1.488E-4)
		^{16}O (3.093E-4)
		Si (8.456E-6)
		Zr (4.256E-2)
		^{112}Sn (4.690E-6)
		^{114}Sn (3.191E-6)
		^{115}Sn (1.644E-6)
		^{116}Sn (7.029E-5)
		^{117}Sn (3.713E-5)
		^{118}Sn (1.171E-4)
		^{119}Sn (4.153E-5)
		^{120}Sn (1.575E-4)
		^{122}Sn (2.238E-5)
		^{124}Sn (2.799E-5)

(b) Geometric parameters and composition of the guide tubes.

Cell pitch (cm):	ρ_{mod} (g cm^{-3}):	T_{mod} (K):	ρ_{B-10} (ppm):
1.27970	0.7142	579.55	2899.6

(c) Global parameters and moderator properties of the UOX assembly.

B.3.2 MOX fuel assembly (18 × 18)

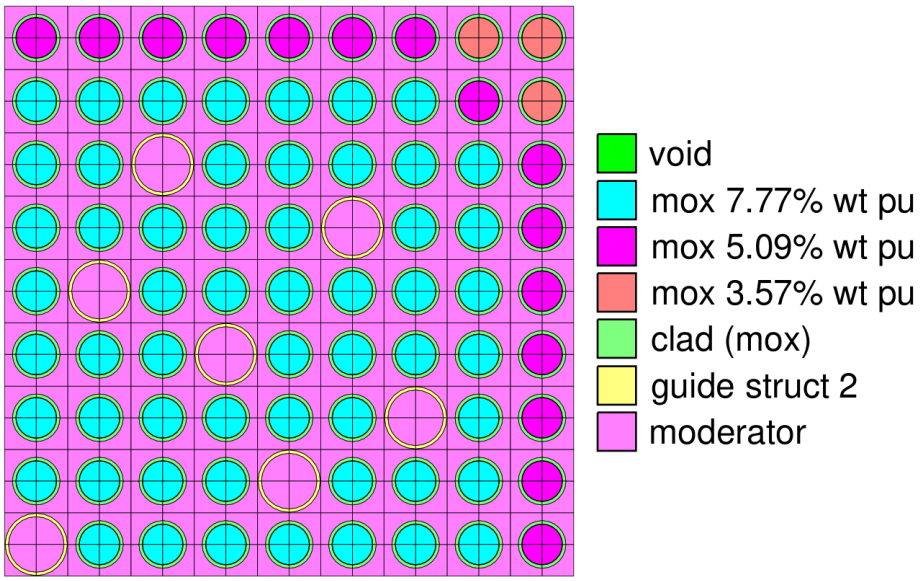

Figure B.6: Layout for the MOX fuel assembly used in the (UOX + MOX) colorset. The cell types employed in this assembly are MOX fuel rods with (*a*) 7.77 %, (*b*) 5.09 % and (*c*) 3.57 % PuO_2 weight, and (*d*) water channels surrounded by guide tubes.

Table B.6: Geometric parameters and compositions of the unit cells constituting the MOX assembly. Atom species without mass number denote natural composition. The notation $R\mathbf{E}\pm x$ is equivalent to $R\cdot 10^{\pm x}$.

Zone	fuel	void	clad
Radius (cm)	0.4025	0.411	0.475
Temperature (K)	845.95	670.0	581.83
Isotopes (density($(\mathrm{b}\cdot\mathrm{cm})^{-1}$))	^{241}Am (2.173E-5)	^{4}He (1.0E-15)	^{4}He (1.635E-17)
	^{16}O (4.557E-2)		^{93}Nb (3.784E-4)
	^{238}Pu (3.597E-5)		^{16}O (3.077E-4)
	^{239}Pu (9.927E-4)		S (2.467E-6)
	^{240}Pu (4.684E-4)		Zr (3.810E-2)
	^{241}Pu (1.451E-4)		
	^{242}Pu (1.190E-4)		
	^{234}U (1.459E-7)		
	^{235}U (5.214E-5)		
	^{236}U (2.607E-9)		
	^{238}U (2.094E-2)		

(a) Geometric parameters and compositions of the 7.77 % wt PuO_2 MOX fuel cell.

Table B.6: Geometric parameters and compositions of the unit cells constituting the MOX assembly (continued).

Zone	fuel	void	clad
Radius (cm)	0.4025	0.411	0.475
Temperature (K)	845.95	670.0	581.83
Isotopes (density$((\mathrm{b}\cdot\mathrm{cm})^{-1})$)	^{241}Am (1.517E-5)	^{4}He (1.0E-15)	^{4}He (1.635E-17)
	^{16}O (4.565E-2)		^{93}Nb (3.784E-4)
	^{238}Pu (2.233E-5)		^{16}O (3.077E-4)
	^{239}Pu (6.536E-4)		S (2.467E-6)
	^{240}Pu (3.092E-4)		Zr (3.810E-2)
	^{241}Pu (9.497E-5)		
	^{242}Pu (7.452E-5)		
	^{234}U (1.704E-7)		
	^{235}U (5.572E-5)		
	^{236}U (2.611E-9)		
	^{238}U (2.159E-2)		

(b) Geometric parameters and compositions of the 5.09 % wt PuO_2 MOX fuel cell.

Zone	fuel	void	clad
Radius (cm)	0.4025	0.411	0.475
Temperature (K)	845.95	670.0	581.83
Isotopes (density$((\mathrm{b}\cdot\mathrm{cm})^{-1})$)	^{241}Am (1.161E-5)	^{4}He (1.0E-15)	^{4}He (1.635E-17)
	^{16}O (4.606E-2)		^{93}Nb (3.784E-4)
	^{238}Pu (1.553E-5)		^{16}O (3.077E-4)
	^{239}Pu (4.627E-4)		S (2.467E-6)
	^{240}Pu (2.201E-4)		Zr (3.810E-2)
	^{241}Pu (6.648E-5)		
	^{242}Pu (5.210E-5)		
	^{234}U (1.746E-7)		
	^{235}U (5.711E-5)		
	^{236}U (2.635E-9)		
	^{238}U (2.214E-2)		

(c) Geometric parameters and compositions of the 3.57 % wt PuO_2 MOX fuel cell.

Radius (cm)	inner: 0.558600	outer: 0.616955
Temperature (K)		845.45
Isotopes (density$((\mathrm{b}\cdot\mathrm{cm})^{-1})$)		C (5.734E-5)
		^{50}Cr (3.286E-6)
		^{52}Cr (6.337E-5)
		^{53}Cr (7.185E-6)
		^{54}Cr (1.789E-6)
		Fe (1.479E-4)
		^{16}O (3.073E-4)
		Si (8.401E-6)
		Zr (4.228E-2)
		^{112}Sn (4.659E-6)
		^{114}Sn (3.170E-6)
		^{115}Sn (1.633E-6)
		^{116}Sn (6.984E-5)
		^{117}Sn (3.689E-5)
		^{118}Sn (1.163E-4)
		^{119}Sn (4.126E-5)
		^{120}Sn (1.565E-4)
		^{122}Sn (2.224E-5)
		^{124}Sn (2.781E-5)

(d) Geometric parameters and composition of the guide tubes.

Cell pitch (cm):	ρ_{mod} ($\mathrm{g\,cm^{-3}}$):	T_{mod} (K):	ρ_{B-10} (ppm):
1.27970	0.7142	579.55	2899.6

(e) Global parameters and moderator properties of the MOX assembly.

Appendix C

Checkerboard reference calculations

Table C.1: Data from the reference transport calculation on the pin checkerboard configuration of 1.80% UO_2 fuel pins neighbouring UO_2 fuel pins with varying enrichments.

		Pin 1 (1.80%)		Pin 2 (Var. %)	
Configuration	k_{eff}	$\bar{\phi}_{n,1}$ (a.u.)	$\bar{\phi}_{n,2}$ (a.u.)	$\bar{\phi}_{n,1}$ (a.u.)	$\bar{\phi}_{n,2}$ (a.u.)
1.80% + 1.60%	0.96672798	0.4082	0.0922	0.4071	0.0925
1.80% + 1.80%	0.98648678	0.4100	0.0900	0.4100	0.0900
1.80% + 2.00%	1.00478571	0.4118	0.0878	0.4128	0.0876
1.80% + 2.20%	1.02181279	0.4134	0.0859	0.4154	0.0854
1.80% + 2.40%	1.03768462	0.4150	0.0840	0.4178	0.0833
1.80% + 2.60%	1.05251755	0.4165	0.0822	0.4200	0.0813
1.80% + 3.10%	1.08569776	0.4200	0.0781	0.4251	0.0768
1.80% + 3.60%	1.11427124	0.4231	0.0745	0.4296	0.0728

(a) Multiplication factor and average flux values, normalized per pin per group.

	Pin 1 (1.80%)				Pin 2 (Var. %)			
Configuration	$\Sigma_{t,1}$ (cm^{-1})	$\Sigma_{t,2}$ (cm^{-1})	$\Sigma_{a,1}$ (cm^{-1})	$\Sigma_{a,2}$ (cm^{-1})	$\Sigma_{t,1}$ (cm^{-1})	$\Sigma_{t,2}$ (cm^{-1})	$\Sigma_{a,1}$ (cm^{-1})	$\Sigma_{a,2}$ (cm^{-1})
1.80% + 1.60%	0.5399	1.265	0.009674	0.07458	0.5405	1.259	0.009493	0.06992
1.80% + 1.80%	0.5401	1.262	0.009665	0.07432	0.5401	1.262	0.009665	0.07432
1.80% + 2.00%	0.5402	1.260	0.009655	0.07407	0.5397	1.266	0.009835	0.07865
1.80% + 2.20%	0.5403	1.258	0.009646	0.07382	0.5394	1.270	0.01000	0.08291
1.80% + 2.40%	0.5404	1.257	0.009637	0.07359	0.5391	1.274	0.01017	0.08709
1.80% + 2.60%	0.5405	1.255	0.009627	0.07336	0.5388	1.278	0.01034	0.09122
1.80% + 3.10%	0.5406	1.250	0.009603	0.07282	0.5382	1.288	0.01074	0.1012
1.80% + 3.60%	0.5406	1.246	0.009578	0.07232	0.5378	1.297	0.01114	0.1109
Configuration	$\nu\Sigma_{f,1}$ (cm^{-1})	$\nu\Sigma_{f,2}$ (cm^{-1})	$\Sigma_{f,1}$ (cm^{-1})	$\Sigma_{f,2}$ (cm^{-1})	$\nu\Sigma_{f,1}$ (cm^{-1})	$\nu\Sigma_{f,2}$ (cm^{-1})	$\Sigma_{f,1}$ (cm^{-1})	$\Sigma_{f,2}$ (cm^{-1})
1.80% + 1.60%	0.005404	0.09240	0.002089	0.03792	0.005042	0.08262	0.001943	0.03391
1.80% + 1.80%	0.005382	0.09205	0.002081	0.03778	0.005382	0.09205	0.002081	0.03778
1.80% + 2.00%	0.005363	0.09171	0.002074	0.03764	0.005717	0.1013	0.002217	0.04158
1.80% + 2.20%	0.005345	0.09139	0.002068	0.03750	0.006047	0.1104	0.002351	0.04531
1.80% + 2.40%	0.005329	0.09107	0.002062	0.03737	0.006373	0.1194	0.002484	0.04898
1.80% + 2.60%	0.005313	0.09077	0.002056	0.03725	0.006695	0.1281	0.002614	0.05259
1.80% + 3.10%	0.005279	0.09005	0.002043	0.03696	0.007482	0.1495	0.002935	0.06137
1.80% + 3.60%	0.005249	0.08939	0.002032	0.03668	0.008249	0.1701	0.003247	0.06982
Configuration	$\Sigma_{s,1\to2}$ (cm^{-1})	$\Sigma_{s,2\to1}$ (cm^{-1})	$\Sigma_{s,1\to1}$ (cm^{-1})	$\Sigma_{s,2\to2}$ (cm^{-1})	$\Sigma_{s,1\to2}$ (cm^{-1})	$\Sigma_{s,2\to1}$ (cm^{-1})	$\Sigma_{s,1\to1}$ (cm^{-1})	$\Sigma_{s,2\to2}$ (cm^{-1})
1.80% + 1.60%	0.01666	0.001397	0.5136	1.189	0.01671	0.001394	0.5143	1.187
1.80% + 1.80%	0.01662	0.001433	0.5138	1.187	0.01662	0.001433	0.5138	1.187
1.80% + 2.00%	0.01658	0.001467	0.5140	1.185	0.01654	0.001471	0.5134	1.186
1.80% + 2.20%	0.01654	0.001501	0.5142	1.183	0.01646	0.001508	0.5130	1.186
1.80% + 2.40%	0.01650	0.001534	0.5144	1.181	0.01638	0.001545	0.5126	1.185
1.80% + 2.60%	0.01645	0.001566	0.5145	1.180	0.01630	0.001581	0.5122	1.185
1.80% + 3.10%	0.01634	0.001644	0.5147	1.176	0.01612	0.001668	0.5114	1.185
1.80% + 3.60%	0.01622	0.001717	0.5148	1.172	0.01595	0.001751	0.5107	1.184

(b) Macroscopic cross sections for the total, absorption, nu-fission, fission, out-scatter and self-scatter reactions